INVESTIGATION OF THE NEAR SURFACE MECHANICAL PROPERTIES OF AMMONIUM PERCHLORATE BY NANOINDENTATION

By

OSCAR MEJIA

Bachelor of Engineering

Universidad Centroamericana "Jose Simeon Cañas"

San Salvador, El Salvador

2001

Submitted to the Faculty of the
Graduate College of the
Oklahoma State University
in partial fulfillment of
the requirements for
the Degree of
MASTER OF SCIENCE
May, 2004

INVESTIGATION OF THE NEAR SURFACE
MECHANICAL PROPERTIES OF
AMMONIUM PERCHLORATE
BY NANOINDENTATION

Thesis Approved:

Dr. D. A. Lucca

Thesis Adviser

Dr. C. E. Price

Dr. A. J. Ghajar

Dr. A. Carlozzi

Dean of the Graduate College

ACKNOWLEDGMENTS

I would like to thank my adviser, Dr. D. A. Lucca. Without him, this dissertation would not have been possible. I thank him for his encouragement and patience that carried me on through difficult times, and for his insights and suggestions that helped to shape my research skills. His valuable feedback contributed greatly to this dissertation.

I also thank my committee members Dr. C. E. Price and Dr. A. J. Ghajar for their time and suggestions. Their valuable feedback helped me to improve the dissertation in many ways.

I would like also to acknowledge LASPAU-OAS for their benevolence in providing a full scholarship grant for my master study.

I also thank Matt Klopfstein, who advised me and helped me in various aspects of my research. He is the one that I can always count on to discuss the tiniest details of a problem.

I would like to extend my thanks and appreciation to Dr. David Hamby and Rudy Ghisleni for their assistance, without which this work would have taken much longer.

Finally, I have to thank those who are ultimately responsible. My parents and my sisters have supported me throughout.

Above all, I thank God for His blessings, support and all the strength, and I thank the Blessed Virgin Mary for umpteen intercessions.

NOMENCLATURE

a ..... Lattice spacing

A ..... Projected contact area

A_c ..... Projected contact area at peak load

AFM ..... Atomic Force Microscope/Microscopy

AP ..... Ammonium Perchlorate

ASTM ..... American Society for Testing and Materials

b ..... Lattice spacing

c ..... Lattice spacing

c_{ij} ..... Elastic compliances

C_f ..... Machine compliance

C_s ..... Sample compliance

C_t ..... Total compliance

E ..... Elastic Modulus

E_i ..... Elastic modulus for the indenter

E_r ..... Reduced modulus

EFC ..... Electrostatic force constant

EPD ..... Etch pit density

ESA ..... European Space Agency

h ..... Elastic displacement of the sample

h_c ..... Contact depth

h_f ..... Residual depth upon unloading

h_s ..... Surface displacement of the contact perimeter

h_{max} ..... Penetration depth corresponding to peak load

H ..... Hardness

IIT ..... Instrumented Indentation Testing

ISO ..... International Organization for Standarization

K_{Ic} ..... Fracture toughness (Mode I)

l ..... Direction cosines of any arbitrary direction

m ..... Constant

P ..... Applied load

P_{max} ..... Peak load

P_{crit} ..... Critical load (pop-in load)

RMS ..... Root mean square

R ..... Radius of the indenter

R_a ..... Average roughness

R_q ..... Rms roughness

RDX ..... Cyclotrimethylenetrinitramine

s_{ij} ..... Elastic constants

S ..... Contact Stiffness

SEM ..... Scanning Electron Microscope/Microscopy

SPM ..... Scanning Probe Microscope/Microscopy

TEM ..... Transmission Electron Microscope/Microscopy

VHN ..... Vickers hardness number

XRD ..... X-ray diffraction

α ..... Constant

ν ..... Poisson's ratio for the specimen

ν_i ..... Poisson's ratio for the indenter

τ_{theo} ..... Theoretical shear strength

τ_{max} ..... Maximum shear stress

TABLE OF CONTENTS

LIST OF FIGURES

LIST OF TABLES

Chapter 1

Introduction

The substantial and extensive applications of energetic materials have made safety an important issue in the development of insensitive propellants. An insensitive propellant is one in which there is minimized possibility of initiation as a result of unintentional impact or thermal and shock stimuli [1]. The investigation of the localized nature of plastic deformation processes in energetic crystals is thus of vital importance in understanding initiation and ignition processes when they are subjected to mechanical forces [2,3]. Moreover, the energy dissipation by the action of mechanical forces on dislocations in energetic crystals is of considerable interest because of the proposal that localized reaction sites or "hot spots" which lead to rapid chemical decomposition are generated during the collapse of obstructed dislocation pileups, particularly in association with cracking processes [4, 5]. It is also known that material microstructure, lattice arrangement and the plasticity of the material play an important role in the orientation dependence of the shock initiation of crystalline energetic materials [6, 7].

At present, ammonium perchlorate (AP) is the most widely used crystalline oxidizer because of its desirable characteristics, including compatibility with other propellant materials, good propulsion performance, quality, uniformity, cost and availability [8, 9]. Unfortunately a basic understanding of the mechanical response of AP

to loading does not exist, and little has been reported on its mechanical properties. Furthermore, most of the previous work on the characterization of the mechanical properties of AP has been performed on crystal whiskers and large single crystals ($\geq$ 1 cm edge length) which are significantly greater in size than those typically used in solid propellant formulations ($\approx$ 100 - 600 μm) [8, 10–12].

Research groups at the Politecnico di Milano and Oklahoma State University have collaborated in an investigation of the near surface mechanical properties and mechanical behavior of AP when subjected to force loading for crystal size less than 350 μm using nanoindentation. To our knowledge, investigations of mechanical properties have not been reported for AP at this length scale.

AP has a large unit cell (40 atoms per unit cell) and readily cleaves on the {210} and {001} planes which also correspond to two of the predominant crystal "as-grown" planes [13,14]. Since, hardness testing provides an index of mechanical behavior that has been correlated experimentally with sensitivity to initiation of decomposition and because the orientation of the crystal is related to the structure-sensitive properties, this investigation includes the investigation of both planes [5, 11].

Since, most energetic materials are insulating and electrostatic energy buildup can be large enough to cross the reaction barrier for explosion, electron based microscopes are difficult and in some cases impossible to use for investigation, specifically transmission electron microscope (TEM) and scanning tunneling microscope (STM). The best instrument for high resolution imaging of AP could be the atomic force microscope (AFM) [15].

Sensitivity, thermal decomposition and the ignition often appear to be associated with crystal imperfections, e.g., edge and screw dislocations, therefore, the scope of this study includes an investigation of the etch pits formed on cleavage planes [16]. Interesting internal features of the pits not previously reported have been observed with the AFM.

Chapter 2 consists of a literature review which includes: the role of the mechanical response to load in the thermal decomposition of energetic materials, a description of the mechanical properties and etching investigations previously performed on AP, and an overview of the nanoindentation technique.

Chapter 3 details the experimental procedure and describes the instruments utilized. Chapter 4 explains the analysis of data and discusses the results. Chapter 5 presents a summary and conclusions of the investigation.

1.1 Objectives of the Research Study

The principal objectives of this investigation are:

- To contribute to the understanding of the near surface mechanical response of the two cleavage planes of AP under very low load using nanoindentation in combination with AFM imaging. Investigations have not been reported at this length scale where an analysis of results in terms of creation and motion of individual dislocations must be considered.

- To further develop known etching techniques developed by P.J. Herley et al. [14] and J.O. Williams et al. [13] and to study the internal structure of etch pits on the cleavage planes using AFM, which is the only surface microscopy technique providing the necessary vertical resolution at large observation scales.

Chapter 2

Literature Review

2.1 Energetic Materials

Energetic materials are defined as substances that undergo exothermic chemical reaction in response to some stimulus and react in time scales leading to combustion, explosion or detonation [17]. Energetic materials represent a multibillion dollar industry for both commercial and military uses [18]. These are among the earliest man made classes of materials and their historical role in the development of nations has been enormous. Land clearing, railroad and highway construction, and mining continue as important applications although not the only ones. The space program is enabled by energetic materials.

Explosives, pyrotechnics and propellants are subclasses of energetic materials [17].

Explosives

Explosives are solid, liquid or gaseous substances or mixtures of substances which, in their applications as primary rocket boosters, charges in warheads, demolition and other applications, are required to detonate [17].

Pyrotechnics

Pyrotechnics are mixtures of solid or liquid fuels or oxidizers which, when ignited, undergo an energetic chemical reaction at a controlled rate intended to produce spe-

cific time delays, heat, noise, smoke, visible light or infrared radiation [17].

Propellants

Propellants are the chemical mixture burned to produce thrust in rockets and consist of a fuel and an oxidizer. The fuel is the substance which burns when combined with oxygen producing gas for propulsion. The oxidizer is the agent that releases oxygen for combination with the fuel. There are different kind of propellants according to their state: liquid, solid, or hybrid [19].

Modern propellants are heterogeneous powders (mixtures) which use a crystallized or finely ground mineral salt as an oxidizer, often AP, which constitutes between 60% and 90% of the mass of the propellant [19]. A typical fuel is aluminum. The propellant is held together by a polymeric binder, usually polyurethane or polybutadiene. The final product is a rubber-like substance with the consistency of a hard rubber eraser [19].

The oxidizer itself, such as AP, potassium perchlorate, ammonium nitrate, and lithium perchorate, may be used as a monopropellant [17]. They have the advantage of only needing to store one compound. Along with these advantages come the disadvantages that they usually have lower specific impulses than many propellants mixture and inappropriate physical properties [19].

Solid propellant motors have a variety of applications. For example a large scale application is the space shuttle solid-rocket booster that uses a mixture of AP with aluminum [20]; also small solid propellant motors often power the final stage of a launch vehicle, or attach to payloads to boost them to higher orbits. Medium propellant motors such as the payload assist module and the inertial upper stage provide the added boost necessary to place satellites into geosynchronous orbit or on planetary trajectories [17]. In addition to their use in propulsion systems, they are used in airbags where a high rate of gas generation is critical [21]. Monopropellant rockets produce very little thrust and don't have a high specific impulse, either, but are

extremely simple to operate and can be turned on and off easily. Many satellites contain monopropellant rockets for fine adjustment of orbital position [17].

In the past few years much attention has been recently focused on solid propellant containing aluminum nanoparticles as a fuel; the presence of aluminum nanopowders have shown benefits such as: shortened ignition delay, shorter burning time for the nano-particles, higher surface area, and greater flexibility for designing propellants with desirable physical properties [21, 22]. The most widely known product used is the ultrafine aluminum powder "Alex", sold by the Argonide Corporation. Alex is comprised of spherical particles having a diameter of 100 - 200 nm [23]. Nanoaluminized propellant is used today to produce up to 90% of the thrust for take-off for both the Ariane rocket (ESA) and Space Shuttle [22].

Clearly, propellants may have a complex compositions and physical structures to that thermochemical and physical characteristics are not readily available [24].

2.2 Importance of Mechanical Properties

The explosive event is usually divided into various stages: ignition, growth of deflagration, the deflagration to detonation transition and the propagation of detonation [25]. Ignition is defined as the condition that occurs when a reaction continues to produce energy without further external heating. Deflagration is an explosive reaction such as rapid combustion that moves through an explosive material at a velocity less than the speed of sound. Detonation is the explosive reaction which moves through the explosive material at a velocity greater than the speed of sound. The ease with which an energetic material can be caused to undergo a violent reaction or detonation is called sensitivity [26].

The exact role of propellant mechanical properties on the sensitivity of the energetic materials is not well understood but from a macroscopic point of view, the

mechanical break up of the material can affect the explosive performance by increasing surface area or by facilitating the propagation of the reaction [27]. Explosives materials in projectiles are subjected to high forces during launching that can cause fracture and premature ignition and it is important to have a complete knowledge of the mechanical properties. Many mechanical and thermal properties are required for the numerical simulation of deformation, crack propagation, and combustion phenomena of propellants [24]. From a microscopic point of view, it has been shown that localized regions in crystalline energetic materials undergo preferential chemical decomposition as a result of the materials experiencing mechanical forces [8]. Networks of microscopic cracks have been associated with initiation of chemical decomposition and are associated with structural changes of the crystal lattice [11]. Sandusky et al. [12] demonstrated that an increase in defect (dislocation) density enhances the chemical decomposition in relatively defect-free AP, and also considered the shock reactivity as microstructurally based. Ritchie [26] has observed an orientation dependence of the shock initiation of energetic materials attributed to anisotropy of plastic flow. Dick [6] has proposed that shocks oriented parallel to a relative unlikely slip system would not trigger any reaction. Examples of explosive behavior that are believed to be sensitive to microstructural effects are shock sensitivity, fragment impact sensitivity, thermal response, friction response and response to low velocity impact [24]. The energetic materials are known to be brittle and their indentation hardness is of special interest because it provides an index of mechanical behavior that has been correlated experimentally with sensitivity to initiation of decomposition [11].

In many situations and most accidents, reaction starts and propagates from localized "hot spots". If, in these small volumes or hot spots, as they are referred, the release of chemical energy is greater than that dissipated by heat losses, then the reaction will grow. It has been shown that thermal decomposition of AP begins at individual points and develops in an anisotropic manner [28]. The occurrence of

these specific regions of decomposition suggest that their origin is related closely to material microstructure and associated with plastic deformation, cracking behavior and presence of dislocations [8, 28, 29].

A model was developed by Armstrong et al. [4] in which the generation of high temperatures within local regions in the form of thermal hot spots is associated with dislocation pile-ups being released suddenly in an avalanche configuration.

2.2.1 "Hot spot" Mechanisms

In general it is believed that ignition is thermal in origin, however mechanical and electrical energy is visualized as being converted into thermal energy and concentrated into a small localized region referred as "hot spots" by a variety of mechanisms that can cause ignition [30]. Impact, friction, shock waves, ultrasonic vibrations, and flying particles have been used to induce explosion [2]. The suggested size of the hot spot is about 100 nm diameter but is material dependent [2].

Thermal decomposition takes place at the hot spot, and because of the exothermic nature of the decomposition, the rate of decomposition rapidly increases and thermal explosion may result [2].

Although there is general agreement that the initiation is due to the existence of such hot spots, there is still wide disagreement as to the cause of these hot spots. Over the years several mechanisms have been suggested for hot spot formation in solid explosives:

- Bowden and Yoffe [2] and Chaudhri and Field [31] have shown that adiabatic compression of small trapped gas bubbles is a key factor in the sensitivity of explosives.

- Field et al. [30] and Bowden and Yoffe [2] have shown that the friction between surfaces of the explosive can generate hot spots. The actual conditions for

explosion depend on factors such as hardness, thermal conductivity, and shape and size of the surfaces [2, 30].

- Winter and Field [32] have shown that if plastic deformation is localized into bands, of dimensions of the order of a micrometer or more, then hot spots can be formed which cause ignition. AFM studies of plastically deformed RDX($C_3H_6N_6O_6$) crystals by shock experiments have shown that melting occurs within the shear bands [33].

- Armstrong et al. [4, 9] have shown that dislocation pile-ups can produce hot spots. The mechanism proposed is based on dislocation pile-ups against a local obstacle on the slip plane where, as the shear stress increases, the obstacle collapses and the dislocations are suddenly released in an avalanche configuration. Figure 2.1 shows a schematic illustration of the model. The high locally concentrated stresses generated at the tips of the pile-ups are able to generate a rate of plastic work which allows for high temperatures to be reached. However, many authors believe that such hot spots will never reach the necessary characteristics to cause the ignition of the energetic material [30].

- Field [25] has proposed that the high temperatures generated at crack tips can promote the formation of hot spots. Although, some authors consider that this mechanism is not a viable one for the ignition of an explosive crystal [34]. Nevertheless, the formation of cracks can produce gaseous decomposition of products, and this can make an explosive more sensitive due to the formation of pockets of gas, which can then be adiabatically compressed and cause ignition.

There is no single dominant mechanism responsible for the initiation of thermal decomposition since it depends on the energy input and the physical properties of the explosive. Moreover, a critical hot spot can be formed with the combination of mechanisms listed above [30].

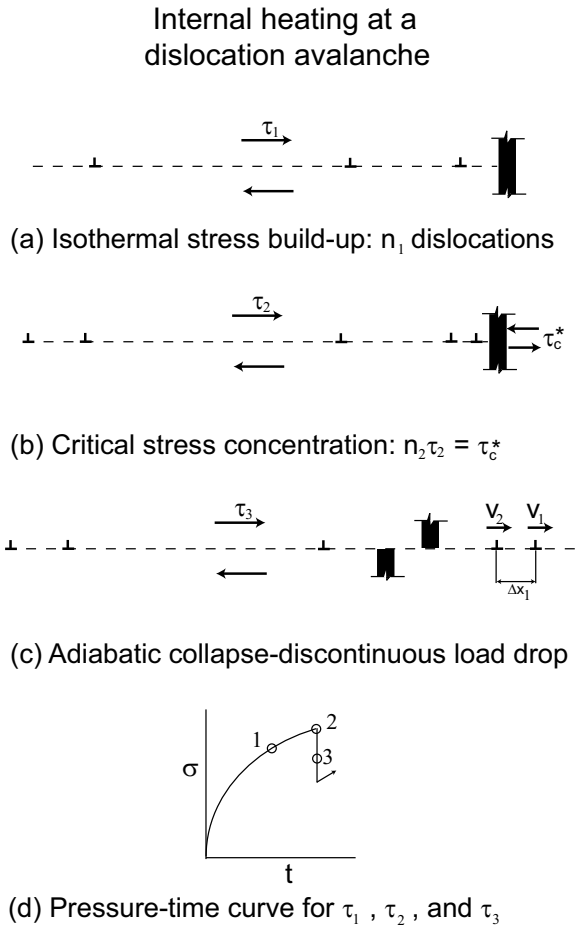

Figure 2.1: Hot spot model based on dislocation pile-up and collapse [4].

2.3 Ammonium Perchlorate

Ammonium Perchlorate, NH_4ClO_4 (Fig. 2.2), is the most widely used oxidizer for solid propellants [8]. It is stable, hygroscopic, reasonably high-performing and safe to handle [19].

AP is produced by a process developed by Schumacher [19] involving the reaction of sodium perchlorate with ammonia and hydrochloric acid:

$$NH_3 + HCl + NaClO_4 \rightarrow NH_4ClO_4 + NaCl \tag{2.1}$$

it is prepared by a double displacement reaction and the products are separated by fractional crystallization.

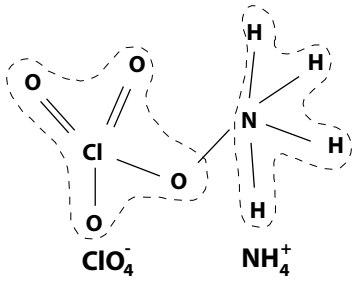

Figure 2.2: AP molecule (NH_4ClO_4).

AP is stable at room temperature but decomposes at measurable rates for temperatures greater than about 150°C [19]. The thermal decomposition of AP has been extensively studied and it has been shown that below 300°C the decomposition follows Eq.(2.2) [35] below:

$$4NH_4ClO_4 \rightarrow 2Cl_2 + 3O_2 + 8H_2O + 2N_2O \tag{2.2}$$

Above 350°C product analysis reveals that the decomposition follows Eq.(2.3) [35] below:

$$10NH_4ClO_4 \rightarrow 2.5Cl_2 + 2N_2O + 2.5NOCl + HClO_4 + 1.5HCl + 18.75H_2O + 1.75N_2 + 6.375O_2 \tag{2.3}$$

2.3.1 Physical Properties

The previously reported values of hardness and moduli of AP are presented in Table 2.1. An expanded table of physical properties of AP is included in Appendix A.

In 1973 Raevskii et al. [10] performed elongation tests on pure crystals and crystal whiskers of AP. Crystal whiskers exhibited a higher tensile strength (127.5 MPa) than pure crystals (4.9 MPa). The elastic modulus obtained from the crystal whiskers ranged between 19.6 GPa and 39.2 GPa (Table 2.1).

The elastic constants c_{ij} (10^{10} N m^{-2}) measured for AP using ultrasonic resonance frequencies [36] and Brillouin scattering method [39] are given in Table 2.2. The

Properties	**Symbols**	**Value**	**Units**	**Reference**
Elastic Modulus	E	19.6 - 39.2	GPa	[10]
Elastic Modulus [210]	$E_{[210]}$	21.3	GPa	[36]
Elastic Modulus [001]	$E_{[001]}$	25.1	GPa	[36]
Hardness (210) plane	$H_{(210)}$	0.127	GPa	[8]
Hardness (001) plane	$H_{(001)}$	0.108	GPa	[8], [8], [37]
Bulk Modulus	K	15.2±0.3	GPa	[38]
Shear Modulus	G	7.4	GPa	[9]

Table 2.1: Hardnesses and moduli reported for AP.

direction dependent elastic modulus (E) for orthorhombic crystals can be obtained by [40]:

$$\frac{1}{E} = l_1^4 + 2l_1^2l_2^2s_{12} + 2l_1^2l_3^2s_{13} + l_2^4s_{22} + 2l_2^2l_3^2s_{23} + l_3^4s_{33} + l_2^2l_3^2s_{44} + l_1^2l_3^2s_{55} + l_1^2l_2^2s_{66} \tag{2.4}$$

where s_{ij} are the usual elastic compliance constants and l_1, l_2 and l_3 are the direction cosines in any arbitrary direction. Using Eq.(2.4) and the elastic compliance constants given in Table 2.2 the elastic modulus was calculated along the [001] and [210] direction obtaining 25.1 GPa and 21.3 GPa respectively (Table 2.1).

When AP is heated to about 238°C an allotropic phase transformation to the cubic, rock-salt structure occur with four molecules per unit cell and $a = 0.763$ nm [1, 38]. Peiris et al. [38,41] investigated the change of structural properties with pressure and found two phase transitions: the first transition starts at about 2.9 GPa and the second phase transformation in AP is observed to start at 5.0 GPa.

Elastic Constants	**Haussühl [36]**	**Vazquez et al. [39]**	**Elastic Compliance**	**Haussühl [36]**
c_{11}	2.297	2.51	s_{11}	0.887
c_{22}	2.356	2.46	s_{22}	0.938
c_{33}	3.012	3.15	s_{33}	0.391
c_{44}	0.469	0.66	s_{44}	2.132
c_{55}	0.584	0.47	s_{55}	1.712
c_{66}	0.964	1.03	s_{66}	1.037
c_{12}	1.660	1.63	s_{12}	-0.624
c_{13}	0.735	1.15	s_{13}	-0.0025
c_{23}	1.033	0.76	s_{23}	-0.170

Table 2.2: Elastic constants c_{ij} (10^{10} Nm^{-2}) and elastic compliances s_{ij} (10^{-10} $\mathrm{N}^{-1}\mathrm{m}^2$) determined for AP using ultrasonic resonance frequencies [36] and Brillouin scattering method [39].

2.3.2 Crystallographic Structure

AP is an insulator and below 238°C it exhibits an orthorhombic lattice structure of dimensions $a = 9.202$ Å, $b = 5.816$ Å, and $c = 7.449$ Å, and belongs to the Pnma space group [42]. Where Pnma denotes the centrosymmetric space group with a primitive lattice with n-glide perpendicular to the a axis, a mirror plane perpendicular to the b axis and a-glide perpendicular to the c axis [43]. The crystallographic unit cell is composed of four NH_4ClO_4 molecules, like the one shown in Fig. 2.2, each molecule is composed of a perchlorate anion (ClO_4^-) and an ammonium cation (NH_4^+), for a total of 40 atoms in each unit cell. The established parameters for the crystal structure are presented in Table 2.3. The position in parentheses (Table 2.3) represent the values found with neutron diffraction. The difference between the data obtained with

X-rays and neutron diffraction indicates that a disorder exists in the way the NH_4 ions are oriented, therefore, no parameters are given to the hydrogens [42]. At room temperature, the ammonium ions behaves as a single unit in the unit cell [44].

The unit cell and the projections of the principal crystallographic planes (100), (010) and (001) are presented in Fig. 2.3. These projections are consistent with the ones obtained by Williams et al. [13] and Yoo et al. [15].

AP crystals grown at room temperature from aqueous solution have the crystallographic features shown in Fig. 2.4, where the principal crystallographic planes observed are the (210) and (001) [13].

2.3.3 Cleavage Planes

The cleaving process is a low energy fracture process associated with transcrystalline fracture along explicit crystallographic planes determined by the characteristics of the crystal structure [45]. Ionic and covalently bonded crystals are more prone to exhibit cleavage than metals, since cleavage is an intrinsically brittle fracture phenomenon.

Cleavage facets are smooth and flat surfaces that present a ledge morphology.

Atom	**Position**	[100]	[010]	[001]
NH_4	4*c*	0.183 (0.182)	1/4	0.167 (0.166)
Cl	4*c*	0.067 (0.068)	1/4	0.692 (0.693)
O(1)	4*c*	0.179 (0.186)	1/4	0.554 (0.561)
O(2)	4*c*	-0.075 (-0.070)	1/4	0.596 (0.607)
O(3)	8*d*	0.079 (0.082)	0.044 (0.053)	0.800 (0.803)

Table 2.3: Crystallographic parameters of AP after Wyckoff [42] using XRD the values in parentheses were obtained using neutron diffraction. Refer to Fig. 2.3 for orientation of axes

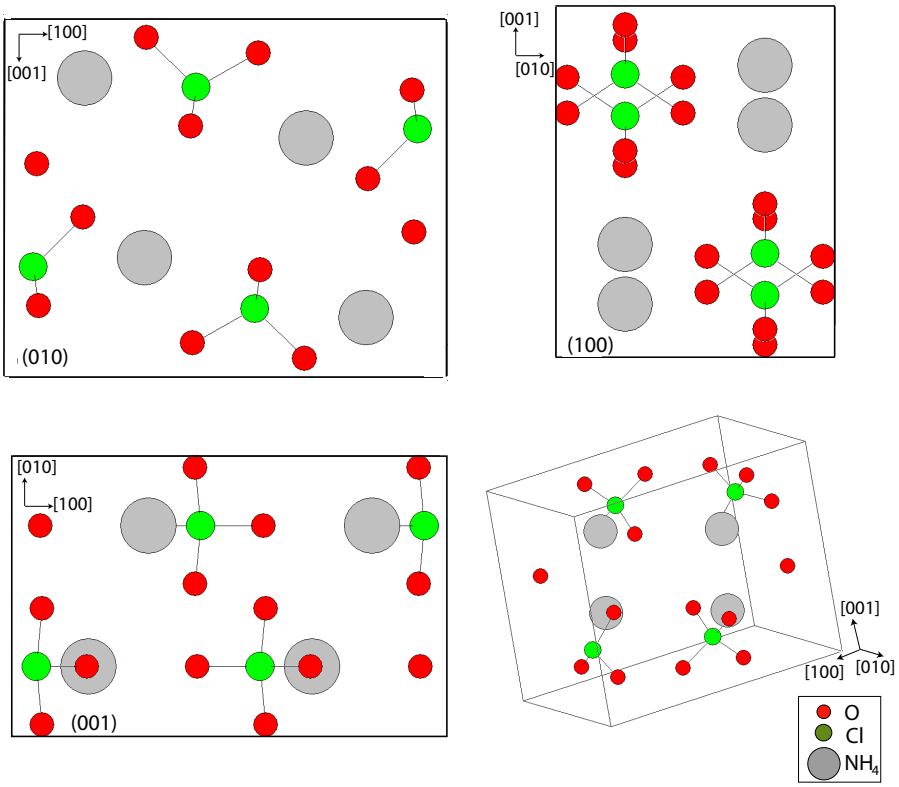

Figure 2.3: Unit cell and principal crystallographic planes of AP. Gray spheres represent the ammonium ion (NH_4^+). Image based on Wyckoff [42] results and obtained using the software Diamond2.1e. Atomic diameters are reduced in relation to the cell in order to clarify the spatial arrangement.

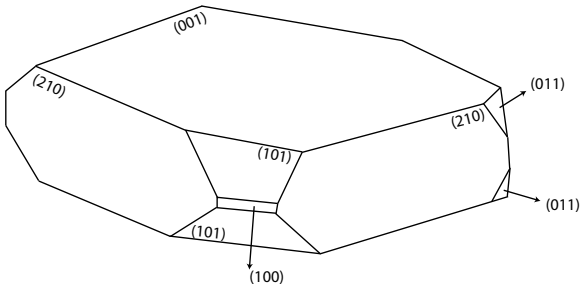

Figure 2.4: Crystallographic features of AP grown crystals [13].

Figure 2.5(a) and (b) illustrates the cleavage surfaces of $Bi_2Se_{2.8}Te_{0.2}$ and AlNiCo respectively . It is usual to see fine cleavage steps that appear as "river markings". This river pattern points out that the cleavage surface is not a single plane but a group of parallel planes, as can be seen in Fig. 2.5(c), and that the crack has been deflected at the steps by obstacles like screw dislocations or point defects . For these surfaces a number of screw dislocations probable pre-existed in the material, but others can be produced at the root of the crack where high stresses are generated [46, 47].

In addition to defining the cleavage planes by the Miller indices, they are described in terms of quality as: perfect, good and poor. Quality represents the degree of perfection of the cleavage surface and the ease with which the crystal cleaves.

Although the cleavage process has been known for a long time, the principle by which the cleavage planes are determined is still debated. Schultz et al. [50] have critically examined previously proposed criteria for cleavage:

- Criteria based on crystal structure: An early association was considered between

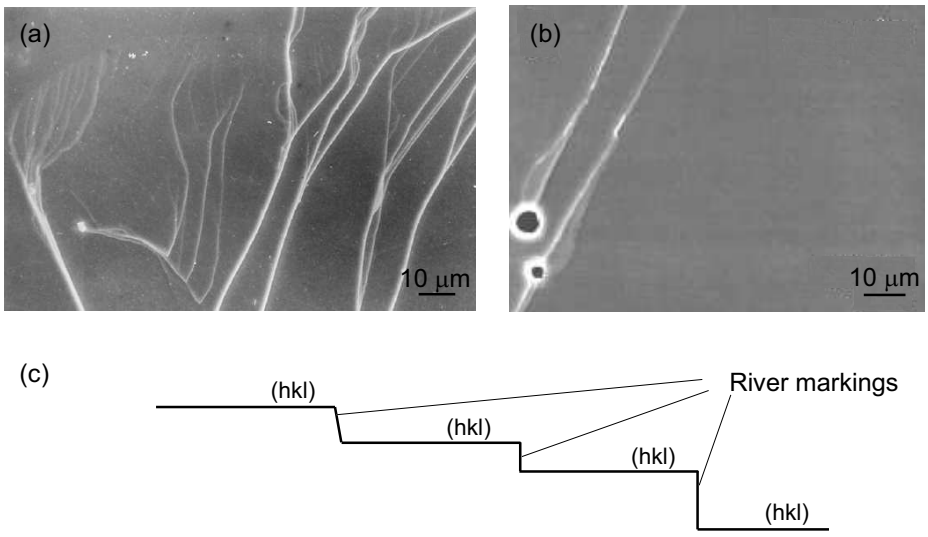

Figure 2.5: (a) SEM image of the (111) cleavage plane of $Bi_2Se_{2.8}Te_{0.2}$ [48] (b) SEM image of the cleavage plane of decagonal AlNiCo [49] (c) River markings model showing stairway configuration generated by crack deflection.

the cleavage process and the external planes formed during crystal growth, however the cleavage planes are not consistent with the planes exposed during the crystal growth process. This is because the processes that dominate crystal growth are different than those that control the cleavage process. The most closely packed planes were also considered as a possibility because of their ability to experience breaking of bonds, however this criterion does not apply for all crystal structures. The lack of success of using this criteria leads to the conclusion that the properties of the crystal structure must be examined, rather than the structure itself.

- Criteria based on crystal properties: Since cleavage involves breaking of bonds, it is important to consider bonds and ions, group of ions, or atoms which form those bonds. When cleavage occurs, the two resulting fracture surfaces will consist of equivalent pairs of ions, or atoms across the new surfaces. This matching criteria implies that an ionic crystal does not cleave on non-neutral crystal planes, with an unequal ionic charge distribution over the two new surfaces. After applying this criteria to a group of materials, Schultz et al. [50] concluded that this ionic neutrality is not a positive criterion for cleavage; rather, it is an exclusionary one. Therefore, this criteria implies that non-neutral planes can not experience cleavage.

- Criteria based on the bond density concept, which implies that the lower densities are associated with cleavage planes. This approach has not been successful because it does not incorporate different bond strengths.

- It has been stated that the cleavage plane is the plane of the minimum surface energy. This approach has exceptions and is more applicable to growth planes.

Schultz et al. [50] stated that each of these criteria fails when applied in a universal sense, and attribute this failure to the fact that none of the criteria consider

the dynamic aspects of the cleavage process. Schultz et al. [50] proposed that a dynamic fracture criterion must be applied based on the fracture toughness concept K_{Ic}. They demonstrated that the established cleavage plane has the lowest experimentally measured fracture toughness value.

Cleavage planes of Ammonium Perchlorate

AP cleaves parallel to the {210} and {001} planes [13, 14]. Here, "{}" represents a group of equivalent planes (Appendix B).

Figure 2.6 illustrates the projection of an AP crystal along the (001) plane. This projection is consistent with the one observed by Yoo et al. [15] and Williams et al. [13].

The {210} planes are perpendicular to the {001} planes and they meet along the diagonal lines parallel to the ones shown in Fig. 2.6. The crystal can cleave along any plane parallel to these lines. This structure has ten planes going through the molecules. It is difficult to envision which of these ten planes will be exposed.

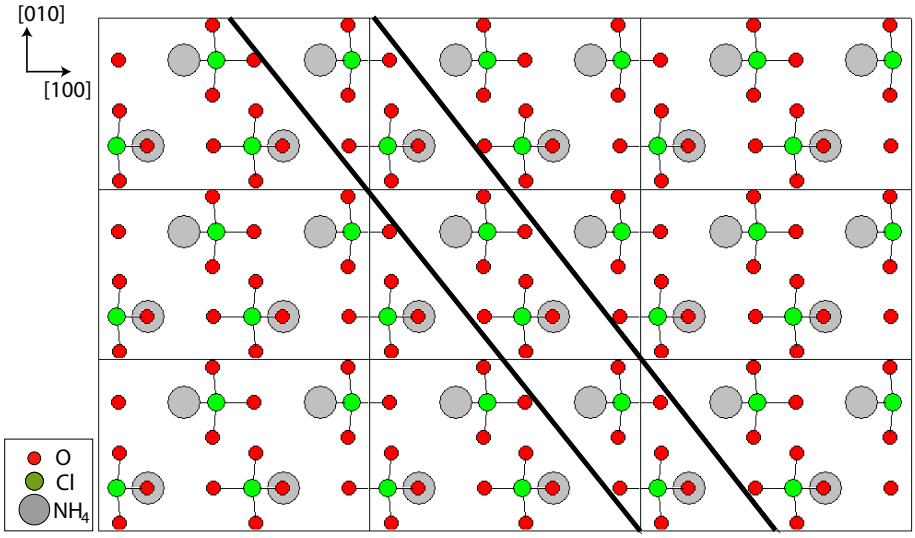

Figure 2.6: Projection of the (001) plane. The two diagonal lines indicate the intersection of two (210) planes.

A possibility is that cleavage occurs on the planes that have the fewest number of molecular bonds crossing them and the planes that have the largest spacing between them. A likely possibility for the cleavage planes is along the planes (diagonal lines) shown in Fig. 2.6 because they are the planes separated by the largest distance, there are no strong bonds crossing these planes, i.e., the perchlorate and the ammonium ions are completely separated [15]. The projection of the {210} planes is shown in Fig. 2.7. It coincides with the one obtained by Yoo et al. [15] but is in disagreement with the dimensions of the projected unit cell predicted by Herley et al. [14]. The principal difference is that Herley et al. [14] obtained a {210} unit cell that is 7.42 Å in the ⟨120⟩ direction, as one would expect from crossing of a {210} planes trough a single unit cell. However, a careful analysis of the crystal structure shows that the {210} planes unit cell should cross two unit cells along the ⟨120⟩ direction, Fig. 2.6, thus giving a cell length of 2×7.42 Å = 14.84 Å.

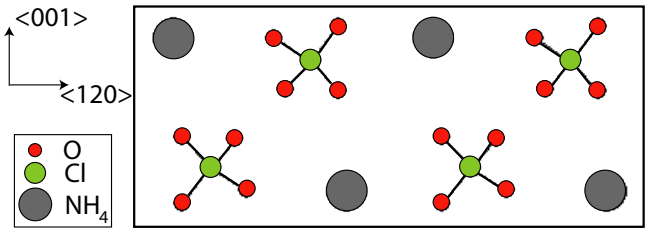

Figure 2.7: Projection of the unit cell on the {210} planes.

2.4 Etching Studies

In view of the fact that dislocation density and structure contributes to the thermal decomposition and shock initiation of detonation, Williams et al. [13], Herley et al. [14, 51], Raevskii et al. [28] and Beard et al. [52] focused their investigations on the occurrence and position of dislocations in AP using the most simple and widely used technique, namely the etch pit formation method.

The etching technique is the earliest and generally the cheapest and quickest recognized method for assessing structural perfection. It can be considered as the reverse of crystal growth and, when the etching is sufficiently selective, it is possible to remove atomic imperfections which can generate surface steps [46]. For example, spiral pits have been observed during chemical etching of germanium [46] and $YBa_2Cu_2O_{7-\delta}$ [53] (shown in Fig. 2.8(a)), while holes have been detected at dislocations in AlB_2 crystals [46]. There is little doubt that dislocations can be preferential sites for chemical attack, primarily because they are small regions of stress with a different energy potential [46].

Methods of etching include: thermal etching, chemical etching, solution etching, preferential oxidation, electrolytic etching and cathodic sputtering [54].

No well defined rule can be formulated for developing an etchant for a given material. Etchants are usually discovered on a purely empirical basis [55]. The relationship between the etchant and the pit shape and orientation is still not well understood, however, it must be pointed out that when the reaction is sufficiently slow it seems that there is a preference to reveal the close-packed cleavage planes. Moreover, if the etching process is related to the crystal growth, it is reasonable to suppose that the shape and orientation of the pits are governed by the geometry and energetics of the growth process. On the other hand, the characteristics of the pits could be governed by the chemistry or thermodynamics of the etching process itself.

Figure 2.8 shows different shapes of pits which have been observed [14].

Johnston [59] has extensively studied the etching process and has observed that frequently the sides of the etch pits do not correspond with crystallographic planes, and in some cases the sides may have some curvature. In general, the pit faces are not low index crystallographic planes.

Johnston [59] has suggested that dislocation etch pits are generally pyramidal with the apex of the pyramid lying on the dislocation line, and the center of the base located at the original intersection of the dislocation with the surface. The direction in which the dislocation is aligned can be obtained by drawing an imaginary line from the base of the pyramid to its apex. A dislocation etch pit will deepen only so long as the dislocation is present. If the energy of the crystal solution interface is isotropic

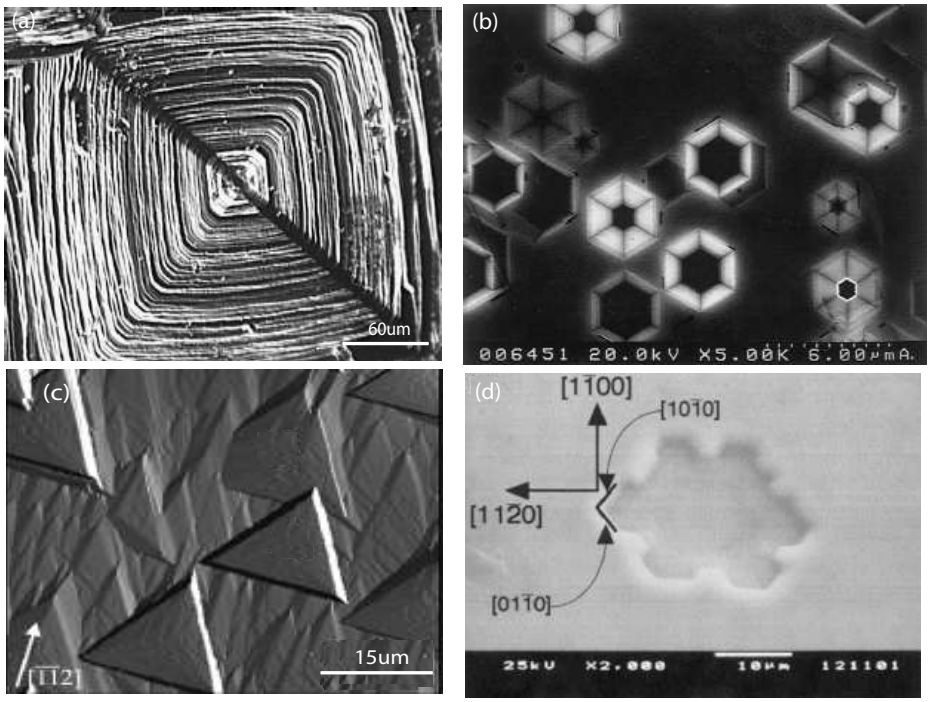

Figure 2.8: Different shape of etch pits observed: (a) Etch pit on (001) plane of $Ba_2Cu_2O_{7-\delta}$ using acetic acid [53]. (b) Etch pit on (111) plane of diamond using potassium nitrate [56]. (c) Etch pit on (0001) plane of GaN chemically etched by H_3PO_4 solution [57]. (d) Etch pit on (0001) plane of 6H-SiC etched by molten KOH [58].

the pit will be circular, if not the shape of the pyramidal base will tend to reflect crystal symmetry, as shown in Fig. 2.8. The etching behavior will depend critically upon the orientation of the surface. The orientation range, within which etch pits appear, depends upon the specific etchant.

The first etching investigation of AP was performed by Raevskii et al. [28] on the rhombohedral and cleavage planes, using 95.5% ethyl alcohol. A network of interacting dislocations on the cleavage planes was reported, as can be seen in Fig. 2.9(a) [28]. The dislocations were observed grouped close to mechanical damage and growth defects, as shown in Fig. 2.9(b). The dislocation density reported for cleavage planes was 10^6 cm^{-2}. A similarity between the anisotropic arrangement of dislocations and the anisotropy of the thermal decomposition was identified. Groups of dislocations close to the nucleus of thermal decomposition were also reported.

Williams et al. [13] in 1971 studied the formation of etch pits on the two cleavage planes, {210} and {001}, and on the growth plane (101), of AP using X-ray and high power interference contrast microscopy. The crystal was immersed in continuously agitated n-butanol for times varying from 5 to 30 sec at 295 K. On the {210} planes, rectangular etch pits were reported with the long edge parallel to the [001] direction, Fig. 2.10(a), and for the {001} planes, pyramidal etch pits were observed with their

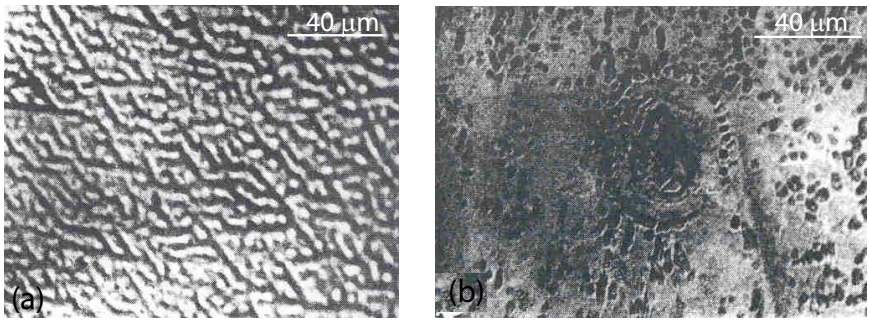

Figure 2.9: Pits observed by Raevskii et al. [28] using 95.5% ethyl alcohol: (a) Network of interacting dislocations on (001) plane. (b) Group of dislocations close to growth defects on (210) plane.

long axes parallel to [001] direction, as shown in Fig. 2.10(b). On the (101) plane, the pits were found to have the shape of an isosceles triangle with the base parallel to [001]. The dislocation density reported was between 0.1 - 5×10^6 cm^{-2}, with the lowest dislocation density observed on the {001} planes.

Herley et al. [14, 51] studied the formation of etch pits on the cleavage planes of AP using X-ray, optical and electron microscopy. For SEM examination, carbon replicas were used. The etchants used were 99% ethyl alcohol, pure n-butanol alcohol or a mixture of both. On the {210} planes, well oriented rectangular etch pits with their long side parallel to the [001] direction and their short side parallel to $[1\bar{2}0]$ were observed using n-butanol alcohol, which is the same shape and orientation as the pits observed by Williams et al. [13]. The size of these pits were approximately 2×8 μm. The dislocation density reported was between $2 - 8 \times 10^6$ cm^{-2}. Figure 2.11 shows that the short sides of the pits are shallow and the long sides are very steep. A terraced structure was reported inside the pits that can hardly be seen in Fig. 2.11. In contrast with Williams et al. [13], no well formed pits were observed on the {001} planes, instead a rapid and extensive reaction was observed. Best results were obtained with n-butanol although different kind of pits were observed with the

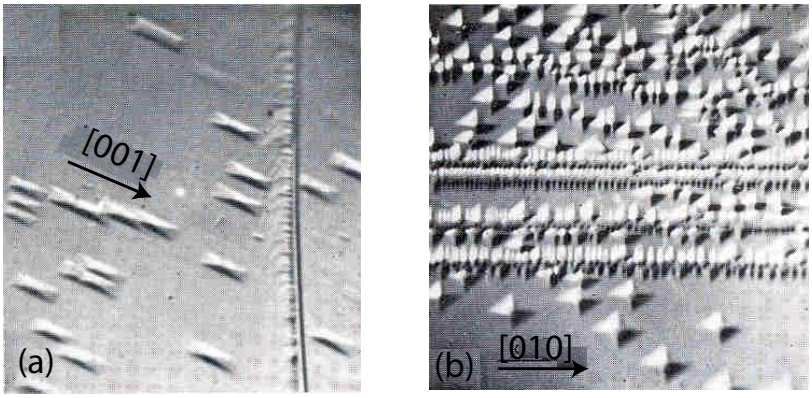

Figure 2.10: Pits observed by Williams et al. [13] using n-butanol: (a) Rectangular pits observed on the {210} planes. (b) Pyramidal etch pits observed on the {001} planes.

mixture of n-butanol and ethyl alcohol. Pits formed on the {001} planes with thermal etching when AP was heated in vacuum at 200°C were also studied. The pits obtained with this technique are similar in shape, size and density to those formed with ethyl alcohol.

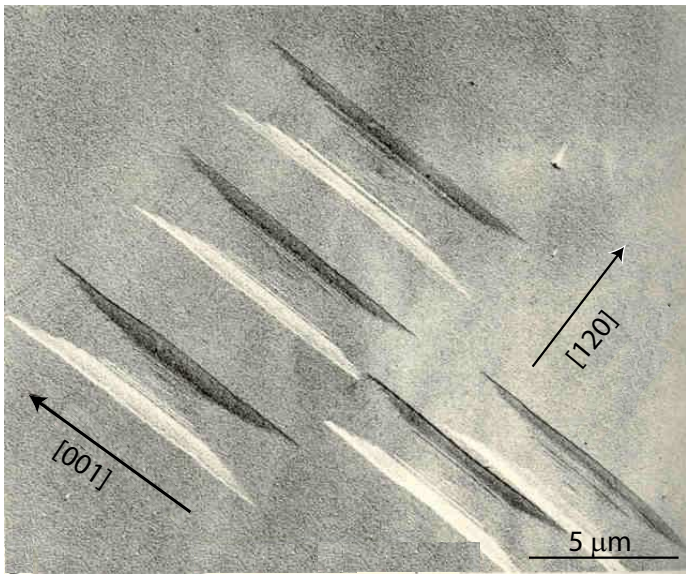

Figure 2.11: Electron microscope pictures of rectangular etch pits observed by Herley et al. [14] using n-butanol on the {210} planes.

2.5 Deformation by Slip

Plastic deformation usually occurs by sliding of portions of the crystal along certain planes (slip planes) [60]. Because of the translational symmetry of the crystal lattice, after the slip has occurred, the crystal structure is restored [45, 60]. This block-like nature of slip requires that the atoms move an integral number of atomic distances along the slip planes creating crystal offsets (slip steps). When we view the surface from above, the steps are seen as lines (slip traces). Slip traces are changes in surface elevation and AFM is a convenient tool to study these imperfections, being considerably more quantitative than slip trace characterization by optical methods.

Slip occurs on certain crystallographic planes in specific directions. The Peierls-Nabarro model predicts that the slip plane is the plane of greatest atomic density and the slip direction is the closest-packed direction within the slip plane [60]. For ionic crystals, there is an additional criterion that slip will not take place in directions which involve appreciable electrostatic repulsion [45]. Considering that such atomic movements would be energetically unfavorable, the number of potential slip systems is restricted. For example in alkali metal halides, the most active slip plane is the (110) even though the (100) is the plane with greatest atomic density. This is because there are strong forces between ions on the (100) plane whereas in the (110) plane the electrostatic effects are less pronounced [14].

Herley et al. [14] deduced by computation, using the crystal structure and considering electrostatic interactions, the most likely slip planes and slip directions in AP. The deduced slip systems were compared with slip traces and etch pit alignments observed on strained, large crystals, $2 \times 1 \times 1$ cm in size. The crystals were either compressed or indented with a sharp needle. The direction of the slip traces observed on the (210) and (001) planes are presented in Table 2.4. For example, in strained crystals the slip traces on the (210) plane were observed running parallel to the $\langle 121 \rangle$

direction and they were attributed to slip on the $(\bar{1}01)[010]$ system. The slip traces observed on the (001) plane are given in Table 2.4 and corresponded to high index planes which cannot be described as close packed. Herley et al. [14] concluded that, for the (001) planes, slip occurs rather readily in the [001] direction in almost any plane that contain the [001] axis. As a result the operative slip directions were identified as [010] and [001] which correspond to the shortest possible lattice vectors. The slip systems based on alignment of etch pits were also deduced. The principal systems identified are presented in Table 2.5.

Williams et al. [13] performed a similar investigation based on calculation of slip systems and observations of slip traces and etch pit alignment (Table 2.6) concluding that the following systems are active: $(201)[010]$, $(20\bar{1})[010]$, $(401)[010]$, $(40\bar{1})[010]$, $(010)[010]$, $(110)[010]$ and $(\bar{1}10)[010]$. The $(011)[0\bar{1}1]$ and $(100)[010]$ were considered as unlikely based on the electrostatic criterion.

The most recent investigation on the mechanical properties of AP was performed by Elban and Armstrong [8] using micro-indentation hardness testing on a single crystal of AP. The slip traces and cracks formed on the (210) and (001) planes were analyzed. A Vickers hardness number (VHN) of 13, corresponding to a Vickers hardness of 0.127 GPa was obtained for the (210) plane. The impression obtained was not equiaxed and a cleavage crack was observed aligned with the [120] direction, as seen in Fig. 2.12(a). The asymmetry of the impression was attributed to different slip systems activated in the total strain field. A very shallow trough was observed

Plane	**Direction of slip traces**
(210)	$\langle 121 \rangle$
(001)	[100], [110], [140], [180], [210]

Table 2.4: Direction of slip traces on the cleavage planes of AP observed by Herley et al. [14].

Etch pit alignment	**Slip plane**	**Interplanar spacing (Å)**	**Slip direction**	**Unit Burger vector (Å)**
[001]	(100)	9.202	[001]	5.816
	(010)	5.816	[001]	7.449
	(110)	4.916	Nil	-
$[1\bar{2}0]$	(001)	7.449	[010]	5.816
$[2\bar{4}1]$	$(\bar{1}02)$	3.452	[010]	5.816
	(112)	2.969	[110]	10.886
$[1\bar{2}1]$	$(\bar{1}01)$	5.790	[010]	5.816
	(012)	3.136	Nil	-
$[1\bar{2}2]$	(011)	4.584	Nil	-
	$(\bar{2}01)$	3.914	[010]	5.816
$[1\bar{2}3]$	$(\bar{1}11)$	4.103	Nil	-
	$(\bar{3}01)$	2.836	[010]	5.816
$[1\bar{2}4]$	$(\bar{2}11)$	3.247	Nil	-
	(021)	2.709	Nil	-
	$(\bar{4}01)$	2.198	[010]	5.816

Table 2.5: Possible slip systems in AP deduced from etch pits observation on the (210) plane [14].

extending in the $\langle 001 \rangle$ direction. The troughs observed in the impression on the (210) plane were attributed to $\{111\}$ $\langle 10\bar{1} \rangle$ and $(010)[\bar{1}00]$, although the last slip system was considered as unlikely by Herley et al. [14].

On the (001) plane a lower Vickers hardness number of 11 (0.108 GPa) was found. The impression shown in Fig. 2.12(b) exhibits a two fold rotational symmetry and

Plane	Etch pit alignment	Slip traces
(210)	[001]	[$\bar{1}$20]
	[$\bar{1}$22] and [1$\bar{2}$2]	[$\bar{1}$22] and [1$\bar{2}$2]
	[$\bar{1}$24] and [1$\bar{2}$4]	[$\bar{1}$24] and [1$\bar{2}$4]
(001)	[100]	[100]
	[010]	[010]
	[110] and [$\bar{1}$10]	[010]

Table 2.6: Summary of etch pit alignments and slip traces observed by Williams et al. [13].

the perimeter of the impression exhibits a particular waviness that is related to cracks running from the impression aligned to the [010] direction. A very shallow trough was observed extending in the ⟨010⟩ direction. The trough was attributed to ±(100)[001] slip and secondary slip traces observed on the trough were recognized as a result of ±(010)[001] slip.

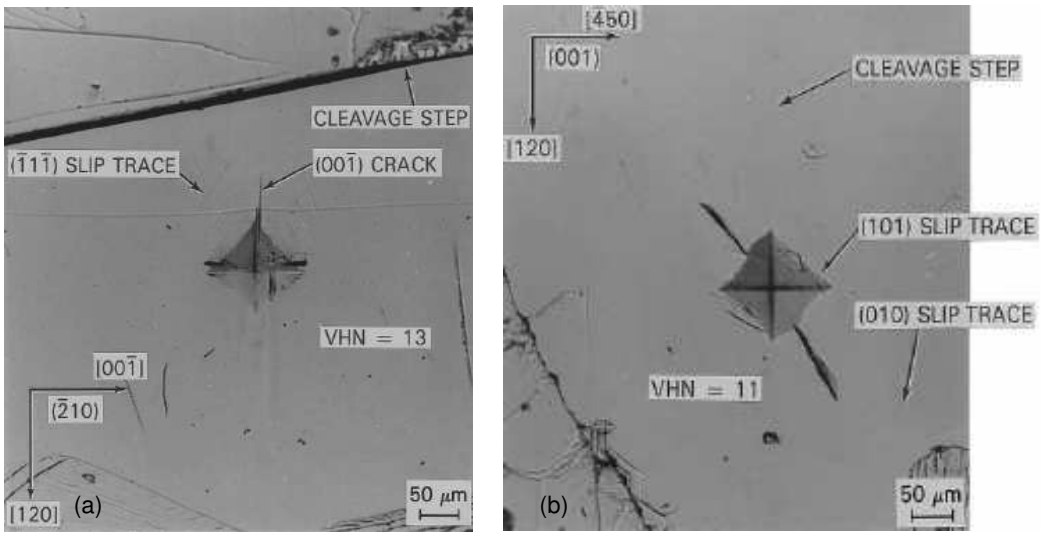

Figure 2.12: Vickers hardness impressions: (a) on the (210) plane, (b) on the (001) plane, viewed in transmitted light [8].

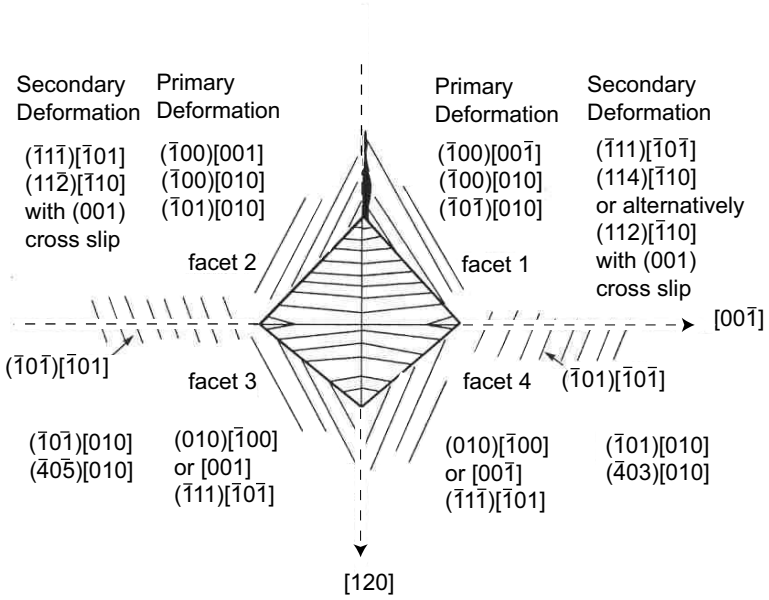

Figure 2.13: Primary and secondary slip systems involved in Vickers indentation on the (210) plane [8].

Figure 2.13 summarizes the principal and secondary slip systems inferred by the impressions on the (210) plane. Secondary slip systems are considered to operate beyond the facets and are responsible for the slip traces enclosing the indentation shown in Fig. 2.13. Cross slip is proposed because of waviness and variations of individual slip traces.

2.6 Nanoindentation

2.6.1 Introduction

The advent of instrumented indentation, also referred as "nanoindentation", has enabled the study of load vs. penetration depth at nanometer length scales. Indentations at this scale make possible the determination of mechanical properties of thin films or small volumes of material. Nanoindentation has been referred to as the next generation of hardness testing [61].

Instrumented indentation has been successfully developing during the last decade and it is now an accepted component of the mechanical characterization field in a wide variety of disciplines including materials science, physics, chemistry, biology and medicine [62].

Hardness testing has been the most used mechanical test since its introduction at the beginning of the 20th century. There have been low load variations of the test from its beginning, usually referred as micro-hardness testing [63]. The micro-hardness test has been employed to measure surface mechanical properties, however there are significant limitations when this technique is applied to thin films or surface regions less than several micrometers. Motivated by the necessity to characterize surface regions in the nanometer range, significant efforts in the development of instrumented indentation have been made [64]. Nanoindentation instruments have the advantage of providing not only surface hardness but also offer the capability to obtain elastic and time-dependent material properties of the surface. Depending on the specifications of the system, forces as small as 1 nN and displacements of 1 Å can be measured [65]. Nanoindentation has successfully been used to determine elastic modulus and hardness [66]. Instrumented indentation testing has also been used to evaluate yield stress and strain hardening characteristics of metals [67], damping and internal friction in polymers [68], residual stresses [69], stress exponents for creep [70] and fracture toughness [71].

Whereas the use of nanoindentation is continually increasing, advances toward absolute quantification and standardization will require advances in instrument calibration, measurement protocols, and analysis techniques [72]. Until now the only standard available for instrumented indentation testing (IIT) is the one proposed by the International Organization for Standardization (ISO): ISO 14577-1, ISO 14577-2 and ISO 14577-3 [73–75] . Additionally the American Society of Testing Materials (ASTM) has assigned the work item WK382: practice for instrumented indentation

testing, to subcommittee E28.06.11, with the purpose of establishing the basic parameters of instrumented indentation testing [76].

2.6.2 Analysis of Indentation Data

The most commonly measured parameters using nanoindentation are the hardness, H, and the elastic modulus, E. It is common to use the Oliver and Pharr method [66] to analyze the load-penetration depth data. The model expands on ideas developed by Loubet et al. [77] and Doerner and Nix [78] considering the deformation of an elastic half-space by an elastic punch, although the Oliver-Pharr model is not constrained by the assumption of a flat punch indenter geometry. The unloading data is analyzed based on this model that relates the projected contact area at the peak load to the elastic modulus, considering the deformation of an elastic half-space by an elastic punch. Once the projected contact area is estimated from the indenter area function, it is possible to calculate E and H.

The problem of determining the stress distribution within an elastic half-space when it is deformed by a rigid punch was first considered by Boussinesq in 1885 [79]. Using methods based on potential theory, Boussinesq derived the solution for the case of the penetration of a half-space by a rigid solid of revolution whose axis was normal to the original boundary of the half-space. Based on Boussinesq's work, Love [80, 81] derived partial numerical solution for the cases of a flat-ended cylindrical punch and a conical punch.

The results of Sneddon [82], who derived a general relationship among the load, displacement and contact area for any punch that can be described as a solid of revolution of a smooth function, have also been used in the Oliver-Pharr analysis. Sneddon [82] showed that the load-penetration depth relationships for many simple punch geometries can be written as:

$$P = \alpha h^m \tag{2.5}$$

where P is the load applied to the sample, h is the elastic displacement of the sample, and α and m are constants where m depends on the geometry of the indenter.

Tabor [83] investigated the effects on plasticity in indentation observing the elastic recovery of indentation impressions. Tabor [83] noted that the permanent indentation left in a metal surface by an spherical indenter has a larger radius of curvature than that of the indenter, and the imprint left by a conical indenter is still conical with a larger include tip angle, this effect was referred to as the release of elastic stresses in the specimen. Since the "recovery" is truly elastical, Tabor [83] applied the classical laws of elasticity for each geometry and showed that the shape of the entire unloading curve and the total amount of recovered displacement can be accurately related to the elastic modulus and size of the contact impression for both spherical and conical indenters. In the early 1970's, Bulychev et al. [84] analyzed the load-penetration depth data obtained from instrumented micro-indentation hardness according to the following equation:

$$S = \frac{dP}{dh} = \frac{2}{\sqrt{\pi}} E_r \sqrt{A} \tag{2.6}$$

where $S = dP/dh$ is the experimentally measured stiffness obtained from the unloading data, E_r is the reduced modulus, and A is the projected contact area of the elastic contact. Equation (2.6) is founded on the classical theory of elasticity and although it was derived for a conical indenter, Bulychev et al. [84] showed that holds well for spherical and cylindrical indenters and also noted good agreement for pyramidal indenters. Furthermore, Oliver and Pharr [85] have shown that the equation also applies to any indenter that can be described as a body of revolution of a smooth function . The fact that the equation works well for some indenters that cannot be described as bodies of revolution has been confirmed by finite element calculations performed by King [86].

Tabor's [83] experiments also resulted in the definition of a reduced modulus, E_r, to account for the fact that elastic deformation occurs in both the indenter and the

specimen. The reduced modulus is given by:

$$\frac{1}{E_r} = \frac{(1-\nu^2)}{E} + \frac{(1-\nu_i^2)}{E_i} \tag{2.7}$$

where E and ν are the elastic modulus and Poisson's ratio for the specimen and E_i and ν_i, are the same parameters for the indenter.

In order to obtain the reduced modulus (Eq.(2.6)) and the hardness we must solve for the projected contact area of the impression, A. For small indentations, measuring the projected contact area optically is a difficult task. To avoid this difficulty Pethica, Hutchings and Oliver [87, 88] suggested a simple method based on a previous knowledge of the projected contact area as a function of the penetration depth and measured load vs. penetration depth curve. This method is based on the fact that the deformation process occurs producing an impression that conforms to the shape of the indenter. If the depth is known by the load-penetration depth data, the projected contact area can be determined from the shape function. Three depths can be distinguished in Fig. 2.14: the depth at the peak load, h_{max}, is the maximum depth reached during indentation; the final depth, h_f, is the residual depth left of the impression after unloading; and the contact depth evaluated at the peak load but considering the elastic deformation of the surface h_c, which is less than the maximum depth of penetration h_{max}.

The deflection of the surface at the contact perimeter depends on the indenter geometry and based on Sneddon's model [82] for a conical indenter the contact depth can be estimated by [66]:

$$h_c = h_{max} - \frac{\pi - 2}{\pi}(h - h_f) = h_{max} - \frac{2(\pi-2)}{\pi}\frac{P_{max}}{S} = h_{max} - \epsilon\frac{P_{max}}{S} \tag{2.8}$$

where $\epsilon = 0.72$ and is defined as a geometric constant. When similar arguments are made for the paraboloid of revolution or the flat punch, a equation similar to Eq.(2.8) is obtained but with a different geometric constant. For a flat punch $\epsilon = 1.0$ and for a paraboloid of revolution $\epsilon = 0.75$ [66]. Experiments with Berkovich indenters

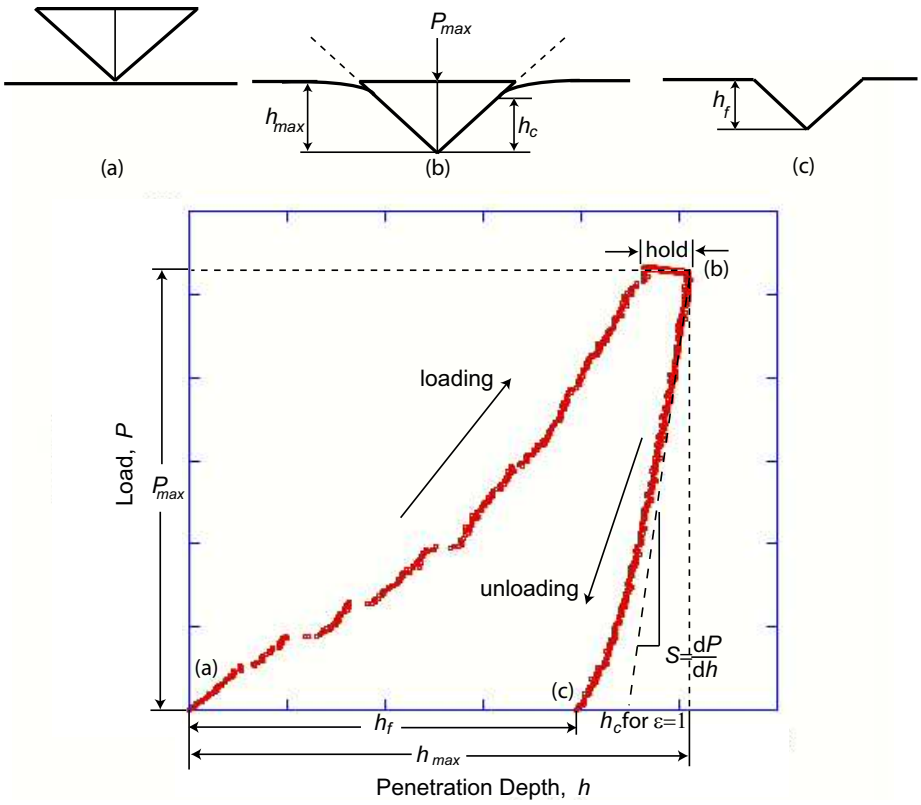

Figure 2.14: Typical load vs. penetration depth curve showing the schematic representation of the indentation process: (a) Original surface profile (b) Surface profile under maximum load (c) Surface profile after load removal.

have shown that Eq.(2.8) also works well with $\epsilon = 0.75$ [65]. This observation has been explained using elastic-plastic analysis and finite element simulation [89]. Pharr and Bolshakov [90] calculated this parameter for a Berkovich indenter using a finite element simulation and obtained a value close to 0.76.

The projected contact area, A, is estimated by evaluating an empirically determined indenter shape function, $f(h)$, which relates the cross-sectional area of the indenter to the distance from its tip. The calibration procedure for the determination of machine compliance and indenter area function is an iterative one and is described in Appendix C. Once the contact depth is calculated (Eq.(2.8)) the projected contact area of the hardness impression can be determined evaluating the area function of

the indenter at the contact depth (h_c) viz.:

$$A_c = f(h_c) \tag{2.9}$$

The hardness is defined as a measure of the load bearing capacity of the contact computed by dividing the applied load by the projected contact area under maximum load [65], viz.,

$$H = \frac{P_{max}}{A_c} \tag{2.10}$$

The unloading stiffness is estimated by differentiating a fitting of the unloading curve of the form of the Eq.(2.5) and evaluating the derivative at the peak load and displacement. Then the elastic modulus can be calculated using Eq.(2.6), viz.,

$$E_r = \frac{\sqrt{\pi}}{2}\frac{S}{\sqrt{A_c}} \tag{2.11}$$

2.6.3 Pop-in

The abrupt increase in penetration at a given load, referred to "pop-in" [91], is shown on the load vs. penetration depth curve in Fig. 2.15. This behavior has been observed in a large variety of materials including metals [92,93] and semiconductors [94,95]. It has been attributed to the sudden nucleation of dislocations [91], oxide layer breakthrough [92], phase transformation [96,97], or motion of individual shear bands [98].

Multiple pop-in events have been reported before in indentation studies of sapphire [99], GaN [100], ZnO [95, 101], tungsten [93], Pd and Zr-based bulk metallic glasses [98]. Kucheyev et al. [101] have attributed multiple pop-in to the fact that beyond the elastic-plastic threshold the material starts to deform plastically via slip and involves the generation of dislocations that will follow the directions of easy slip but may be impeded as a result of interactions between slip systems. At some point the

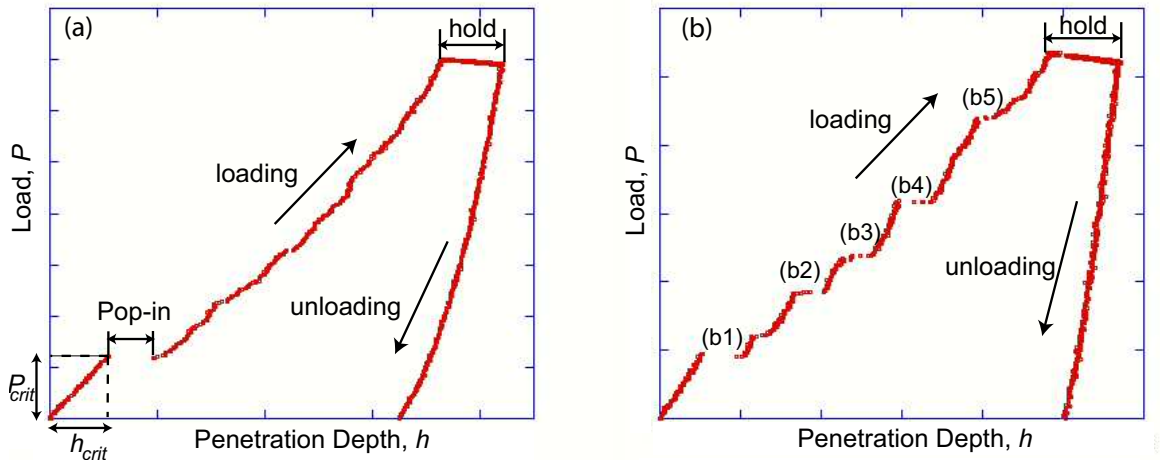

Figure 2.15: Typical load versus penetration depth curves showing: (a) single pop-in event, and (b) multiple pop-in events (b1 - b5).

further propagation of indentation-produced dislocations will be obstructed. Therefore, further plastic deformation must involve the nucleation of more dislocations, resulting in multiple pop-in events. It has also been pointed out that the displacement in each pop-in is a function of the instantaneous depth of the indenter [98]. This phenomenon has be explained by the fact that more elastic energy is stored in the material when a higher load is reached before the first pop-in [98].

The arguments that have been made for attributing pop-in to the yield point of the material and the sudden nucleation of dislocations are essentially three: 1) the observation of elastic behavior before the onset of pop-in. The unloading curve traces the loading curve and an AFM image of the area shows no evidence of deformation or cracking. 2) there is agreement between the maximum shear stress under the indenter and the theoretical shear strength [60]. 3) there is agreement between the load vs. penetration depth curve before the first pop-in and the initial loading curve when modeled as the elastic loading of two spherical bodies, where the load is related to the displacement by [93, 102]

$$P = \frac{4}{3} E_r \sqrt{R\delta^3} \tag{2.12}$$

here P is the load, R the radius of the indenter tip if the sample is planar, δ is the

depth of penetration, and E_r is the reduced modulus defined in Eq.(2.7).

Wang et al. [102], Chiu and Ngan [103], Lucca et al. [95, 104], Bahr et al. [93], Yu et al. [105] and Caceres et al. [106] using a Hertzian contact model evaluated the maximum stress under the indenter. For elastic loading of a sphere on a semi-infinite solid, the maximum pressure is:

$$P_m = \left(\frac{6E_r^2}{\pi^3 R^2}\right)^{\frac{1}{3}} P^{\frac{1}{3}} \tag{2.13}$$

Based on the continuum contact mechanics the most highly stressed point will be located $0.48a$ below the free surface, where a is the radius of contact between the tip and the sample, and the maximum stress will be equal to [107]:

$$\tau_{max} = 0.31P_m = 0.18\left(\frac{PE_r^2}{R^2}\right)^{\frac{1}{3}} \tag{2.14}$$

once the maximum shear stress under the indenter has been calculated it can be compared with the theoretical value [60]:

$$\tau_{theo} = \frac{G}{2\pi} \tag{2.15}$$

In order to understand the pop-in numerous studies has been performed varying conditions that can affect this phenomenon. Among these are the topography of the surface of the sample, environmental conditions, indentation time, velocity of engagement and indenter geometry. Bahr et al. [93] and Oden et al. [108] have studied the relation of crystal orientation, dislocation density and oxide film thickness to the occurrence of pop-in. Moreover, the influence of variation in roughness [109], the temperature [110], the relative humidity [111], the loading rate [98], the velocity of the engagement [112], the radius of the indenter [111] and creep [113] have been studied in relation to pop-in.

2.6.4 Indentation Size Effect (ISE)

In the last years several experimental measurements of nanohardness and microhardness of metals, non-metals and ceramics have been made. Many of the investigations have reported that the hardness increases with decreasing the penetration depth [95,109,114–119]. Figure 2.16 depicts this ISE. Although there are other investigations in which no significant variation in hardness with indenter load have been reported [66] or a reduction in hardness was observed with decreasing the depth of penetration [120, 121].

Fleck et al. [115] indicated that the increase in hardness with decreasing load can be explained by a strain gradient plasticity. In this theory, two types of dislocations accommodate strain: statistically stored dislocations (ρ_s) and geometrically necessary dislocations (ρ_G) [115, 122]. The simplest possible dimensionally correct relationship between flow stress (τ) and the density of dislocations is [115]:

$$\tau = CGb\sqrt{\rho_s + \rho_G} \tag{2.16}$$

where C is a constant taken to be $1/3$, G is the shear modulus and b is the magnitude of the Burgers vector [114]. The density of geometrically necessary dislocations is

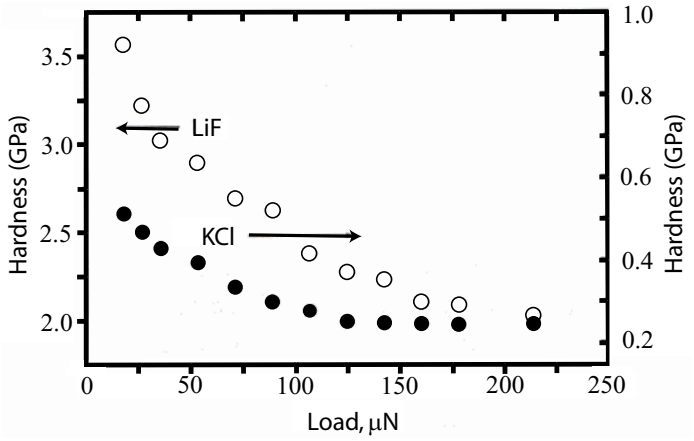

Figure 2.16: Indentation size effect observed on LiF and KCl single crystals [119].

inversely related to the depth of indentation and can be obtained by [114]:

$$\rho_G \approx \frac{4\gamma}{bD} \tag{2.17}$$

where D is the diameter of the indent γ is the average strain. The hardness can be estimated as about three times the flow stress for fully developed plastic flow, and so Ma and Clarke [114] obtained:

$$H \approx Gb\left[\rho_s + \frac{4\gamma}{bD}\right]^{1/2} \tag{2.18}$$

here the density of statistically stored dislocations does not depend on the depth of the indentation and is evident in Eq.(2.18) that hardness in inversely proportional to the square root of the size of the indentation.

Lately, Lim and Chaudhri [123] performed nanoindentation experiments on both annealed oxygen-free polycrystalline work-hardened copper and found that none of the models based on the strain gradient plasticity theory is applicable. Another study has attributed the decrease in hardness with penetration depth to a non-negligible tip defect at small depth penetration [124].

2.6.5 Surface Roughness

The surface roughness is very important in nanoindentation because the mechanical properties are deduced from contact depth and area function on the assumption that the surface is flat and smooth. If the surface is rough, multiple area contacts between the indenter tip and asperities of the surface are formed instead of a single contact. The roughness describes the deviation from the nominal surface in the form of finely spaced irregularities. Analysis of the surface roughness is usually performed either by stylus profilometry or by atomic force microscopy [125, 126]. An average of the deviation between the mean and actual surface comprises the roughness number. The arithmetic (R_a) or root mean square (R_q) averages are used:

$$R_a = \frac{1}{L}\int_0^L |y|\, dx = \frac{\sum y}{n} \tag{2.19}$$

$$R_q = \sqrt{\frac{1}{L}\int_0^L y^2 dx} = \sqrt{\frac{\sum y^2}{n}} \tag{2.20}$$

where y represents deviations from the center line of the surface, and n the number of such values, and L is the length over which y is averaged.

Chapter 3

Experimental Techniques

The {210} and {001} planes of high purity commercial ammonium perchlorate crystals were studied in this investigation. The surfaces were obtained by cleaving and the crystallographic orientation of the surfaces was determined by etching. Nanoindentation was performed using a load-controlled commercial nanoindenter in conjunction with an scanning force microscope (AFM) system (Appendix D). A Berkovich diamond indenter was used for the measurement of the elastic modulus and hardness and a spherical and a cube corner indenter were also used for the study of the plastic deformation behavior.

3.1 Sample Preparation

High purity commercial AP (99+%) crystals grown at room temperature from aqueous solution were investigated. These crystals are the same type of crystals used in the preparation of solid propellant at Politecnico di Milano.

AP was stored at low temperature (4°C) in a closed container. Before each experiment a few crystals were chosen and allowed to reach room temperature. Only optically transparent and well shaped crystals were selected of typical size 400 ($\pm$50) μm $\times$ 500 ($\pm$50) μm $\times$ 600 ($\pm$50) μm. The nanoindentation samples were then obtained

by cleaving the crystals using a sharp blade and handling very carefully to avoid any contact with the fresh new surfaces. The surfaces used were free of inclusions.

Each of the cleaved crystal halves was then mounted on different glass slides, using a very thin layer of glycol pthylate. Glycol pthylate was selected because: it does not react with AP, the temperature needed to melt it is below the decomposition temperature of AP, and it is transparent. One of the mounted samples was placed inside the AFM enclosure in order to perform nanoindentations and the other one was etched in order to identify crystallographic orientation of the surface. The inclination angle of the nanoindentation sample surface was checked using the AFM and if the cleaved surface was inclined more than one degree the sample was removed and re-mounted or the sample was discarded [73].

The samples were transported in containers with a desiccant and all handling operations were done as quickly as possible to limit environmental contamination of the samples.

3.2 Etching Process

In the present study chemical etching was performed to identify crystallographic planes and directions on the AP samples, and to study the internal structure of etch pits by AFM. Different etchants were tested on AP crystals based on previously reported etchants in the literature [13,14,28,51,52,127]. The best results were obtained by etching with 100% n-butanol, previous studies using this etchant were performed by Herley et al. [14] and Williams et al. [13].

The etchant was at room temperature and the crystals were etched for 6 - 10 sec. Immediately after this compressed nitrogen was blown onto the surface to stop the etching of the sample. Etched samples were observed using the optical microscope and the AFM. Based on the etching and X-ray results obtained by Herley et al. [14]

and Williams et al. [13] the crystallographic planes and directions were identified by the shape and the relative orientation of the etch pits. The etch pit density (EPD) was measured with the AFM by averaging the EPD values in ten different locations of the crystal and for different crystals. The areas selected had a size of 30 μm $\times$ 30 μm and only well developed pits were considered. The samples were also etched after indentation in order to study the alignment of special features such as cracks, pile-up, slip traces, and pits around the indentations impressions.

3.3 Nanoindentation Instrument

The nanoindentation system is composed of a load-controlled commercial nanoindenter (Hysitron, Inc.) and an atomic force microscope (Digital Instruments Dimension 3100 SPM System). The combination of these two systems enables the nanoindentation system to take scanning force images of the sample surface by using the same diamond tip for imaging and for indentation.

A block diagram of the nanoindentation system is presented in Fig. 3.1. The nanoindentation system includes a signal adapter, a piezo electric tube scanner, a controller, a three plate capacitative load-displacement transducer and an indenter. The indenter is fixed to the transducer which applies a desired load to the indenter and measures the displacements of the indenter in the vertical direction (z direction).

The maximum load of our nanoindentation system is approximately 10 mN. The noise floor for the force has been reported as 100 nN while the noise floor for the displacement is less than 0.2 nm. This allows indentations with load less then 25 μN and indentation depth less than 5 nm to be made.

The central part of the TriboScope nanoindentation system is a three plate capacitive force-displacement transducer, shown in Fig. 3.2. It consists of two fixed drive plates and a pick-up electrode, which is mounted to the housing by suspension

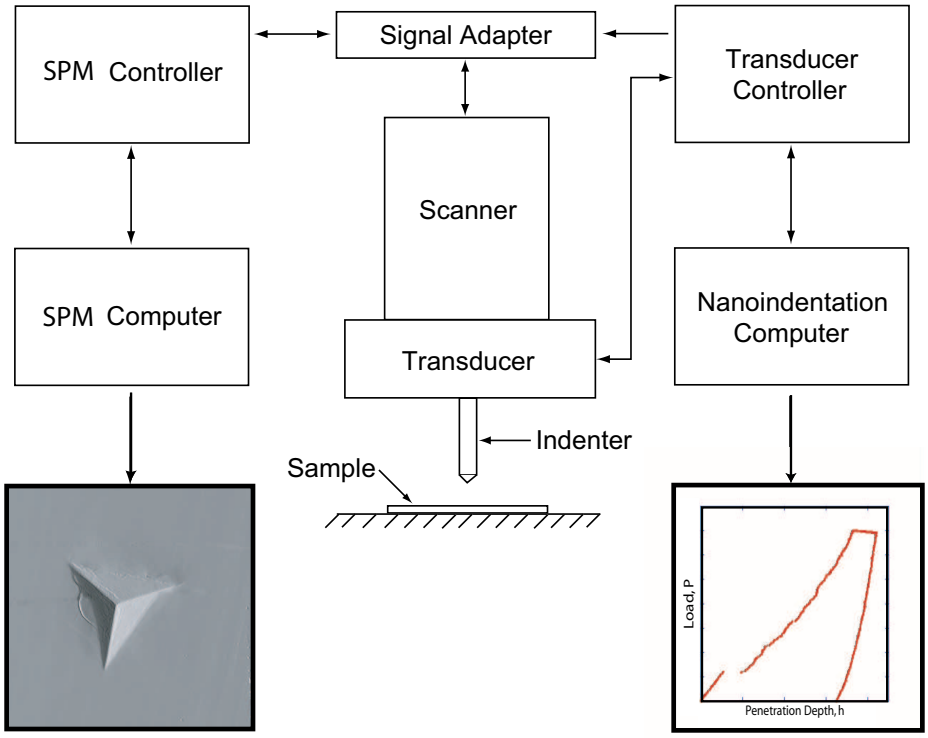

Figure 3.1: Block diagram of the nanoindentation system.

springs. The indenter is mounted to the pick-up electrode, which moves vertically. To generate a force, a voltage is applied to the drive plates which creates an electric field between them and an electrostatic force is generated on the pick-up electrode. The amount of this force, F_{el}, is proportional to the square of the voltage applied to the drive plate, V [128]:

$$F_{el} = k_e V^2 \tag{3.1}$$

where k_e is an electrostatic force constant, which depends on the plate area and the distance between drive plate and pick-up electrode. The displacement is obtained by measuring the capacitance between each of the drive plates (C) and the pick-up electrode, using the equation:

$$d = \frac{A\epsilon_o\epsilon_r}{C} \tag{3.2}$$

where C is the capacitance, A the area of the capacitor, ϵ_o is the permittivity of free space, ϵ_r is the relative permittivity of the air, and d is the distance between two plates.

A part of the electrostatically generated force is supported by the suspension springs of the pick-up electrode. This part must be subtracted from the electrostatically applied force to obtain the actual force applied to the sample, F_s:

$$F_s = F_{el} - k_s h \tag{3.3}$$

where h is the displacement of the pick-up electrode and k_s is the spring constant of the suspension.

Indenters are typically made of a hard, stiff material such as diamond ($E = 1141$ GPa [66]) and sapphire ($E = 400$ GPa [62]). Indenters are ussually of either spherical shape or pyramidal. Pyramidal indenters include those having four sides (Vickers, Knoop) and those having three sides (Berkovich, cube corner). In order to measure the mechanical properties of the AP, a Berkovich indenter, which is widely utilized to measure mechanical properties at the nanometric scale was used. The geometry of an ideal Berkovich indenter is shown in Fig. 3.3 with a nominal angle of 65.3° between the face and the normal to the base at the apex (face angle), and an angle of 76.9° between the edge and the normal (apex angle).

The main defect of the four-sided square (Vickers indenter) and rhombic (Knoop indenter) pyramid indenters used in micro-hardness testing is the manufacturing dif-

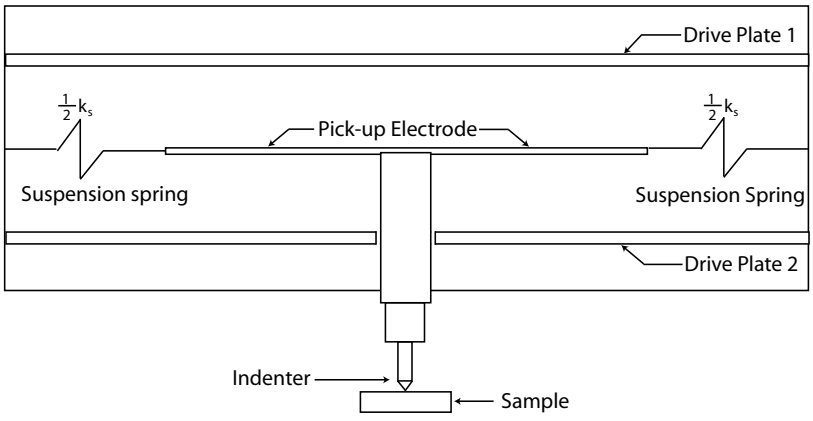

Figure 3.2: Schematic of the three plate capacitive force-displacement transducer of the Hysitron TriboScope.

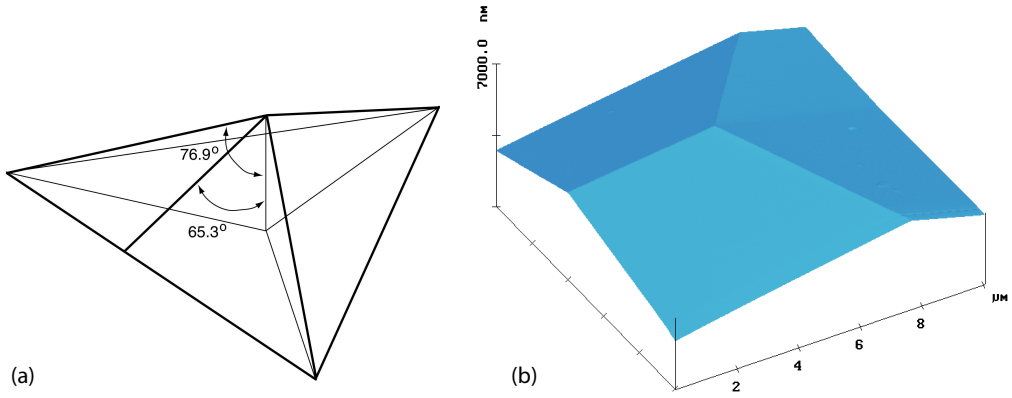

Figure 3.3: Berkovich indenter: (a) Geometry, and (b) AFM image.

ficulty of producing a four sided pyramid with all four facets meeting in a common point. In general, between two opposite faces of the indenter a ridge is formed like the crest of a roof [129]. This fact led to the idea to use a diamond pyramid with a sharply pointed tip for first time in 1951 by E. S. Berkovich [129].

Two types of Berkovich indenter exist: the standard Berkovich with the same ratio of actual surface area to indentation depth as a Vickers indenter and the modified Berkovich indenter with the same ratio of projected contact area to indentation depth as the Vickers indenter. A modified Berkovich indenter was used in this investigation.

A cono-spherical indenter was used in some of the experiments to avoid the stress concentration caused by the edges of the Berkovich or cube corner indenters. The cono-spherical indenters are conical shaped tips with a spherical end. The cono-spherical indenter used in this study had a nominal radius equal to 3 μm and a cone angle of 120°.

Experiments were also performed using a cube corner diamond tip, which is a three-sided pyramid with 90° total included tip angle. The geometrical description of the Berkovich and cube corner indenter is presented in Table 3.1. This tip is sharper than a Berkovich indenter and leads to a higher stress concentration under the indenter, so that the elastic-plastic transition occurs at lower loads.

	Symbol	Berkovich	Cube Corner
Face angle	β	65.3°	35.3°
Apex angle	γ	76.9°	54.7°
Projected area	A_{proj}	$24.5h^2$	$2.6h^2$
Ratio of the projected to the surface area	A_{proj}/A_{surf}	0.91	0.58

Table 3.1: Description of the Berkovich and cube corner indenters.

Because the nanoindentation instrument is not perfectly rigid, the measured displacement of the indenter is the sum of the penetration of the indenter into the specimen and the displacement of the instrument itself. The compliance of the nanoindentation istrument, also called the load-frame compliance, is obtained by making a series of indentations in reference materials, as outlined in Appendix C. All of the raw data is corrected for the load-frame compliance.

Thermal drift calibration is used to adjust the measured displacements to account for small amounts of thermal expansion or contraction in the test material and indentation equipment. To measure the thermal drift rate a small fixed load is applied to the sample and the displacement of the indenter is measured. The measured drift rate for all experiments was less than 0.1 nm/sec averaged over a 5 sec interval. All the displacements measured during the indentation test are corrected according to the measured thermal drift rate.

3.4 Procedure for Nanoindentation Experiments

A detailed explanation of the procedure used for the nanoindentation experiments is given in Appendix E, only a brief description will be given here. Before experiments

were performed the cleanliness of the indenter was checked by carefully inspecting it under an optical microscope. If any debris was found on the indenter, it was cleaned with methanol/ethyl alcohol solution and re-examined with the optical microscope.

The sample was positioned under the indenter away from the edges of the sample and close to relative flat regions. In order to minimize the surface degradation reported by Yoo et al. [15] the humidity in the indentation chamber was maintained below 12% during all the experiments by putting desiccant inside the indentation chamber before loading the sample and each crystal was used for less than six hours. After the sample is placed in the indentation chamber, the sample and instrument are allowed to thermally equilibrate, which typically takes about an hour

Prior to each indentation the indenter tip was used to scan a 25 μm x 25 μm region of the surface. The region for indentation was chosen with the criteria that there were relatively smooth large areas of the cleaved surface, free of cleavage steps. After the region was selected a 1 μm x 1 μm scan was performed to more closely examine the area to be indented. A Berkovich diamond indenter was used for the measurement of the elastic modulus and hardness. The sample was indented using the load function shown in Fig. 3.4, consisting of a loading and unloading cycle. The maximum loads applied were: 60 μN, 100 μN, 150 μN, 250 μN and 500 μN. Most all of the experiments used a loading and unloading rate of 20 μN/sec however different unloading rates were used to evaluate the effect of this variable in the results. A hold period was introduced at peak loads to reduce the effect of creep. To avoid any interference with neighboring indents successive indentations were separated at least 25 times the maximum depth [65].

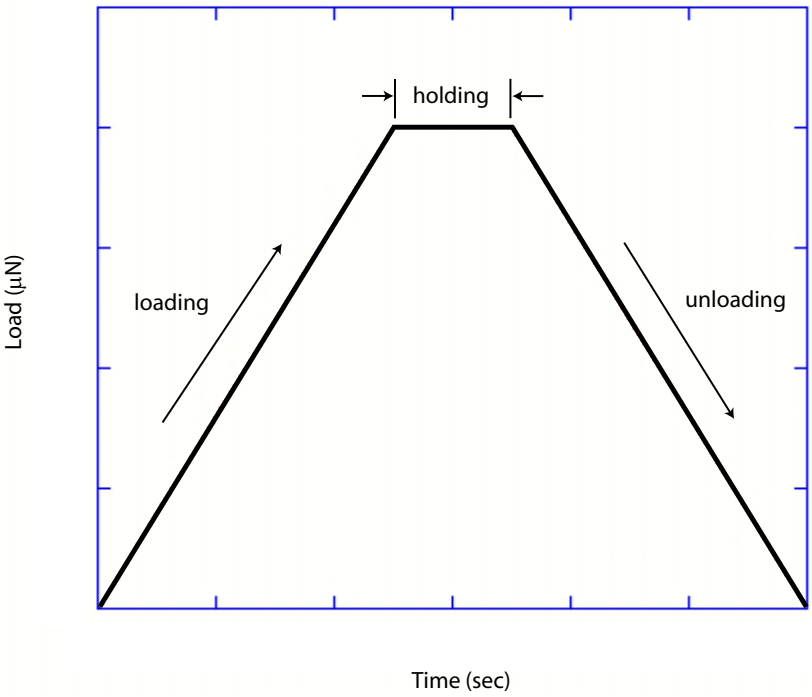

Figure 3.4: Load pattern used.

Chapter 4

Results and Discussion

4.1 Optical and AFM Examination of Cleaved Surfaces

4.1.1 Surface Roughness

A AFM was used to measure the roughness of the surfaces to be indented. Figure 4.1 shows a typical 1 μm x 1 μm AFM image of the surface topography of the {001} planes. The roughness for this surface was 1.1 nm R_q and 0.92 nm R_a. The lines that give an appearance of scratches on this image are not a feature of the surface, but an artifact of the AFM scanning process. The image shown is representative of AFM images obtained for all samples and similar artifacts and features were observed in all scans. The average R_q roughness from 25 1 μm x 1 μm AFM scans on each {001} and {210} planes were 1.3 $\pm$ 0.3 nm and 1.2 $\pm$ 0.3 nm respectively. The samples were smooth enough so that the surface roughness did not significantly affect the measured elastic modulus and hardness. Moreover, the roughness corresponded to only the 2.8% of the minimum contact depth used to evaluate the hardness and the reduced modulus in this study.

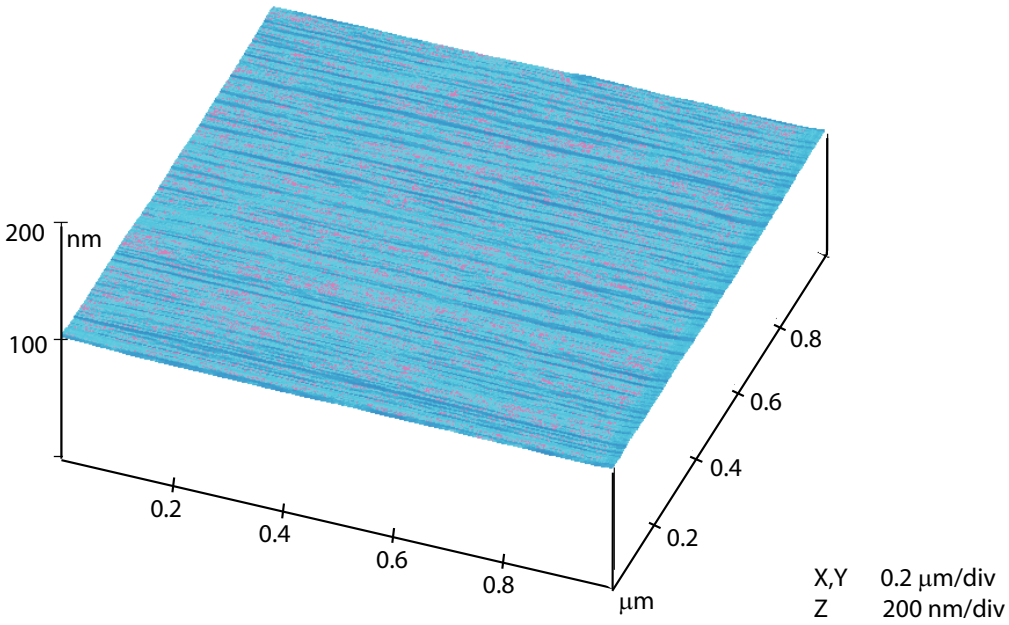

Figure 4.1: AFM image of a cleaved surface of AP.

4.1.2 Cleavage Steps

Examination of the {001} and {210} planes of AP under the optical microscope reveals many steps of different heights as can be seen in Fig. 4.2. The arrangement of the steps on the complementary areas of the matched cleaved faces (i.e., (001) and $(00\bar{1})$, (210) and $(\bar{2}\bar{1}0)$, $(\bar{2}10)$ and $(2\bar{1}0)$ planes) appears to form mirror images of each other. No correlation was observed between the cleavage steps and crystallographic directions.

Figure 4.3 shows AFM images of the {001} and {210} planes. The height of the small steps on the {001} planes correlated to the dimension of the crystal lattice perpendicular to the {001} planes $c = 7.449$ Å [42], and ranged from approximately $2c$ to $10c$, as shown in Fig. 4.4(a). However, larger steps were also observed, as can be seen in Fig. 4.4(b). These steps measured between $50c$ and $100c$. Similar features were observed for the {210} planes but corresponded to the dimension of the crystal lattice perpendicular to the plane $d = 3.608$ Å.

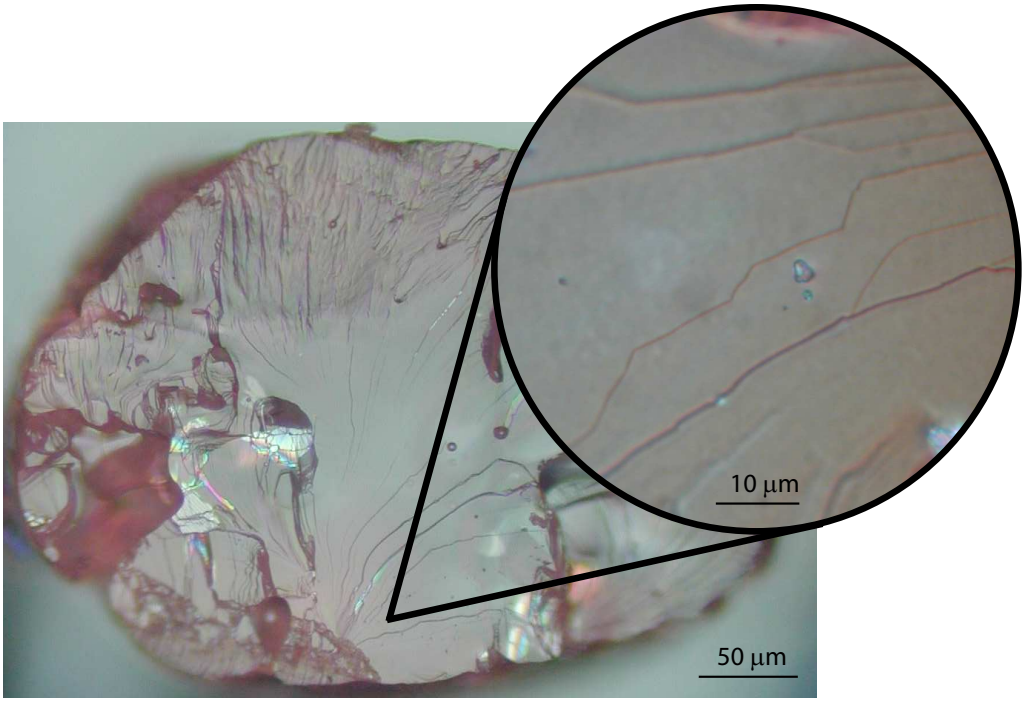

Figure 4.2: Typical AP cleaved surfaces obtained. Fine cleavage steps can be observed.

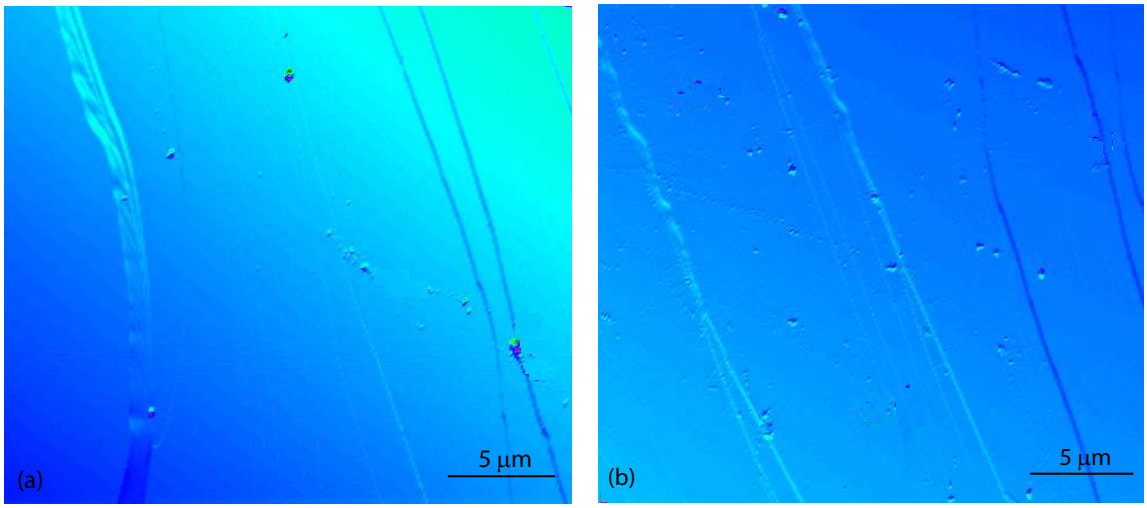

Figure 4.3: Examples of cleavage steps observed with AFM on: (a) {001} planes, and (b) {210} planes.

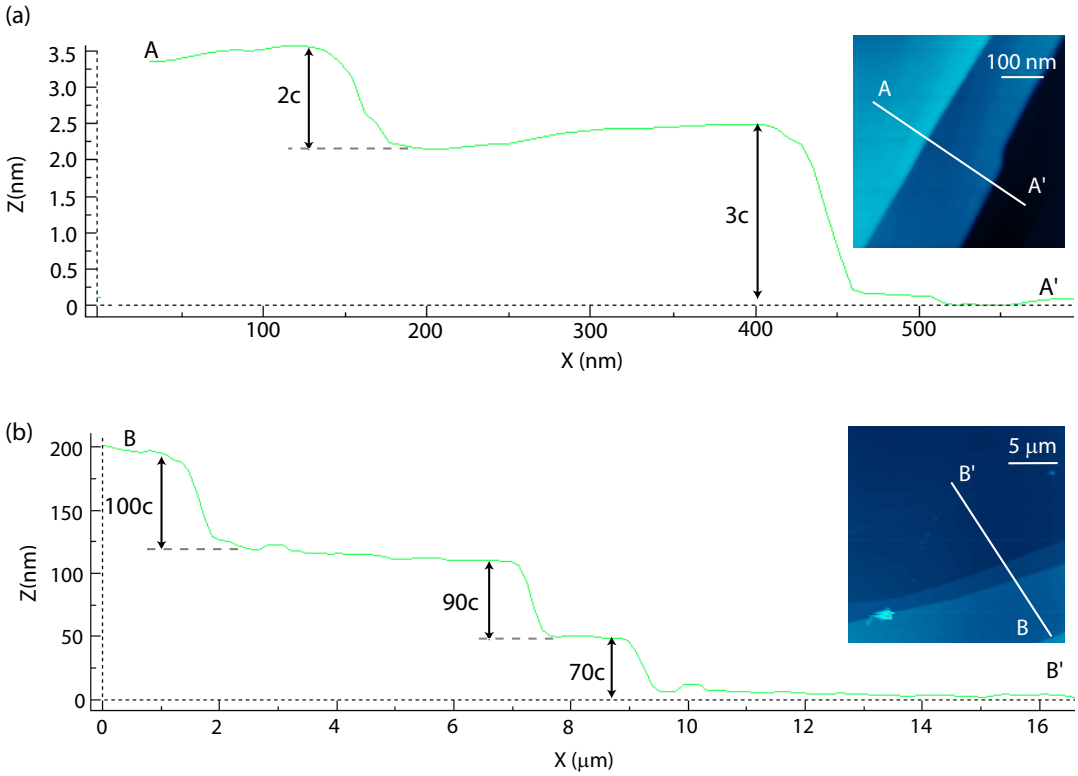

Figure 4.4: Cross-section of cleavage steps observed on the {001} planes with: (a) small steps approximately between $2c$ and $10c$, and (b) large steps between $50c$ and $100c$ ($c = 7.449$ Å [42]).

4.2 Optical and AFM Examination of Etched Surfaces

Chemical etching was performed to identify crystallographic planes and directions on the AP samples and to study the internal structure of the etch pits by AFM. Different etchants were tested on AP crystals based on previously reported etchants in the literature [13,14,28,51,52,127]. The best results were obtained by etching with 100% n-butanol. Well formed pits, all oriented in one direction were observed on the {001} and {210} cleaved planes. The pits started to form after 2 sec exposure to the etchant.

4.2.1 {001} Planes

An etch pit formed on a {001} plane is shown in the AFM amplitude mode image of Fig. 4.5(a). Amplitude mode measures the RMS signal of the cantilever amplitude and is proportional to rate of change of slope of the surface and is very sensitive to small changes in the height (Appendix D). A three dimensional representation of the etch pit is shown in Fig. 4.5(b).

100% n-butanol produces a rhombus based pyramidal pit at dislocations that intersect the {001} planes. The long axis of the rhombus lies parallel to ⟨010⟩ direction and the short axis is parallel to ⟨100⟩ direction as shown by Herley et al. [14] and Williams et al. [13].

The size of the axes of well-developed pits are approximately 6.52(±1.33) × 4.94(±1.16) μm. To the best of our knowledge, these dimensions have not been reported before. The depth of well developed pits is a function of the etching time

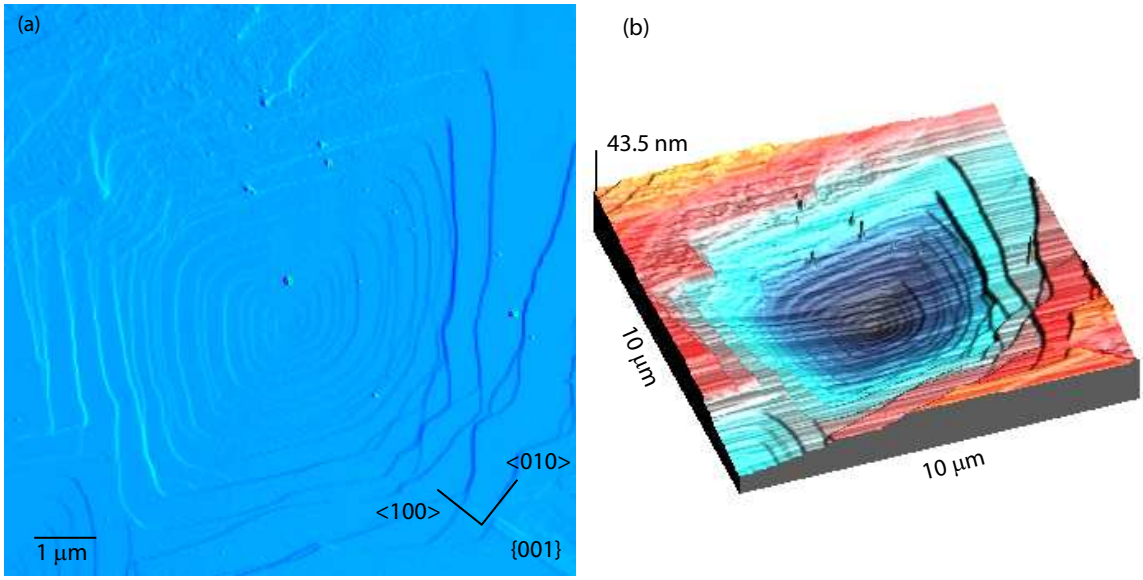

Figure 4.5: AFM images of etch pits on {001} planes of AP showing: (a) etch pit terraced structure, where the size of the pit is approximately 7 μm × 6 μm × 24 nm, and (b) a three dimensional view of the etch pit shown in (a).

and the nature of the dislocation that it reveals i.e., the dislocation can move away from its position and the pit will become flat-bottomed and will not continue to growth [54, 59]. Flat-bottomed pits were observed during sequential etching and it was noted that before any pit disappeared in such a series of etches it always became flat-bottomed as shown in Fig. 4.6(c). The faces forming the pits in Fig. 4.6 were examined and did not appear to be low index faces.

Some authors have related the angle that a dislocation line makes with the surface to the asymmetry of its etch pits [130, 131]. The pits observed on the {001} planes are symmetric and its axis is normal to the surface (Fig. 4.6), therefore, the line of the dislocation must lie normal to the cleaved plane. The inside of the pit has a spiral terraced structure with step heights between 0.7 and 5 nm, as shown in Fig. 4.6. It is interesting to observe that 0.7 nm corresponds approximately to the value of the dimension of the crystallographic unit cell perpendicular to this plane $c = 7.45$ Å [42].

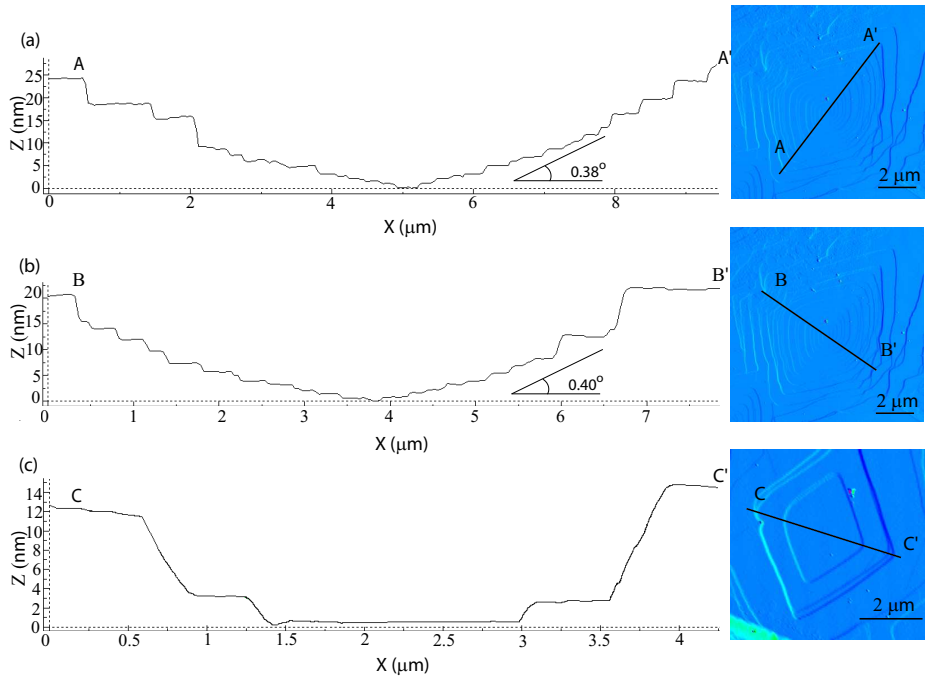

Figure 4.6: Terraced structure observed on profiles of pits on {001} planes: (a) along long axis, (b) along short axis, and (c) flat-bottomed pits.

This suggests that the etching could have proceeded by the removal of monolayers of the crystal, a reverse of the crystal growth process [54]. These spiral terraced pits, as can be seen in Fig. 4.7, are very similar to spiral growth patterns which have been seen on a large number of crystals and which result from screw dislocations formed during crystal growth. It is, therefore, most likely that these pits formed where spiral growth has occurred [53, 132, 133]. Most of the terraces were aligned parallel to the edges of the pit.

4.2.2 {210} Planes

Etching the {210} planes with 100% n-butanol produced rectangular etch pits, shown in Fig. 4.8(a). The longer side of the rectangular pit is parallel to the ⟨001⟩ direction and the shorter side parallel to the ⟨120⟩ direction as shown by Herley et al. [14] and Williams et al. [13]. The size of the etch pits observed are approximately $2.29(\pm 0.39) \times 6.85(\pm 0.63)$ μm. A three dimensional representation of the etch pit is shown in Fig. 4.8(b).

Just as before, pits were observed to flatten, shown in Fig. 4.9(c), prior to their disappearance.

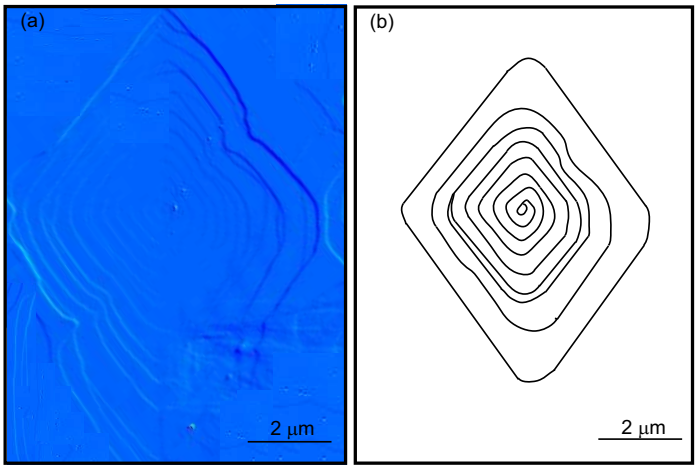

Figure 4.7: (a) AFM image of an etch pit on the {001} planes showing a clockwise spiral. (b) Line drawing of the pit shown in (a).

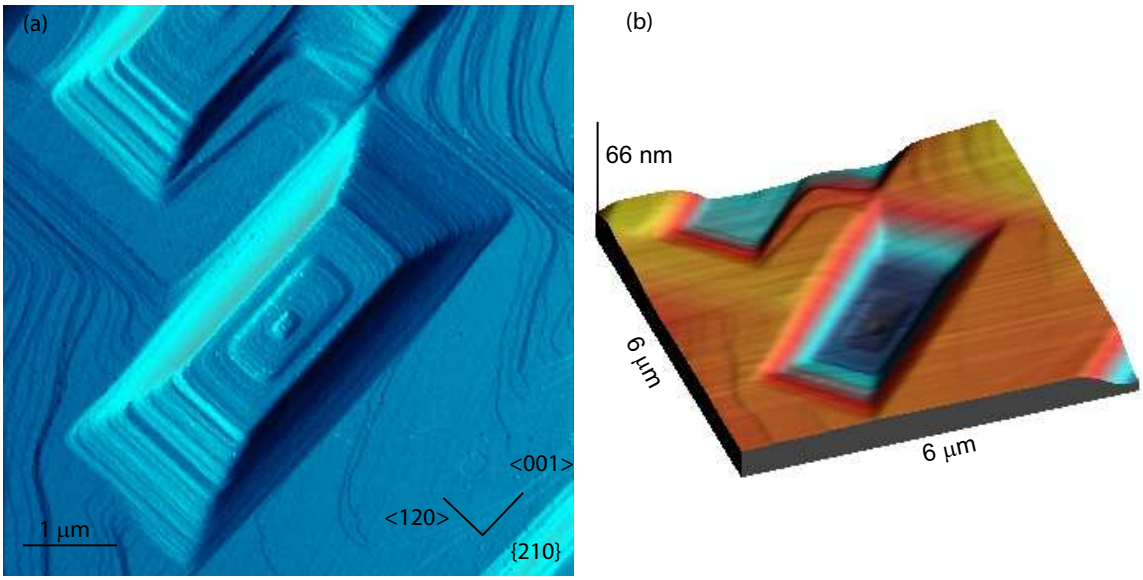

Figure 4.8: AFM images of etch pits on {210} planes of AP showing: (a) etch pit terraced structure, where the size of the pit is approximately 2 μm $\times$ 5 μm $\times$ 40 nm, and (b) a three dimensional view of the etch pit shown in (a).

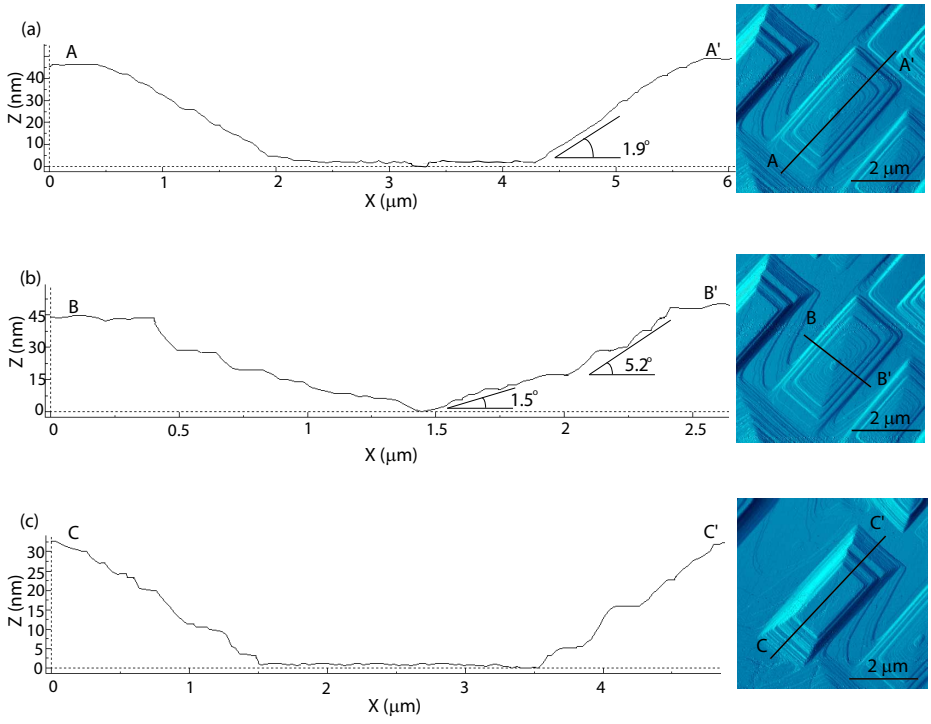

Figure 4.9: Terraced structure observed on profiles of pits on {210} planes: (a) along long side, (b) along short side, and (c) flat-bottomed pits.

Figure 4.9(a) and (b) show that the long side (A-A′) of the pits are steeper than the shorter sides (B-B′). Both sides of the pits do not appear to correspond to low index faces. The pits observed on the {210} planes are symmetric and its axis is normal to the surface, as can be seen in Fig. 4.9, therefore the line of the dislocation must lie normal to the cleavage plane as predicted by Johnston [59].

As in the case of the {001} planes, the inside of the pit has a spiral terraced structure as shown in Fig. 4.9 with step heights between 0.5 and 7 nm. Just as before these spiral terraced pits, Fig. 4.10, are very similar to the spiral growth patterns which have been seen on a large number of crystals [53,132,133]. Most of the terraces were aligned parallel to the edges of the pit. Interestingly Herley et al. [14] and Williams et al. [13], utilizing an electron microscope to observe carbon replicas of the surface of etched AP, did not report any evidence of spirals in the pits. This can be attributed to insufficient resolution due to the replication process or due to degradation of the surface itself.

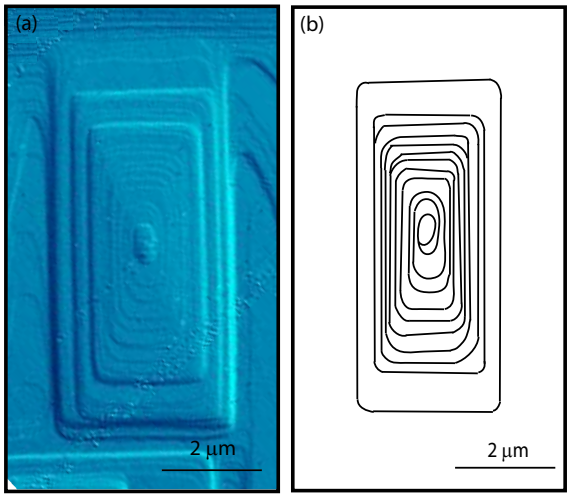

Figure 4.10: (a) AFM image of an etch pit on the {210} planes showing a counter-clockwise spiral. (b) Line drawing of the crystal shown in (a).

4.2.3 Etch Pit Density

Etch pits, essentially, reveal emergence points of dislocations in the surface and, therefore, give a direct measure of dislocation densities [54]. The following evidence suggests strongly that all dislocations are revealed by the present etching techniques [130, 131]:

- Almost identical pattern of pits appear on matched cleavage faces.
- The dislocations that are attacked by the etchant are attacked uniformly.
- When a dislocation moves away from the position of a pit, during subsequent etching the pit ceases to have a pyramidal shape; it becomes flat-bottomed. Thus, a dislocation not only originates a pit, but its presence is necessary to maintain the pyramidal shape of a growing pit. Some authors have related the angle that a dislocation line makes with the surface to the asymmetry of its etch pits [130, 131].
- The etch pit density increases near inclusions or highly deformed regions.

A detailed AFM analysis was performed for seven different samples by scanning each sample in five locations with a scan area of 30 μm x 30 μm. Based on these 35 images, the etch pit density was found to be approximately $(2.6 \pm 0.33)\times10^6$ cm^{-2} for the {001} planes and $(3.6 \pm 0.35)\times10^6$ cm^{-2} for the {210} planes. Table 4.1 presents a comparison between the measured values of etch pit density and values found in literature. The etch pit density measurements exhibit a normal distribution and are comparable with the previous values obtained in other studies [13, 14]. The etch pit density obtained for {210} is slightly higher than the one obtained for the {001} planes.

Cleavage Plane	Etch Pit Density ($\times 10^6$ cm^{-2})			
	Measured	**Williams** [13]	**Thomas** [127]	**Herley** [14]
{001}	(2.6 ± 0.33)	0.1 - 5	0.1	3.0
{210}	(3.6 ± 0.35)	0.1 - 5	3.0	0.1

Table 4.1: Measured etch pit density from AFM images with a comparison to values found in literature.

4.3 Nanoindentation Studies on Cleaved Surfaces of AP

The mechanical response of crystalline energetic solids to force loading is known to play a role in thermal decomposition, and also contributes to the overall mechanical behavior of the solid propellant. Whereas, submicrometer scale investigations of energetic crystals have been reported [15, 44, 134], to our knowledge characterization by nanoindentation has not been addressed.

In this study, both the {001} and {210} cleavage planes of AP were investigated by nanoindentation. The load range of indentations performed on both planes was from 60 - 500 μN, corresponding to a contact depth of 30 - 175 nm. The smallest indentation was chosen with a peak load higher than the P_{crit} to initiate plastic deformation so that hardness could be measured.

4.3.1 Load-Displacement Analysis

Figure 4.11 illustrates a typical load vs. penetration depth nanoindentation curve obtained for {001} planes of AP. The curve shows: (a) an elastic loading region, (b1-b5) multiple sudden increases in penetration depth at a given load, (c) elasto-plastic loading, (d) creep at maximum load, and (e) an unloading region. The point

at which the unloading curve (e) intersects the penetration depth axis (f) is the permanent depth of indentation. the same behavior was observed for indentations on the {210} planes. The abrupt increase in penetration at a given load is referred to as "pop-in" and has been observed in a large variety of materials including metals [91–93] and semiconductors [94, 95].

It should be noted, from Fig. 4.11, that a small load decrease was observed during the holding period. This is an artifact of our instrument. In the transducer the indenter tip is suspended on springs and with the applied electrostatic force being held constant, a large displacement increment would result in a sizable increase in the spring force, causing the load applied onto the sample to drop. This effect has

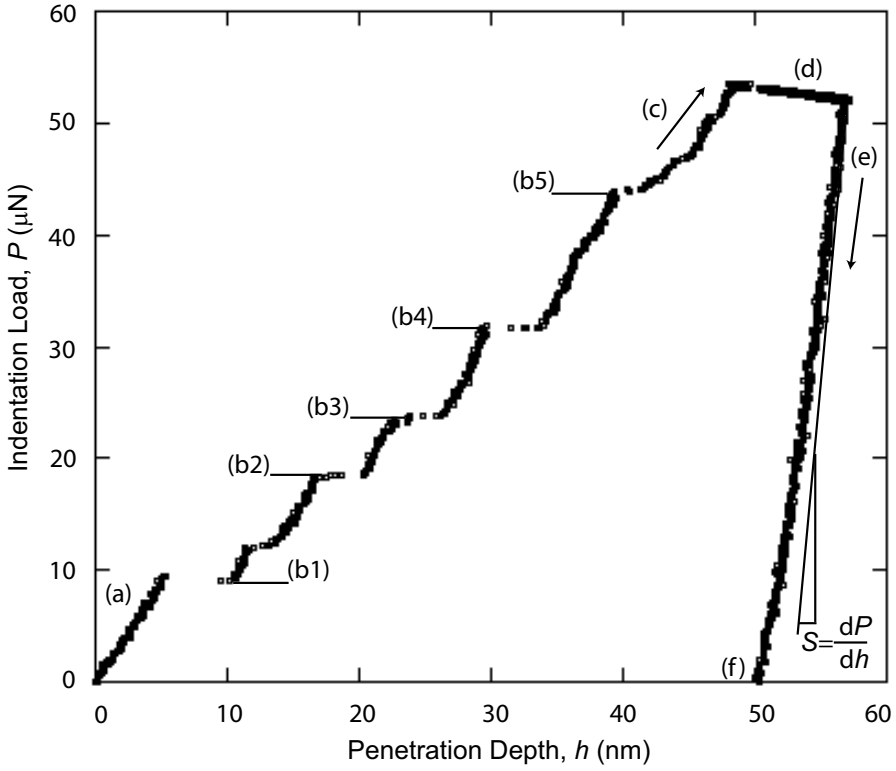

Figure 4.11: Typical load vs. penetration depth curve for {001} planes of AP using a Berkovich indenter. Multiple pop-in events (b1 - b5) were observed for all indentations. Same behavior was observed for indentations on the {210} planes.

also been observed in In, Al and Sn [113].

From Fig. 4.11, the first pop-in is observed to occur at about 10 μN. Shortly after the first pop-in, the load vs. penetration depth curve becomes serrated, indicating a series of smaller pop-ins following the main one. Multiple pop-in events have been observed in other indentation studies such as sapphire, GaN and ZnO and have been attributed to activation and generation of dislocations on different slip systems [95, 99–101]. It has been proposed that the first pop-in corresponds to a dislocation nucleation event. These nucleated dislocations will move in the directions of easy slip until they get pinned as result of interactions between slip systems, further plastic deformation will require the generation of more dislocations, resulting in multiple pop-in events [100,101]. This provides a plausible explanation for the multiple pop-in events observed in the present study of AP, however, further investigation is needed.

Pop-in was observed in all the experiments performed. The critical loads for first pop-in for the {001} and {210} planes were 12.9 ± 3.4 μN at a penetration depth of 6.4 ± 1.8 nm, and 14.7 ± 5.2 μN at a penetration depth of 8.9 ± 3.4 nm respectively. The standard deviation was obtained from fifty experiments performed at a maximum load of 60 and 40 μN. Figure 4.12 shows the load vs. penetration depth curves for both cleavage planes and Table 4.2 summarizes the results obtained for the critical load and depth.

The nature of the pop-in observed can be examined by considering the initial portion of the loading curve, Fig. 4.11(a). For indentations performed with a maximum load below the critical load at pop-in, the strain produced was found to be totally

Plane	P_{crit} **(μN)**	h_{crit} **(nm)**
{001}	12.9 ± 3.4	6.4 ± 1.8
{210}	14.7 ± 5.2	8.9 ± 3.4

Table 4.2: Pop-in results for the two cleavage planes of AP.

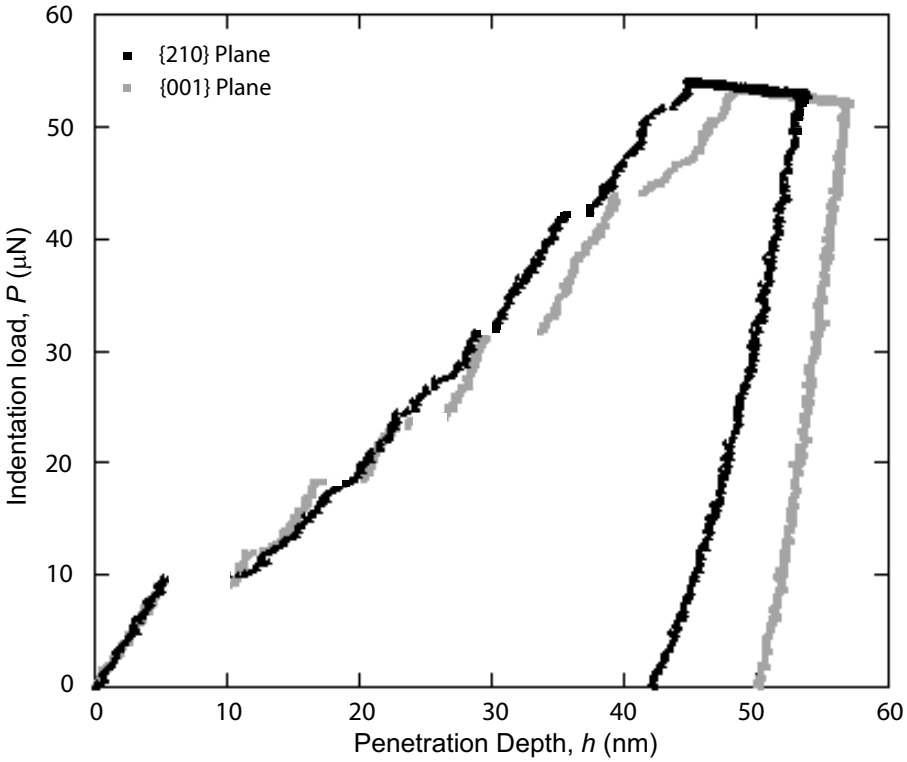

Figure 4.12: Comparison between load vs. penetration depth curves obtained for the {001} and {210} planes.

recoverable. This was confirmed by the fact that the loading curve is re-traced during unloading returning to zero indentation depth as can be observed in Fig. 4.13, and also by observation of the surface topography immediately after indentation with the AFM which showed no residual impression. This purely elastic behavior suggests that the release of strain energy at pop-in corresponds to a dislocation nucleation event and the initial yield point [91].

This initial loading can be modeled considering the Hertzian solution for a non-rigid spherical indenter in contact with an elastic half-space, where the load is related to the displacement by [107]:

$$P = \frac{4}{3} E_r \sqrt{R h^3} \tag{4.1}$$

where P is the load, R is the radius of the indenter tip, and h is the depth of penetration. In Fig. 4.14 the elastic contact solution given by Eq.(4.1) is compared

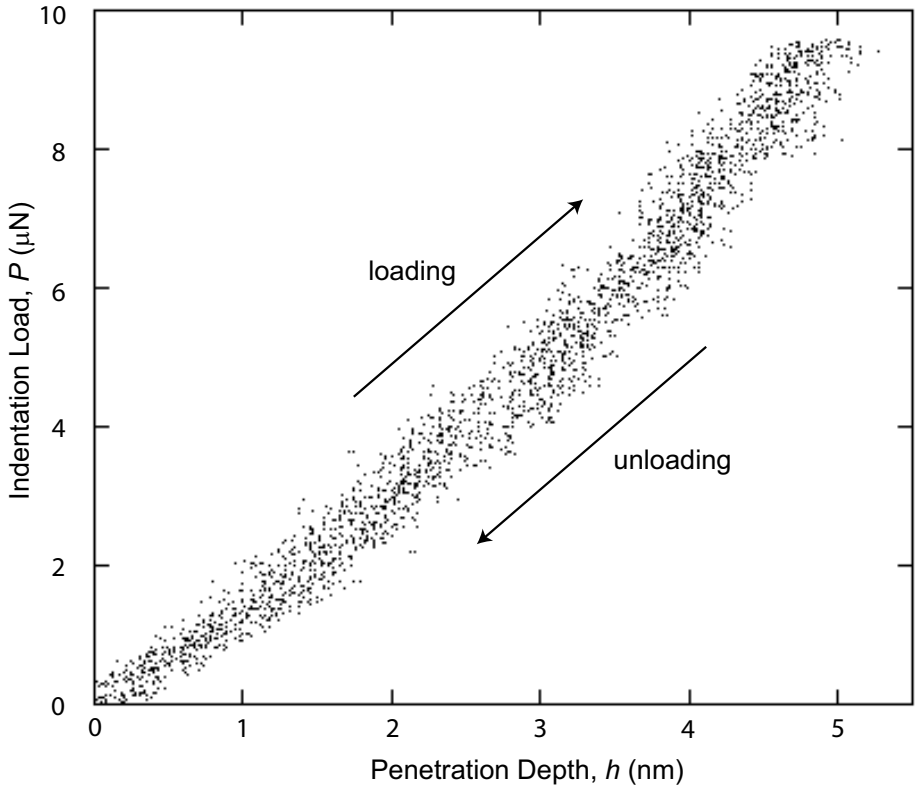

Figure 4.13: Elastic loading of a {001} plane. There is no evidence of residual plastic deformation. The loading and unloading curves overlap.

with the initial elastic portion of a load vs. penetration depth curve, using $R = 305$ nm and $E_r = 22$ GPa (obtained from Eq.(4.5) and Refs. [9, 38]). R was estimated by matching the area function of the Berkovich indenter (for $h_c \leq 10$ nm) with the area function of an ideal sphere. The two curves shown Fig. 4.14 follow the same path, confirming the purely elastic behavior before pop-in. The difference in both plots can be attributed to an offset in the force transducer or an error in the assumed radius of the tip, because better curve fitting was observed for higher radius values.

Figure 4.15 shows the load vs. penetration depth curves for two consecutive, neighboring indentations. The presence of the first indentation was found to suppress the occurrence of pop-in in the second indentation. This behavior was observed on both cleavage planes. The initial indentation which was made with a maximum load of 50 μN was seen to exhibit multiple pop-ins. When a second indentation was made

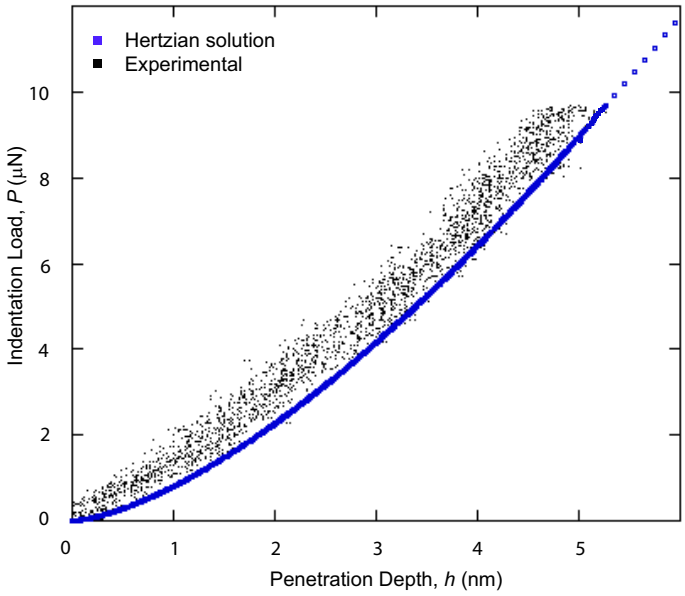

Figure 4.14: Initial elastic portion of a load versus penetration depth curve in {001} AP is compared with elastic contact theory.

in the neighborhood, but did not overlap the first, pop-in was not observed. This suggests that the presence of dislocations sources produced by the first indentation provided nucleation sites for dislocation motion during the second indentation, therefore pop-in was not observed. This result is consistent with the results of Miyahara et al. [135]. Who, also, observed that a neighboring indentation suppressed the occurrence of pop-in during the nanoindentation of single crystal tungsten.

To further support the idea of the dislocation nucleation at pop-in the maximum shear stress at the onset of pop-in was calculated and compared with the theoretical shear strength. Considering elastic contact model (Hertzian solution) between a spherical tip and a flat surface of an isotropic elastic half space, the maximum shear stress (τ_{max}) can be estimated using Eq.(4.2) [107]:

$$\tau_{max} = 0.31 P_m = 0.31 \left(\frac{6E_r^2}{\pi^3 R^2} \right)^{\frac{1}{3}} P^{\frac{1}{3}} \tag{4.2}$$

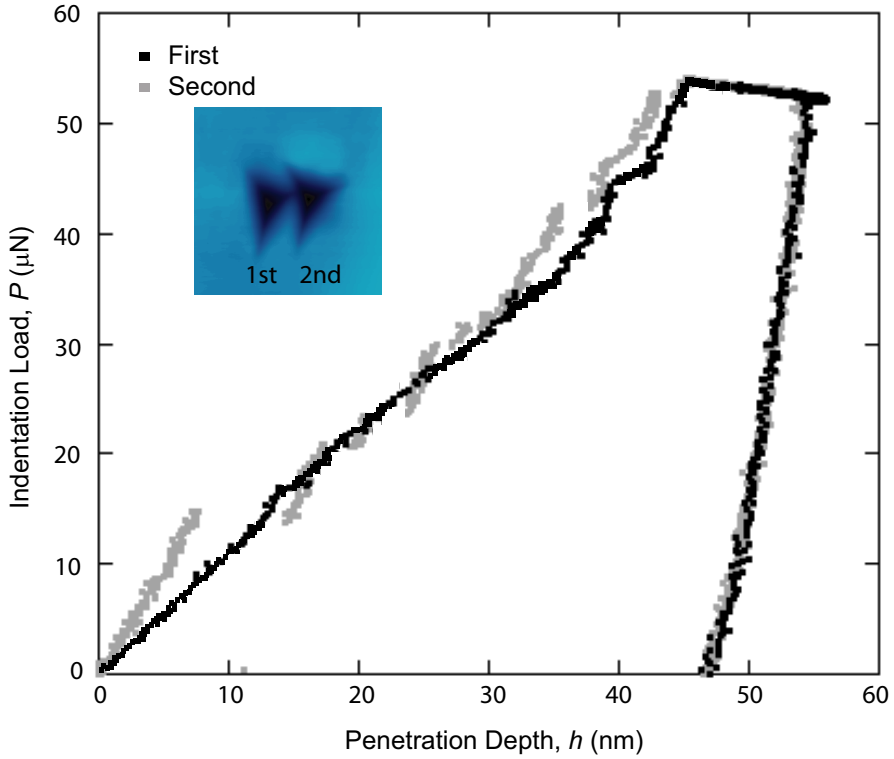

Figure 4.15: Load versus penetration depth curves for two neighboring but not overlapping indentations in {001} AP. The first indentation has multiple pop-in events however the second does not.

For the {001} planes with $P = P_{crit} = 12.88$ μN and $R = 305$ nm and $E_r = 22$ GPa (obtained from Eq.(4.5) and Refs. [9,38]), τ_{max} is estimated to be about 0.7 GPa. For the {210} planes 0.72 GPa was calculated using $P = P_{crit} = 14.7$ μN. The theoretical shear strength for a perfect lattice was calculated applying the formula for an ionic crystal [60]: $\tau_{theo} \approx G/8$. For $G = 7.4$ GPa [9], $\tau_{theo} \approx 0.9$ GPa was calculated. The difference obtained between τ_{theo} and τ_{max} obtained for both planes can be accounted for the anisotropic behavior of AP and by the presence of non-neglectable electrostatic effects into the ionic crystal cell. This coarse approximation for τ_{max} however differs from the theoretical value τ_{theo} by approximately 23%.

The displacement in the first pop-in was observed to be a function of the instantaneous depth of the indenter. Larger incursions were observed for higher loads. This

can be explained by the fact that more elastic energy is stored in the material when a higher load is reached before the first pop-in.

4.3.2 Indentation Hardness

Results of hardness as a function of contact depth are shown in Fig. 4.16, where the error bars along the hardness scale are based on one standard deviation of about fifty experiments per point.

The two planes exhibit similar hardness values, although the values obtained for the {210} planes are slightly higher. A decrease in hardness for both planes at greater depths can be inferred (ISE, Sec. 2.6.4) and may have a physical basis as described by the strain gradient plasticity [115] The average hardness values at a contact depth of 35 nm for the {001} were found to be 0.51 GPa and the hardness decreased to 0.27 GPa at a contact depth of 150 nm. For the {210} the average hardness value reduces from 0.72 GPa at 31 nm to 0.39 GPa at 121 nm. The larger error bars on the shallowest indentations are likely caused by the surface roughness or the effects of the environment on the near surface. No variation in hardness was observed, even after 10 hours of exposure to the low humidity environment (12%), inside the AFM enclosure. The decrease of hardness with indentation depth has been observed in AP for micro-indentation tests and was attributed to the presence of cracks [7, 8]. Cracking of the AP was not observed around indentations used to evaluate the hardness. These values of hardness are consistent with the only values found for AP, obtained by Elban and Armstrong [8] utilizing Vickers micro-indentation and for much deeper indentations, approximately 17 μm found a VHN of 13 corresponding to a Vickers hardness of 0.127 GPa and a VHN of 11 (0.108 GPa) for the {210} and {001} planes respectively. The hardness results are summarized in Table 4.3.

A possible explanation for the difference in hardness for the two planes obtained with nanoindentation experiments is that different slip systems were involved during

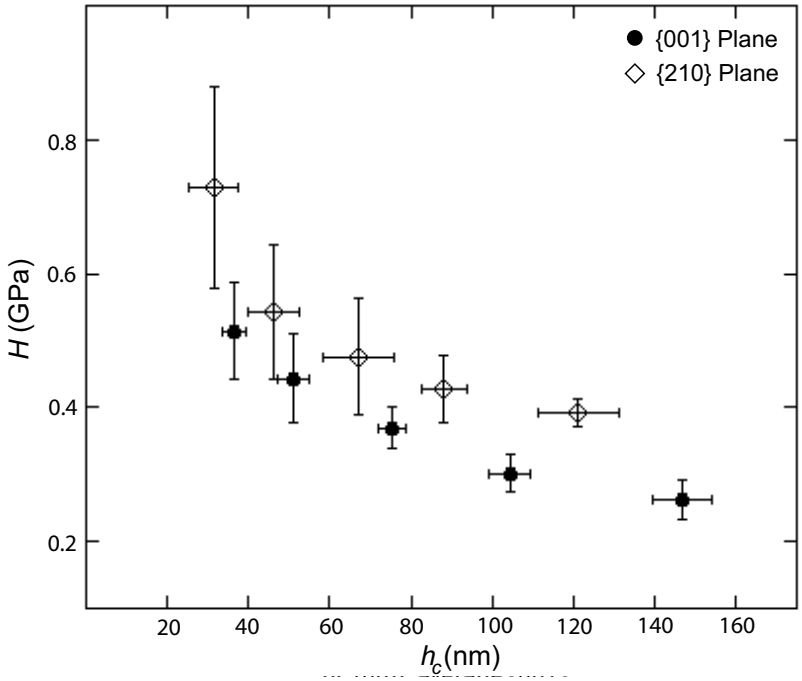

Figure 4.16: Hardness versus contact depth for both cleavage planes of AP.

plastic deformation which is further discussed in section 4.4.

4.3.3 Measured Reduced Modulus

Figure 4.17 shows the reduced modulus as a function of contact depth obtained for both cleavage planes. The error bars along the elastic modulus are based on the stan-

	Nanoindentation		**Micro-indentation** [8]	
Plane	H **(GPa)**	**Depth (nm)**	H **(GPa)**	**Depth (μm)**
{001}	0.51 ± 0.07	36.6 ± 2.9	0.108	19
	0.27 ± 0.03	146.8 ± 5.4		
{210}	0.72 ± 0.15	31.4 ± 5.6	0.127	17
	0.39 ± 0.02	121.2 ± 7.9		

Table 4.3: Hardness results obtained of the two cleavage planes of AP and comparison with previous micro-hardness study [8].

dard deviation of about fifty experiments per point. The reduced modulus approaches a constant value for greater depths in both planes. For the shallowest indentations, the reduced modulus increases and larger error bars are observed. It is likely that the reduced modulus increases because the number of defects decreases near to the surface and the material behaves in an ideal manner. It is also likely that the surface roughness or effects of the environment influence on the near-surface properties.

The average value of reduced modulus was observed to be 22.2 ± 1.0 GPa for the {001} planes and 19.9 ± 1.1 GPa for the {210} planes. The fact that the reduced modulus measured for the {001} planes is higher than for the {210} planes over the entire range of contact depth investigated is consistent with the anisotropic behavior predicted from the elastic modulus, calculated using the elastic constants of AP where $E_{[001]} = 25.1$ GPa and $E_{[210]} = 21.3$ GPa (Section 2.3.1).

No value of Poisson's ratio was found for AP in the literature but the actual value of Poisson's ratio is not critical to influence the trend. Poisson's ratio can be obtained using the reported values of bulk modulus $K = 15.2$ GPa [38], shear stress $G = 7.4$ GPa [9] and assuming an isotropic behavior by [60]:

$$\nu = \frac{1 - 2G/3K}{2 + 2G/3K} \tag{4.3}$$

a value of $\nu = 0.29$ is obtained. The elastic modulus can be calculated using:

$$\frac{1}{E_r} = \frac{(1 - \nu^2)}{E} + \frac{(1 - \nu_i^2)}{E_i} \tag{4.4}$$

using $E_i = 1141$ GPa and $\nu_i = 0.07$ for diamond, $E = 20.6$ GPa for the {001} planes and $E = 18.4$ GPa for the {210} planes were obtained [66].

The value of elastic modulus is consistent with the low end values obtained by Raevskii et al. [28], between 19.6 - 39.2 GPa, measured from tensile test of crystal whiskers of AP. Furthermore if the reported value of bulk modulus K [38] and shear stress G [9] is used to obtain the elastic modulus assuming an isotropic behavior using

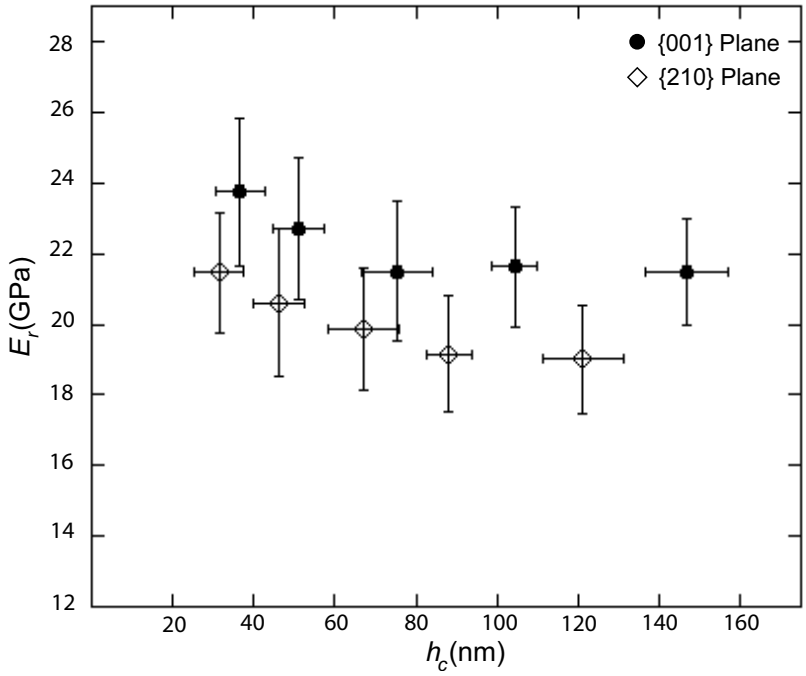

Figure 4.17: Reduced modulus versus contact depth for both cleavage planes of AP.

the equation [60]:

$$E = \frac{9KG}{3K + G} \tag{4.5}$$

a value of $E = 19.1$ GPa was obtained which is in between the two values obtained for the cleaved planes.

The reduced modulus results are summarized in Table 4.4. The difference in reduced modulus obtained between {210} and {001} planes could be attributed to the difference in the atomic arrangement of the two surfaces as a result of reconstruction and relaxation (Appendix B). Indentation after 10 hours exposure to the low humidity (12%) environment inside the AFM enclosure did not present any appreciable variation in reduced modulus.

Plane	E_r **(GPa)**	**Depth (nm)**
{001}	23.7 ± 2.0	36.6 ± 2.9
	21.5 ± 1.5	146.8 ± 5.4
{210}	21.4 ± 1.7	31.4 ± 5.6
	19.0 ± 1.5	121.2 ± 7.9

Table 4.4: Reduced modulus results of the two cleavage planes of AP.

4.4 Principal Slip Systems

Atomic force microscopy was used to study the surface topography, and identify probable slip systems responsible for slip trace formation around indentations. A spherical indenter was used for most of these studies to avoid the stress concentration caused by the edges of the Berkovich indenter.

During indentation, slip traces are the result of dislocations emerging at the free surface and steps appear in a line direction, which corresponds to the intersection of a slip plane and the plane of indentation [136]. Measuring the angle between each slip trace and the reference direction provided by etching, allows each slip trace to be assigned to a specific crystallographic direction. The slip system information provided by Williams et al. [13] and Herley et al. [14] has been utilized in determining the probable slip systems chosen to explain the slip traces. Williams et al. [13] and Herley et al. [14] deduced the most likely slip systems from the crystal structure and electrostatic interactions.

It was observed that the slip traces form a pattern on the surface surrounding the impression, which varies with the crystallographic plane in which the indentation was made. For indentations with the Berkovich and cube corner indenter on a given plane, rotations of the sample around an axis perpendicular to the plane did not significantly affect the overall pattern in any of the crystals tested. Some details of

the slip trace patterns are expected to change with different tip shapes, however, since the slip traces are caused by the available slip systems, the basic pattern will not be affected significantly.

4.4.1 $\{001\}$ Planes

AFM imaging of residual impressions does not reveal pile-up for low-load indentations ($\leq$ 250 μN), used to identify the values of hardness and elastic modulus, however, at higher loads ($\geq$ 2 mN), significant pile-up was always observed. Fig. 4.18(a) shows the surface topography of a spherical indentation with a maximum load of 10 mN obtained by AFM. Pile-up for all high-load indentations on the $\{001\}$ planes was always aligned with the $\langle 010 \rangle$ direction, as determined by etching of the crystal after scanning with the AFM. For indentations with a maximum load of 10 mN, the pile-up had a maximum height of about 530 nm, approximately 20% of the indentation depth.

Figures 4.18(b) and (c) show the cross section of the pile-ups observed surrounding the indentation, with cracks which have a depth of approximately 49 nm. The crack has one side that is higher than the other which suggests that this crack may have started as a slip trace on the surface and, because of extensive plastic deformation, it appears as a crack. The cracks are aligned to the $\langle 010 \rangle$ direction, parallel to the cracks observed by Elban and Armstrong [8] with Vickers indentation, although, in some cases, microindentations exhibited a second cracking system aligned to $\langle 100 \rangle$ perpendicular to the first cracking system. It can be observed, in Fig. 4.18(b) and (c), that a depression is formed along the $\langle 010 \rangle$ direction with a height of approximately of 60 nm. This depression is parallel to the troughs observed in the microindentation experiments.

The pile-up of deformation observed surrounding the indentation on the $\{001\}$ planes is constrained not by the indenter geometry but the crystal orientation, as

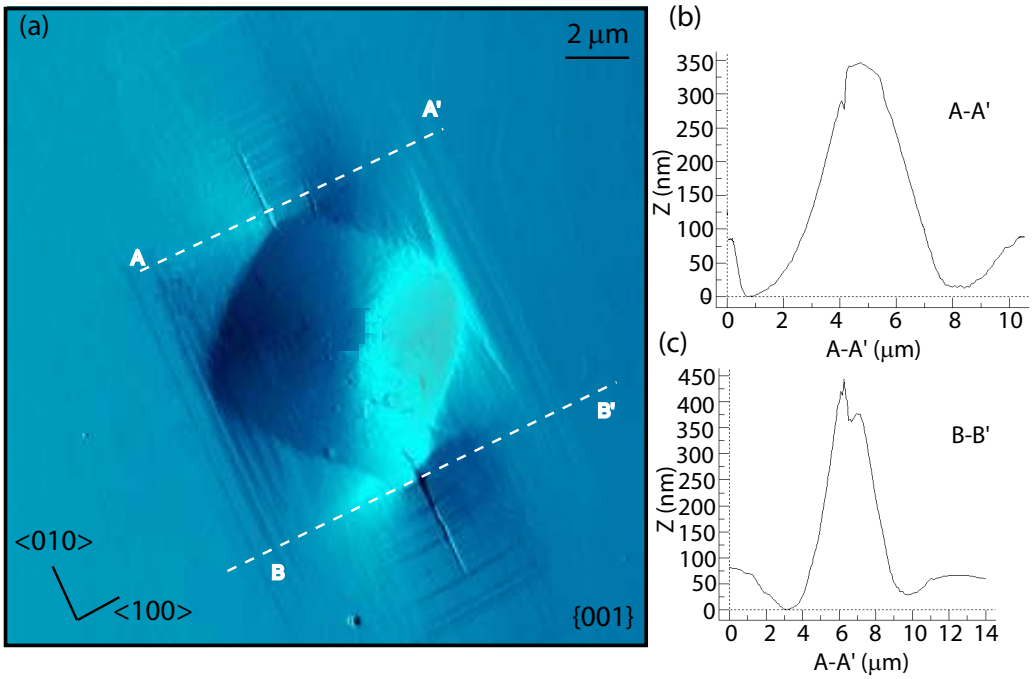

Figure 4.18: AFM image of a spherical indentation with a maximum load of 10 mN. (a) "Amplitude mode" image showing two-fold rotational symmetry of slip traces. (b) Shows the cross-section (A-A′) of the pile-up, crack and depression in this region. (c) Shows the cross section (B-B′) of the pile-up, crack and depression in this region.

can be seen in the Berkovich indentation on the {001} planes in Fig. 4.19, a similar pattern of plastic deformation aligned to the {010} direction and the same slip traces as in the spherical indentation are observed. this is similar what Zielinski et al. [137], Stelmashenko et al. [138] and Woodcock and Bahr [139] observed, who studied Fe-3%Si, tungsten and molybdenum single crystals.

Operative Slip Systems

The consequence of the indentation creating dislocation motion provides a possible explanation of the upward displacement of regions lying outside of the impressions [5]. The slip traces observed around a spherical indentation are shown in Fig. 4.20 and the probable slip systems for these slip traces are given in Table 4.5.

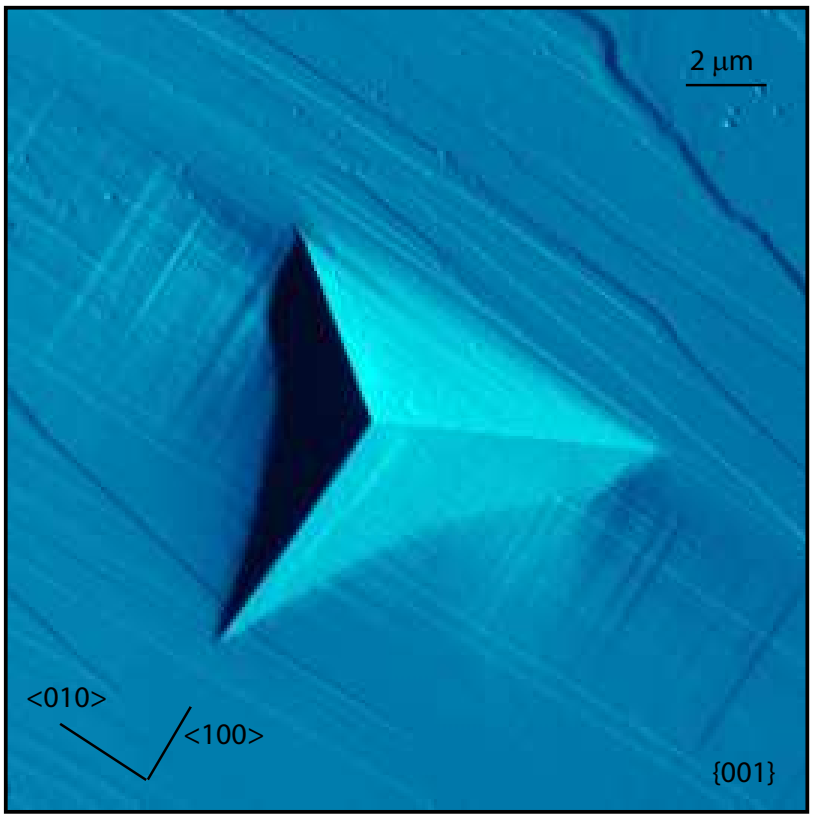

Figure 4.19: AFM image of a Berkovich indentation with a maximum load of 2.5 mN. The plastic deformation pattern observed is similar to that for a spherical indentation.

The slip traces aligned to the $\langle 010 \rangle$ direction can be related to dislocations moving along $\pm \langle 001 \rangle$ and can be attributed to slip on the (100) plane. This system also could be responsible for the depressions observed parallel to the $\langle 010 \rangle$ direction. The slip traces observed parallel to the $\langle 100 \rangle$ direction can be attributed to the $(010)\langle 001 \rangle$ slip system. These slip traces were more prominent at medium loads (1 mN to 2 mN). This system would also be responsible for the pile-up observed, because of the slip traces parallel to the $\langle 100 \rangle$ on the pile-up. It can be seen in Fig. 4.20 that the highest part of the pile-up existed on more closely spaced slip traces.

In compression tests on AP crystals, slip traces along [100], [110], [140], [180] and [010] directions were found and it was concluded that slip can occur in the [001] direction in almost any plane that contains the [001] axis [14]. It seems likely that the

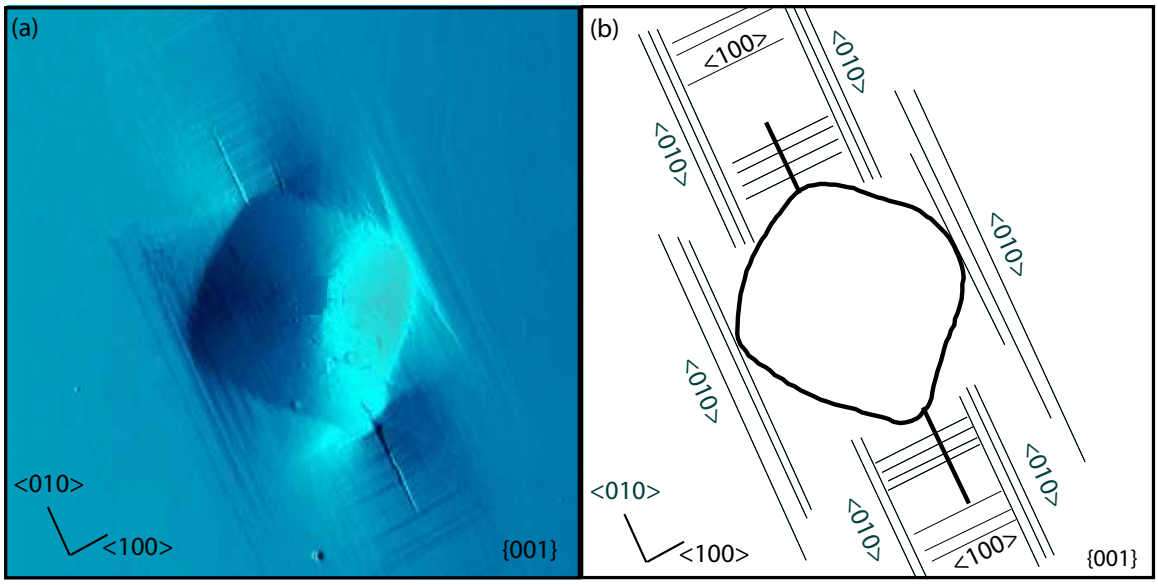

Figure 4.20: (a) Amplitude mode AFM image of a spherical indentation on {001} planes with a maximum load of 10 mN. (b) Schematic drawing of the slip trace pattern shown around the indentation (a).

first systems to be activated are the ones observed in nanoindentation, forming the slip traces ⟨010⟩ and ⟨100⟩. The slip traces obtained in the nanoindentation experiments were also observed during shock loading testing, although we did not observe cracks aligned to the $\langle\bar{1}10\rangle$ direction as was observed in the shock loading test [7]. In view of the plastic deformation obtained, the (100)⟨001⟩ and (010)⟨001⟩ are thought to be the primary deformation systems involved in forming the impressions on the {001} planes.

As proposed by Elban and Armstrong [8], the crack running along the ⟨010⟩

Slip Traces	**Probable Slip System**	**Reference**
⟨100⟩	±(010)[001]	[8, 13, 14]
⟨010⟩	±(100)[001]	[8, 14]

Table 4.5: Relationship between observed slip traces on the {001} planes and the probable slip systems.

direction could be attributed to reaction of dislocations on (101) plane according to the vector equation:

$$\left(\frac{1}{2}\right)[101]_{(\bar{1}01)} + \left(\frac{1}{2}\right)[10\bar{1}]_{(101)} = [100]_{(100)} \tag{4.6}$$

this reaction would give a dislocation crack nucleus having a orientation similar to that exhibited by the pattern observed.

4.4.2 $\{210\}$ Planes

Figure 4.21(a) shows the surface topography of a spherical indentation on the $\{210\}$ planes with a maximum load of 10 mN obtained by AFM. Extensive asymmetric pile-up and a crack around the indentation were found for all indentations with a maximum load above 2.5 mN. The pile-up was always aligned with the $\langle 001 \rangle$ direction, as determined by etching of the crystal after scanning with the AFM, and had a maximum height of about 400 nm for a maximum load of 10 mN, approximately 30% of the indentation depth. Figure 4.21(b) shows the cross section of the pile-up region, with a crack which has a depth of approximately 80 nm. The crack has one side that is higher than the other, as in the case of the $\{001\}$ planes, suggesting that the crack may have started as a slip trace on the surface and because of extensive plastic deformation it appears as a crack. Figure 4.21(c) shows the cross section of a step formed on the surface aligned with the $\langle 120 \rangle$ direction with a height of approximately 70 nm. The figure shows a single step although, in some cases, a pair of steps was observed.

Pile-up in the $\{210\}$ planes was observed at only one side of the indentation, as opposed to the $\{001\}$ planes which had pile-up on two sides of the indentation. In order to further explore this result, indentations were performed with a Berkovich indenter and a cube corner indenter as shown in Fig. 4.22. Both indenters produced pile-up aligned with the $\langle 001 \rangle$ direction. A further experiment was performed in

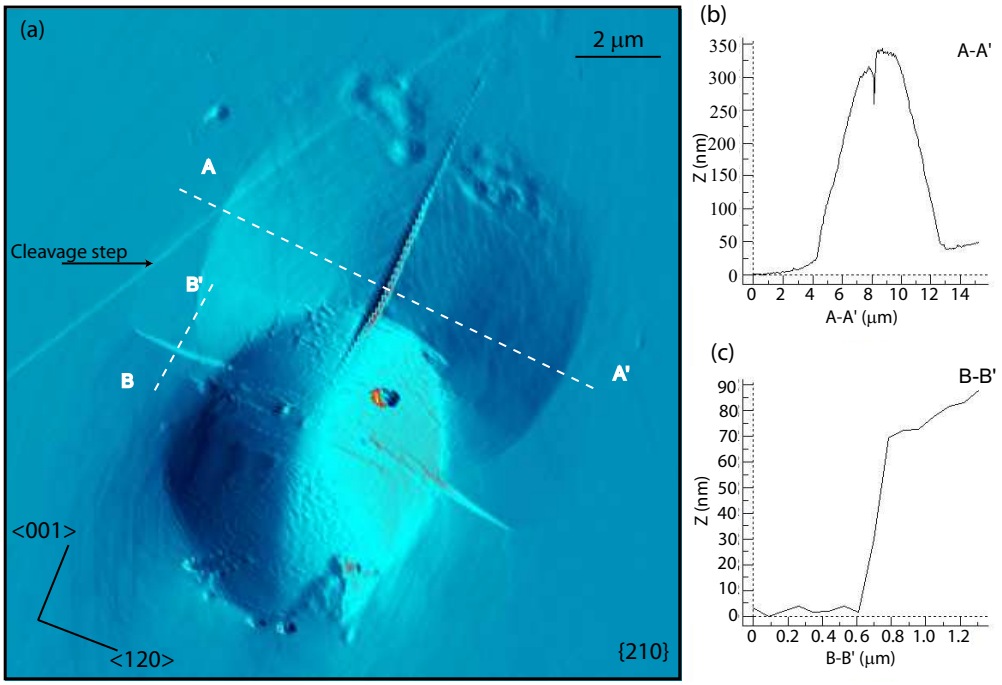

Figure 4.21: AFM image of a spherical indentation on the {210} planes with a maximum load of 10 mN. (a) Asymmetric pile-up above the indentation with a crack on top. (b) Shows the cross section (A-A′) of the pile-up and the crack in this region. (c) Shows the cross-section (B-B′) of the surface step that is in the ⟨120⟩ direction.

which the crystal was rotated after being indented, and the pile-up obtained was always asymmetric and aligned to the ⟨001⟩ direction.

It is interesting that on Vickers indentation experiments of the (210) plane of AP, Sandusky et al. [12] observed cracks in the ⟨001⟩ and $[\bar{1}\bar{2}0]$ direction, however, Elban and Armstrong [8] only report a crack in the $[\bar{1}\bar{2}0]$ direction. The difference with the crack that was observed in nanoindentation experiments could be explained that different slip systems can be activated at higher loads of indentation.

As in the case of the {001} planes, the pile-up of deformation observed are not constrained by indenter geometry, because the same pile-up was observed for the pyramidal and spherical indenters. Figure 4.22(a) shows an indentation using a Berkovich indenter on the {210} planes, with a maximum load of 10 mN. Asymmetric pile-up

is seen and a crack aligned to the ⟨001⟩ direction, as in the case of the spherical indentation, interestingly, the crack does not emanate from the corners of the indenter. The depth of the crack varied from 10 nm to 100 nm and is shown in the cross-section plot of Fig. 4.22(c). One side of the crack is higher than the other, similar to the spherical indentations.

Figure 4.22(b) shows an indentation using a cube corner indenter with a maximum load of 10 mN; a pile-up and a crack aligned to the ⟨001⟩ direction, as in the case of the spherical indentation, can be observed. Pile-ups are also observed aligned approximately to the ⟨121⟩ direction. These two pile-ups (approximately 100 - 250 nm) are

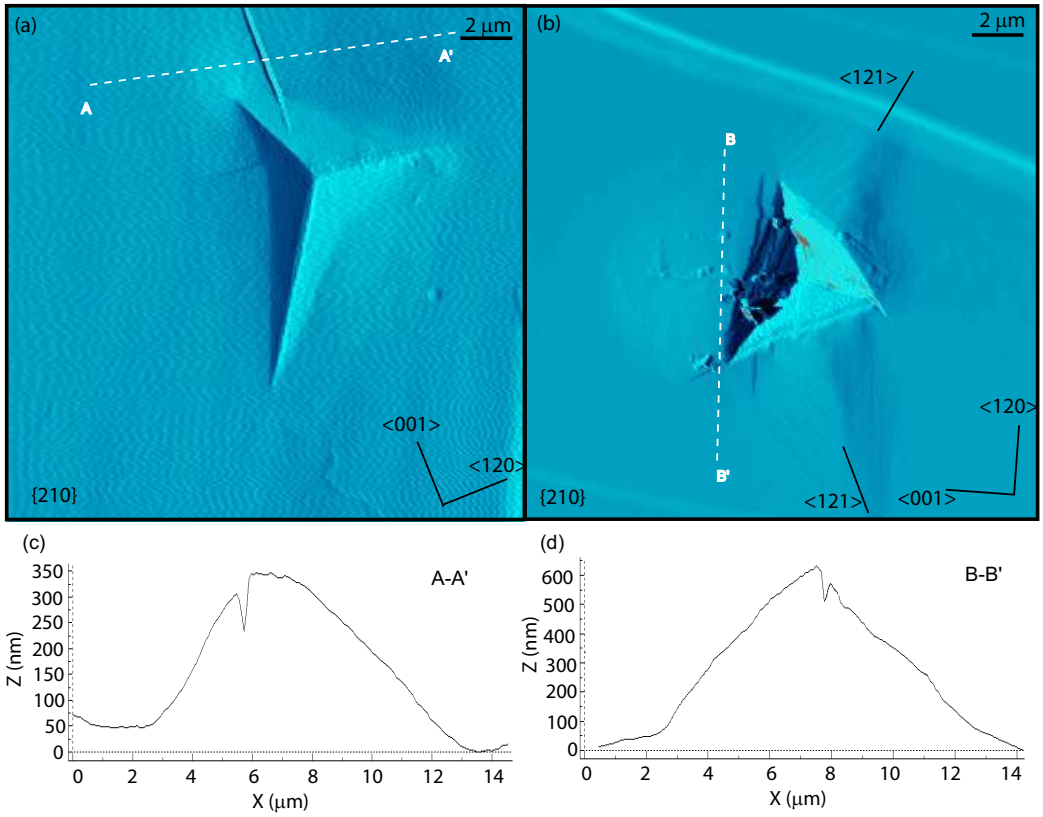

Figure 4.22: AFM image of indentations on the {210} planes with a maximum load of 10 mN. (a) Berkovich indentation impression. (b) Cube corner indentation impression. (c) Shows the cross-section (A-A′) of the pile-up and the crack on the Berkovich indentation. (d) Shows the cross-section (B-B′) of the larger pile-up and the crack on the cube corner indentation.

smaller than the pile-up aligned to the ⟨001⟩ direction (600 nm, Fig. 4.22(c)) and were never observed for indentations using either the spherical or the Berkovich indenter. Since the cube corner indenter generates higher stress concentration under the indenter it seems that it activated another slip systems which caused the formation of these pile-ups.

All the indentations were elongated in the ⟨001⟩ direction because different slip systems were operative in the total strain field. The plastic deformation around an indentation on the {210} planes is more asymmetric than the plastic deformation on the {001} planes.

Operative Slip Systems

Figure 4.23 shows the slip traces of slip planes intersecting the surface around an indentation, using a spherical indenter, on the {210} planes. As before, the slip system information obtained by Herley et al. [14] and Williams et al. [13] has been utilized in determining the deformation systems chosen to explain the current nanoindentation impressions.

The slip traces show the intersection of the slip plane with the sample surface and enable the determination of probable slip systems during indentation. Slip traces along ⟨001⟩, ⟨120⟩ and ⟨124⟩ directions have been observed on {210} planes as shown in Fig. 4.23 and the probable slip systems are presented in Table 4.6. The slip traces along the ⟨125⟩ directions have not been previously reported but were observed for all the spherical indentations on the {210} planes.

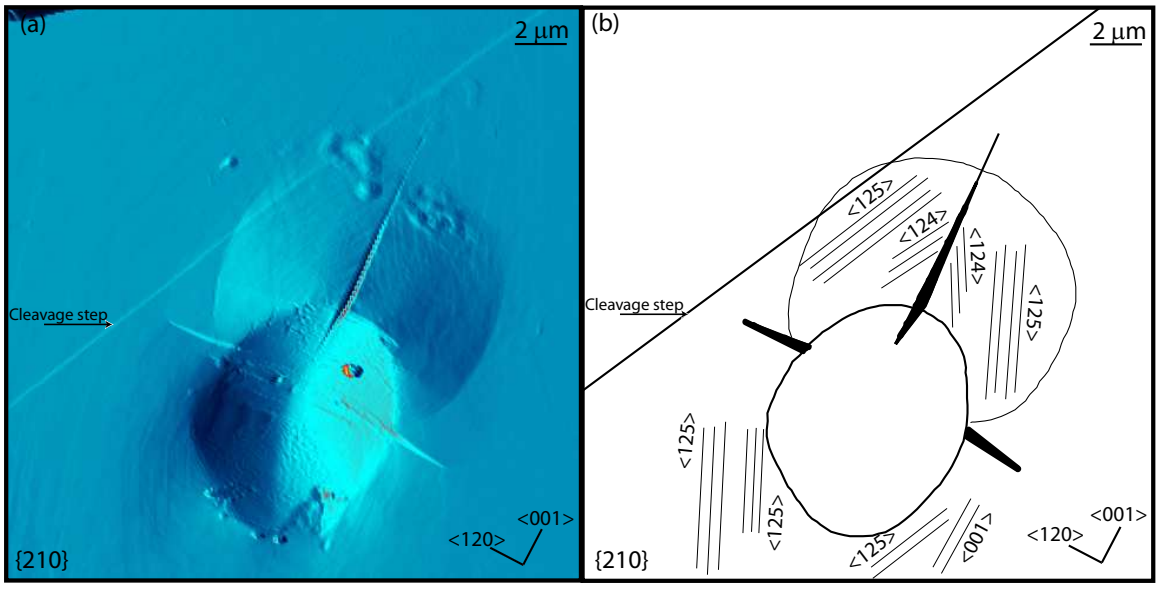

Figure 4.23: (a) Amplitude mode AFM image of a spherical indentation on {210} planes with a maximum load of 10 mN. (b) Schematic drawing of the slip trace pattern shown around the indentation (a).

Slip Traces	**Probable Slip System**	**Reference**
$\langle 120 \rangle$	$\pm(001)[010]$, $(001)[100]$	[13, 14]
$\langle 001 \rangle$	$(100)[010]$	[13, 14]
	$(\bar{1}00)[010]$, $(010)[\bar{1}00]$	[8]
$\langle 123 \rangle$	$(\bar{3}01)[010]$, $(301)[010]$	[13, 14]
$\langle 124 \rangle$	$(401)[010]$, $(40\bar{1})[010]$	[13, 14]

Table 4.6: Relationship between observed slip traces on the {210} planes and the probable slip systems.

Chapter 5

Conclusions

The near surface mechanical properties and mechanical behavior of the {001} and {210} planes of ammonium perchlorate have been investigated using nanoindentation in combination with AFM imaging. The crystal size was approximately 300 - 400 μm, which is about the size used for propellants.

- Chemical etching in n-butanol was used to determine the surface orientation of the crystals. The internal structure of etch pits on cleaved surfaces have been investigated using AFM. Pits observed on both surfaces presented a spiral terraced structure very similar to spiral growth patterns seen on a large number of crystals which result from screw dislocations formed during crystal growth.

- The pits observed on the {210} planes were rectangular with a size of approximately 2.29($\pm$0.39) $\times$ 6.85($\pm$0.63) μm.

- The pits observed on the {001} planes were rhombus-based pyramidal shape with a size of approximately 6.52($\pm$1.33) $\times$ 4.94($\pm$1.16) μm.

- The etch pit density obtained was (2.6 $\pm$ 0.33)$\times 10^6$ cm^{-2} for the {001} planes and (3.6 $\pm$ 0.35)$\times 10^6$ cm^{-2} for the {210} planes.

- Multiple pop-in events were observed in all of the indentations. Both cleaved

planes exhibited purely elastic behavior until the onset of plasticity at the first pop-in event.

- The critical load for the first pop-in on the {001} and {210} planes were 12.9 ± 3.4 μN at a depth of 6.4 ± 1.8 nm, and 14.7 ± 5.2 μN at a depth of 8.9 ± 3.4 nm respectively. Pop-in was attributed to dislocation nucleation and the onset of yielding.

- The hardness and reduced modulus were obtained over the depth range 30 nm to 150 nm. The measured hardness of the near surface was higher than that previously reported for deeper Vickers indentation [8].

- The hardness obtained for the {210} planes was slightly higher than the value obtained for the {001} planes consistent with previous micro-indentation studies [8]. The hardness was found to decrease as a function of the depth (ISE) for both planes. For the {001} planes the average hardness obtained at 35 nm was 0.51 GPa and the hardness decreased to 0.27 GPa at a contact depth of 150 nm. For the {210} the average hardness value reduces from 0.72 GPa at 31 nm to 0.39 GPa at 121 nm. The decrease of hardness with indentation was observed in AP for micro-indentation studies and was attributed to the presence of cracks [8]. No cracks were observed around the nanoindentations at these low loads ($\leq$ 250 μN).

- The reduced modulus was nearly constant over the depth range of 30 nm to 150 nm however a slight decrease was observed for the deepest indentations. The average value of the reduced modulus found for the {001} planes was 22.2 ± 0.99 GPa and 19.9 ± 1.1 GPa for the {210} planes. The fact that the reduced modulus measured for the {001} planes is higher than for the {210} planes is consistent with the anisotropic behavior predicted from the elastic modulus calculated using the elastic constants of AP. The difference in reduced

modulus could be attributed to the difference in the atomic arrangement of the two planes (Appendix B).

- Indenting with high loads (greater than 1 mN) on the {210} planes with either a Berkovich indenter, a spherical indenter or a cube corner indenter resulted in asymmetric pile-up, slip traces on the surface and cracks. Cracking was observed in the ⟨001⟩ direction and a step in the surface was observed in the ⟨120⟩ direction. All of the slip traces observed were consistent with reported values in the literature except one in the ⟨125⟩ direction which was observed for the spherical indentations.

- Indenting with high loads (greater than 1 mN) on the {001} planes with either Berkovich indenter or spherical indenter resulted in a more symmetric plastic deformation than the {210} planes with presence of pile-up, slip traces and cracks. Cracking was observed in the ⟨010⟩ direction and the pile-up aligned with this direction. All of the slip traces observed were consistent with reported values in the literature. Pile-up observed on both planes were strictly crystallographic and orientation dependent.

- In order to explain the slip traces observed around the nanoindentations the slip system information provided by Williams et al. [13] and Herley et al. [14] was used. Both researchers deduced the most likely slip systems based on the crystal structure and electrostatic interactions. The following slip systems were most likely active during nanoindentation: (010)[001], (100) [001], (001)[010], (001)[100], (100)[010], $(\bar{1}00)[010]$, $(010)[\bar{1}00]$, $(\bar{3}01)[010]$, (301) [010], (401)[010] and $(40\bar{1})[010]$.

- Differences in the mechanical properties of the {001} and {210} planes, observed in the present study, were attributed to the different slip planes activated during the indentation on different planes of the crystal. These results suggest that

more slip systems are involved in the deformation process during the indentation of the {210} planes as compared to the {001} planes.

Bibliography

[1] A.L. Ramaswamy, H. Shin, R. W. Armstrong, C. H. Lee, and J. Sharma. Nanosecond and picosecond laser induced cracking and ignition of single crystals of ammonium perchlorate. *Journal of Materials Science*, 31:6035–6042, 1996.

[2] F.P. Bowden and A.D. Yoffe. *Fast Reaction in Solids*. Academic Press Inc., New York, 1958.

[3] W.L. Elban, J.C. Hoffsommer, and R.W. Armstrong. X-ray orientation and hardness experiments on RDX explosive crystals. *Journal of Materials Science*, 19:552–566, 1984.

[4] R.W. Armstrong, C.S. Coffey, and W.L. Elban. Adiabatic heating at a dislocation pile up avalanche. *Acta Metallurgica*, 30:2111–2116, 1982.

[5] R.W. Armstrong and W.L. Elban. Dislocation aspects of plastic flow and cracking at indentations in magnesium oxide and cyclotrimethylenetrinitramine explosive crystals. In P.J. Blau and B.R. Lawn, editors, *ASTM STP 889: Microindentation Techniques in Materials Science and Engineering*, pages 109–128. ASTM, Philadelphia, 1984.

[6] J.J. Dick. Effect of crystal orientation on shock inititation sensitivity of pentaerythritol tetranitrate explosive. *Journal of Applied Physics*, 44(9):859–861, 1984.

[7] W.L. Elban, H.W. Sandusky, B.C. Beard, and B.C. Glancy. Microstructural basis for enhanced shock induced chemistry in single crystal ammonium perchlorate. *Journal of Propulsion and Power*, 11(1):24–31, 1995.

[8] W. L. Elban and R. W. Armstrong. Plastic anisotropy and cracking at hardness impressions in single crystal ammonium perchlorate. *Acta Materialia*, 46(17):6041–6052, 1998.

[9] R.W. Armstrong, H.L. Ammon, W.L. Elban, and D.H. Tsai. Investigation of hot spot characteristics in energetic crystals. *Thermochimica Acta*, 384:303–313, 2002.

[10] A.V. Raevskii, G.B. Manelis, E.M. Nadgornyi, and A.P. Ivanov. Filamentary crystals of ammonium perchlorate. *Doklady Akademii Nauk SSSR*, 209(1):157–159, 1973.

[11] R.W. Armstrong, W.L. Elban, A.L. Ramaswamy, and C. Cm. Wu. Thermomechanical aspects of energetic crystal combustion. In K.K. Kuo, editor, *Challenges in Propellants and Combustion: 100 years after Nobel.*, pages 313–336. Begell House, New York, 1997.

[12] H.W. Sandusky, B.C. Beard, B.C. Glancy, W.L. Elban, and R.W. Armstrong. Comparison of deformation and shock reactivity for single crystals of RDX and ammonium perchlorate. *Materials Research Society Symposium Proceedings*, 296:93–98, 1993.

[13] J.O. Williams, J.M. Thomas, Y.P. Savintsev, and V.V. Boldyrev. Dislocations in orthorhombic ammonium perchlorate. *Journal of Chemical Society (A)*, 3:1757–1760, 1971.

[14] P.J. Herley, P.W.M. Jacobs, and P.W. Levy. Dislocations in ammonium perchlorate. *Journal of Chemical Society (A)*, 3:434–440, 1971.

[15] M. Yoo, S. Yoon, and A. de Lozanne. Atomic force microscopy of ammonium perchlorate. *Materials Research Society Symposium Proceedings*, 296:221–226, 1993.

[16] J. Sharma and C.S. Coffey. Atomic force microscopy of hot spots in RDX and AP crystals. In K.K. Kuo, editor, *Challenges in Propellants and Combustion: 100 Years after Nobel*, pages 268–277. Begell House, New York, 1997.

[17] N. Kubota. *Propellants and Explosives*. Wiley, Weinheim, Germany, first edition, 2002.

[18] D.H. Liebenberg, Armstrong R.W., and J.J. Gilman. Structure and properties of energetic materials. *Materials Research Society Symposium Proceedings*, 296:ix, 1993.

[19] S.F. Sarner. *Propellant Chemistry*. Reinhold Publishing Corporation, New York, 1966.

[20] J.D. Hunley. The history of solid-propellant rocketry: What we do and do not know. In *35th AIAA, ASME, SAE, ASEE Joint propulsion conference and exhibit*, Los Angeles, California, 1999.

[21] A. Olivani, L. Galfetti, F. Severini, G. Colombo, F. Cozzi, F. Lesma, and M. Sgobba. Aluminum particle size influence on ignition and combustion of AP/HTPB/Al solid rocket propellants. In *Advances in Rocket Propellant Performance, Life and Disposal for Improved System Performance and Reduced Cost*, Aalborg, Denmark, 2002.

[22] G.A. Risha, E. Boyer, R.B. Wehrman, and K.K. Kuo. Performance comparison of HTPB-based solid fuels containing nano-sized energetic powder in a cylindrical hybrid rocket motor. In *38th AIAA/ASME/SAE/ASEE Joint Propulsion*

Conference and Exhibit, pages 1–12, Indianapolis, Indiana, 2002. American Institute of Aeronautics and Astronautics.

[23] P. Brousseau and C.J. Anderson. Nanometric aluminum in explosives. *Propellants, Explosives, Pyrotechnics*, 27:300–306, 2002.

[24] K.K. Kuo, T.A. Litzinger, and W.H. Hsieh. Interrelationship between solid propellant combustion and materials behavior. *Materials Research Society Symposium Proceedings*, 296:331–347, 1993.

[25] J.E. Field. Hot spot ignition mechanisms for explosives. *Accounts of Chemical Research*, 25:489–496, 1992.

[26] J.P. Ritchie. Molecular modeling of slip supposed to occur in the shock initiation of crystalline PETN. *Materials Research Society Symposium Proceedings*, 296:99–106, 1993.

[27] J.T. Hagan and M.M. Chaudhri. Fracture surface energies of high explosives PETN and RDX. *Journal of Materials Science*, 12:1055–1058, 1976.

[28] A.V. Raevskii, G.B. Manelis, V.V. Boldyrev, and L.A. Votinova. The part played by dislocations in the thermal decomposition of ammonium perchlorate crystals. *Doklady Akademii Nauk SSSR*, 160(5):1136–1137, 1965.

[29] W.E. Garner. Thermal decomposition, inflammation and detonation. *Proceedings of the Royal Society of London*, A246:203–206, 1958.

[30] J.E. Field, N.K. Bourne, S.J.P. Palmer, and S.M. Walley. Hot spot ignition mechanisms for explosives and propellants. *Philosophical Transactions of the Royal Society of London, Series A*, 339:269–283, 1992.

[31] M.M. Chaudhri and J.E. Field. The role of rapidly compressed gas pockets in the initiation of condensed explosives. *Proceedings of the Royal Society of London*, A340:113–128, 1974.

[32] R.E. Winter and J.E. Field. The role of localized plastic flow in the impact initiation of explosives. *Proceedings of the Royal Society of London*, A343:399–413, 1975.

[33] C. S. Coffey and J. Sharma. Lattice softening and failure in severely deformed molecular crystals. *Journal of Applied Physics*, 89:4797–4802, 2001.

[34] J.E. Field, G.M. Swallowe, and S.N. Heavens. Ignition mechanisms of explosives during mechanical deformation. *Proceedings of the Royal Society of London*, A382:231–244, 1982.

[35] J.C. Schumacher. *Perchlorates. Properties, Manufacture and Uses.* Reinhold Publishing Corporation, New York, first edition, 1960.

[36] S. Haussühl. Elastic and thermoelastic properties of isotypic $KClO_4$, $RbClO_4$, $TlClO_4$, NH_4ClO_4, $TiBF_4$, NH_4BF_4 and $BaSO_4$. *Zeitschrift für Kristallographic*, 192:137–145, 1990.

[37] H.W. Sandusky, B.C. Glancy, D.W. Carlson, W.L. Elban, and R.W. Armstrong. Relating deformation to hot spots in shock-loaded crystals of ammonium perchlorate. *Journal of Propulsion*, 7:518–525, 1991.

[38] S.M. Peiris, G.I. Pangilinan, and T.P. Russell. Structural properties of ammonium perchlorate compressed to 5.6 GPa. *Journal of Physical Chemistry A*, 104:11188–11193, 2000.

[39] F. Vazquez, R.S. Singh, and J.A. Gonzalo. Elastic and elasto-plastic constants of ammonium perchlorate. *Journal of Physics and Chemistry of Solids*, 37:451–455, 1976.

[40] J.F. Nye. *Physical Properties of Crystals*. Oxford University Press, Oxford, 1985.

[41] S.M. Peirs, G.I. Pangilinan, and T.P. Russell. Structural changes in ammonium perchlorate under compression. In Y. Horie, editor, *Shock Compression of Condensed Matter*, volume 505(1), pages 955–958, Utah, 1999. American Institute of Physics.

[42] R.W.G. Wyckoff. *Crystal Structures*, volume 3. Interscience Publishers, New York, 1963.

[43] A. Kelly, G.W. Groves, and P. Kidd. *Crystallography and Crystal Defects*. Wiley, Chichester, England, revised edition, 2000.

[44] M. Yoo, S. Yoon, and A. de Lozanne. Atomic force microscopy of ammonium perchlorate. *Journal of Vacuum Science and Technology B*, 12(3):1638–1641, 1994.

[45] R.W. Hertzberg. *Deformation and Fracture Mechanics of Engineering Materials*. John Wiley and sons, New York, fourth edition edition, 1996.

[46] R.W.K. Honeycombe. *The Plastic Deformation of Metals*. Edward Arnold, London, first edition, 1984.

[47] A.J. Forty. The generation of dislocations during cleavage. *Proceedings of the Royal Society A*, 242:392–399, 1957.

[48] S. Augustine and E. Mathai. Growth morphology , and micro-indentation analysis of Bi_2Se_3, $Bi_{1.8}In_{0.2}Se_3$ and $Bi_2Se_{2.8}Te_{0.2}$ single crystals. *Materials Research Bulletin*, 36:2251–2261, 2001.

[49] Ph. Ebert, F. Kluge, M. Yurechko, B. Grushko, and K. Urban. Structure and composition of cleaved and heat treated tenfold surfaces of decagonal Al-Ni-Co quasicrystals. *Surface Science*, 523:298–306, 2003.

[50] R.A. Schultz, M.C. Jensen, and R.C. Bradt. Single crystal cleavage of brittle materials. *International Journal of Fracture*, 62:291–312, 1994.

[51] P.J. Herley and Levy P.W. Quantitative studies on radiation induced dislocations and decomposition kinetics of ammonium perchlorate. *7th International Symposium on the Reactivity of Solids*, pages 387–397, 1972.

[52] B.C. Beard, H.W. Sandusky, and B.C. Glancy. Defect density measurements in shocked single crystal ammonium perchlorate by X-ray photoelectron spectroscopy. *Journal of Materials Research*, 7(12):3266–3274, 1992.

[53] C.T. Lin. Study of growth spirals and screw dislocation on $YBa_2Cu_3O_{7-\delta}$ single crystals. *Physica C*, 337:312–316, 2000.

[54] S. Amelinckx. *The direct observation of dislocations.* Academic Press, New York and London, first edition, 1964.

[55] B.R. Pamplin. *Crystal Growth.* Pergamon Press, New York, second edition, 1980.

[56] F.K. de Theije, E. Veenendaal, W.J.P. Enckevort, and E. Vlieg. Oxidative etching of cleaved synthetic diamond {111} surfaces. *Surface Science*, 492:91–105, 2001.

[57] S.K. Hong, B.J. Kim, H.S. Park, S.Y. Yoon, and T.I. Kim. Evaluation of nanopipes in MOCVD grown (0001) GaN/Al_2O_3 by wet chemical etching. *Journal of Crystal Growth*, 191:275–278, 1998.

[58] T. Nishiguchi, Y. Masuda, S. Ohshima, and S. Nishino. A proposal for CVD growth of 15R-SiC by observing the etch pits on 15R-SiC (000-1) C-face. *Journal of Crystal Growth*, 237-239:1239–1243, 2002.

[59] W.G. Johnston. Dislocation etch pits in non-metallic crystals. In J.E. Burke, editor, *Progress in Ceramic Science*, volume 2, pages 1–76. Pergamon Press Inc., New York, first edition, 1962.

[60] G.E. Dieter. *Mechanical Metallurgy.* McGraw-Hill, Boston, Massachusetts, third edition edition, 1986.

[61] T.J. Bell and E.G. Thwaite. Recent developments in hardness testing and their implications for standardization. *Annals of the CIRP*, 48:449–452, 1999.

[62] Y.T. Cheng, T. Page, G.M. Pharr, M.V. Swain, and K.J. Wahl. Fundamentals and applications of instrumented indentation in multidisciplinary research. *Journal of Materials Research*, 19(1):1–2, 2004.

[63] A.C. Fischer-Cripps. A review of analysis methods for sub-micron indentation testing. *Vacuum*, 58:569–585, 2000.

[64] D.A. Lucca, E. Brinksmeier, and G. Goch. Progress in assessing surface and subsurface integrity. *Annals of the CIRP*, 47:669–693, 1998.

[65] J.L. Hay and G.M. Pharr. Instrumented indentation testing. In *ASM Handbook Volume 8: Mechanical Testing and Evaluation*, pages 232–243. CRC Press, Boca Raton, FL, 2000.

[66] W.C. Oliver and G.M. Pharr. An improved technique for determining hardness and elastic modulus using load and displacement sensing indentation experiments. *Journal of Materials Research*, 7(6):1564–1583, 1992.

[67] M.W. Swain. Mechanical property characterization of small volumes of brittle materials with spherical tip indenters. *Materials Science and Engineering, series A*, 253:160–166, 1998.

[68] B.N. Lucas, C.T. Rosenmayer, and W.C. Oliver. Mechanical characterization of sub-micron polytetrafluoroethylene (PTFE) thin films. *Materials Research Society Symposium Proceedings: Thin films-stresses and mechanical properties*, 505:97–102, 1998.

[69] Y.-H Lee and D. Kwon. Measurement of residual-stress effect by nanoindentation on elastically strained (100) W. *Scripta Materialia*, 49:459–465, 2003.

[70] B.N. Lucas and W.C. Oliver. Indentation power-law creep of high-purity indium. *Metallurgical and Materials Transactions A*, 30A:601–610, 1999.

[71] G. M. Pharr. Measurement of mechanical properties by ultra low load indentation. *Materials Science and Engineering, series A*, 253:151–159, 1998.

[72] M.R. VanLandingham. Review of instrumented indentation. *Journal of Research of the National Institute of Standards and Technology*, 108:249–265, 2003.

[73] International Organization for Standardization (ISO). Metallic materials - Instrumented indentation test for hardness and materials parameters - Part 1: Test method. *ISO14577-1*, 2002.

[74] International Organization for Standardization (ISO). Metallic materials - Instrumented indentation test for hardness and materials parameters - Part 2: Verification and calibration of testing machines. *ISO 14577-2*, 2002.

[75] International Organization for Standardization (ISO). Metallic materials - Instrumented indentation test for hardness and materials parameters - Part 3: Calibration of reference blocks. *ISO 14577-3*, 2002.

[76] American Society for Testing (ASTM) and Materials. WK382: Practice for instrumented indentation testing. date initiated: 02-07-2003.

[77] J.L. Loubet, J.M. Georges, O. Marchesini, and G. Meille. Vickers indentation curves of magnesium oxide (MgO). *Journal of Tribology*, 106:43–48, 1984.

[78] M.F. Doerner and W.D. Nix. A method for interpreting the data from depth sensing indentation instrument. *Journal of Materials Research*, 1:601–609, 1986.

[79] I. Todhunter and K. Pearson. The application of potentials to the theory of elasticity including Hertz's researches on impact of spheres. In Cambridge University Press, editor, *History of the theory of elasticity*, volume 2, pages 235–307. Dover publications, New York, first edition, 1893.

[80] A.E.H. Love. The stress produced in a semi-infinite solid by pressure on part of the boundary. *Philosophical Transactions of the Royal Society of London. Series A*, 228:377–420, 1929.

[81] A.E.H. Love. Boussinesq problem of a rigid cone. *The Quarterly Journal of Mathematics*, 10:161, 1939.

[82] I.N. Sneddon. The relation between load and penetration in the axisymmetric Boussinesq problem for a punch of arbitrary profile. *International Journal of Engineering Science*, 3:47–57, 1965.

[83] D. Tabor. Deformation of metals by spherical indenter. Shallowing and elastic recovery. In D. Tabor, editor, *The Hardness of Metals*, pages 84–93. Clarendon Press. Oxford, New York, first edition, 2000.

[84] S. I. Bulychev, V.P. Alekhin, M.Kh. Shorshorov, A.P. ternovskii, and G.D. Shnyrev. Work of plastic and elastic deformation during indenter indentation. *Strength Materials*, 12:1084–1089, 1976.

[85] G.M. Pharr and W.C. Oliver. On the generality of the relationship among contact stiffness, contact area and elastic modulus during indentation. *Journal of Materials Research*, 7:613–617, 1992.

[86] R.B. King. Elastic analysis of some punch problems for a layered medium. *International Journal of Solids and Structures*, 23(12):1657–1664, 1987.

[87] J.B. Pethica, R. Hutchings, and W.C. Oliver. Hardness measurement at penetration depths as small as 20 nm. *Philosophical Magazine A*, 48(4):593–606, 1983.

[88] W.C. Oliver, R. Hutchings, and J.B. Pethica. Measurement of hardness at indentation depth as low as 20 nanometers. In P.J. Blau and B.R. Lawn, editors, *STP889: Micro-indentation Techniques in Materials Science and Engineering*, pages 90–108. ASTM, Philadelphia, 1984.

[89] A. Bolshakov, W.C. Oliver, and G.M. Pharr. An explanation for the shape of nanoindentation unloading curves based on finite element simulation. *Materials Research Society Symposium Proceedings: Thin Films-Stresses and Mechanical Properties*, 356:675–680, 1995.

[90] G.M. Pharr and A. Bolshakov. Understanding nanoindentation unloading curves. *Journal of Materials Research*, 17(10):2660–2671, 2002.

[91] C. Tromas, J.C. Girard, V. Audurier, and J. Woirgard. Study of the low stress plasticity in single crystal MgO by nanoindentation and atomic force microscopy. *Journal of Materials Science*, 34:5337–5342, 1999.

[92] W.W. Gerberich, J.C. Nelson, E.T. Lilleodden, P. Anderson, and J.T. Wyrobek. Indentation induced dislocation nucleation: the initial yield point. *Acta Materialia*, 44(9):3585–3598, 1996.

[93] D.F. Bahr, D.E. Kramer, and W.W. Gerberich. Non-linear deformation mechanisms during nanoindentation. *Acta Materialia*, 46(10):3605–3617, 1998.

[94] H.S. Leipner, D. Lorenz, A. Zeckzer, and P. Grau. Dislocation-related pop-in effect in gallium arsenide. *physica status solidi a*, 183(2):R4–R6, 2001.

[95] D.A. Lucca, M.J. Klopfstein, R. Ghisleni, and G. Cantwell. Investigation of polished single crystal ZnO by nanoindentation. *CIRP Annals-Manufacturing Technology*, 51(1):483–486, 2002.

[96] Y.G. Gogotsi, V. Domnich, S.N Dub, A. Kailer, and K.G. Nickel. Cyclic nanoindentation and Raman microspectroscopy study of phase transformations in semiconductors. *Journal of Materials Research*, 15(4):871–879, 2000.

[97] J. E. Bradby, J.S. Williams, J. Wong-Leung, M. V. Swain, and P. Munroe. Mechanical deformation of InP and GaAs by spherical indentation. *Applied Physics Letters*, 78(21):3235–3237, 2001.

[98] C.A. Schuh and T.G. Nieh. A nanoindentation study of serrated flow in bulk metallic glasses. *Acta Materialia*, 51:87–99, 2003.

[99] T.F. Page, W.C. Oliver, and J.C. M^c Hargue. The deformation behavior of ceramic crystals subjected to very low load (nano) indentation. *Journal of Materials Research*, 7:450–473, 1992.

[100] J.E. Bradby, S.O. Kucheyev, S.J. Williams, J. Wong-Leung, M.V. Swain, P. Munroe, G. Li, and M.R. Phillips. Indentation-induced damage in GaN epilayers. *Applied Physics Letters*, 80(3):383–385, 2002.

[101] S.O. Kucheyev, J.E. Bradby, J.S. Williams, C. Jagadish, and M.V. Swain. Mechanical deformation of single crystal ZnO. *Applied Physics Letters*, 80(6):956–958, 2002.

[102] W. Wang, C.B. Jiang, and K. Lu. Deformation behavior of Ni_3Al single crystals during nanoindentation. *Acta Materialia*, 51:6169–6180, 2003.

[103] Y.L. Chiu and A.H.W. Ngan. Time-dependent characteristics of incipient plasticity in nanoindentation of a Ni_3Al single crystal. *Acta Materialia*, 50:1599–1611, 2002.

[104] D.A. Lucca, M.J. Klopfstein, O.R. Mejia, L. Rossettini, and L. De Luca. Investigation of the near surface mechanical properties of ammonium perchlorate using nanoindentation. In *Ninth International Workshop on Combustion and Propulsion: Novel Energetic Materials and Applications*, Lerici, Italy, 2003.

[105] G. Yu, H. Ishikawa, T. Egawa, T. Soga, J. Watanabe, T. Jimbo, and M. Umeno. Mechanical properties of the GaN thin films deposited on sapphire substrate. *Journal of Crystal Growth*, 189/190:701–705, 1998.

[106] D. Caceres, I. Vergara, and R. Gonzales. Nanoindentation on AlGaN thin films. *Journal of Applied Physics*, 86(12):6773–6778, 1999.

[107] K.L. Johnson. *Contact Mechanics*. Cambridge University Press, Cambridge, 1985.

[108] M. Oden, H. Ljungcrantz, and L. Hultman. Characterization on the induced plastic zone in a single crystal TiN(001) film by nanoindentation and transmission electron microscopy. *Journal of Materials Research*, 12(8):2134–2142, 1997.

[109] S.G. Corcoran, R.J. Colton, E.T. Lilleodden, and W.W. Gerberich. Anomalous plastic deformation at surfaces: Nanoindentation of gold single crystals. *Physical Review B*, 55(24):R16057–R16060, 1997.

[110] D.F. Bahr, D.E. Wilson, and D.A. Crowson. Energy considerations regarding yield points during indentation. *Journal of Materials Research*, 14(6):2269–2275, 1999.

[111] S.A. Syed Asif, K.J. Wahl, and R.J. Colton. The influence of oxide and adsorbates on the nanomechanical response of silicon surfaces. *Journal of Materials Research*, 15(2):546–553, 2000.

[112] A.B. Mann and J.B. Pethica. The role of atomic size asperities in the mechanical deformation of nanocontacts. *Applied Physics Letters*, 69(7):907–909, 1996.

[113] G. Feng and A.H.W. Ngan. Creep and strain burst in indium and aluminum during nanoindentation. *Scripta Materialia*, 45:971–976, 2001.

[114] Q. Ma and D.R. Clarke. Size dependent hardness of silver single crystals. *Journal of Materials Research*, 10(4):853–861, 1995.

[115] N.A. Fleck, G.M. Muller, M.F. Ashby, and J.W. Hutchinson. Strain gradient plasticity: Theory and experiment. *Acta Metallurgica et Materialia*, 42(2):475–487, 1994.

[116] Y. Liu and A.H.W. Ngan. Depth dependence hardness in copper single crystals measured by nanoindentation. *Scripta Materialia*, 44:237–241, 2001.

[117] G. Alcala, P. Skeldon, G.E. Thompson, A.B. Mann, H. Habazaki, and K. Shimizu. Mechanical properties of barrier-type anodic alumina films using nanoindentation. *Surface and Coatings Technology*, 173(2-3):293–298, 2003.

[118] R.C. Cammarata, T.E. Schlesinger, C. Kim, S.B. Qadri, and A.S. Edelstein. Nanoindentation study of the mechanical properties of copper-nickel multilayered thin films. *Applied Physics Letters*, 56(19):1862–1864, 1990.

[119] Ya.M. Soifer, A. Verdyan, and L. Rapoport. Nanoindentation size effect in alkali-halide single crystals. *Materials Letters*, 56:127–130, 2002.

[120] K. Sangwal. On the reverse indentation size effect and micro-hardness measurement of solids. *Materials Chemistry and Physics*, 63:145–152, 2000.

[121] J. Gong, H. Miao, Z. Zhao, and Z. Guan. Load-dependence of the measured hardness of Ti(C,N)-based cermets. *Materials Science and Engineering*, A303:179–186, 2001.

[122] M.F. Ashby. The deformation of plastically non-homogeneous materials. *Philosophical Magazine*, 21:399–424, 1970.

[123] Y.Y. Lim and M.M. Chaudhri. The effect of the indenter load on the nanohardness of ductile metals: an experimental study on polycrystalline work-hardened and annealed oxygen free copper. *Philosophical Magazine A*, 79(12):2979–3000, 1999.

[124] A. Flores and F.J. Balt Calleja. Mechanical properties of poly(ethylene terephthalate) at the near surface from depth sensing experiments. *Philosophical Magazine A*, 78(6):1283–1297, 1998.

[125] M.C. Shaw. *Metal Cutting Principles*. Oxford University Press, NY, first edition, 1984.

[126] K.G. Budinski and M.K. Budinski. *Engineering Materials: Properties and Selection*. Prentice Hall, NJ, seven edition, 2002.

[127] J.M. Thomas, J.O. Williams, V.V. Boldyrev, and Yu. P. Savintsev. Investigations of dislocation etch pits in NH_4ClO_4 doping with copper. *Izvestiya Akademii Nauk SSSR, Neorganicheskie Materialy*, 11(6):1035–1037, 1972.

[128] B. Bhushan, K. Kulkarni, W. Bonin, and J.T. Wyrobek. Nanoindentation and picoindentation measurements using a capacitive transducer system in atomic force microscopy. *Philosophical Magazine A*, 74(5):1117–1128, 1996.

[129] E.S. Berkovich. Three-faceted diamond pyramid for micro-hardness testing. *Industrial Diamond Review*, 11(127):129–132, 1951.

[130] J. J. Gilman and W. G. Johnston. The origin and growth of glide bands in lithium fluoride crystals. In J.C. Fisher, W. G. Johnston, R. Thomson, and T. Vreeland, editors, *Dislocations and Mechanical Properties of Crystals*, pages 116–163. John Wiley and sons, Inc., NY, first edition, 1956.

[131] P.J. Halfpenny, K.J. Roberts, and J.N. Sherwood. Dislocations in energetic materials. *Journal of Materials Science*, 19:1629–1637, 1984.

[132] I.M. Dawson and V. Vand. The observation of spiral growth-steps in n-paraffin single crystals in the electron microscope. *Proceedings of the Royal Society of London series A: Mathematical and Physical sciences*, 206(1087):555–562, 1950.

[133] J.M. Thomas and J.O. Williams. Lattice imperfections in organic solids. *Transactions of the Faraday Society*, 63:1922–1928, 1967.

[134] J. Sharma, R. W. Armstrong, W. L. Elban, C. S. Coffey, and H. W. Sandusky. Nanofractography of shocked RDX explosive crystals with atomic force microscopy. *Applied Physics Letters*, 78:457–459, 2001.

[135] K. Miyahara, S. Matsuoka, and N. Nagashima. Nanoindentation measurements for a tungsten (001) single crystal. *JSME International Journal*, 41(4):562–568, 1998.

[136] J.H. Schneibel and L. Martinez. Atomic force microscope of slip lines in FeAl. *Journal of Materials Research*, 10(9):2159–2161, 1995.

[137] W. Zielinski, H. Huang, S. Venkataraman, and W.W. Gerberich. Dislocation distribution under a micro-indentation into an iron-silicon single crystal. *Philosophical Magazine A*, 72(5):1221–1237, 1995.

[138] N.A. Stelmashenko, M.G. Walls, L.M. Brown, and Yu. V. Milman. Microindentations on W and Mo oriented single crystals : an STM study. *Acta Metallurgica et Materialia*, 41(10):2855–2865, 1993.

[139] C.L. Woodcock and D.F. Bahr. Plastic zone evolution around small scale indentations. *Scripta Materialia*, 43:783–788, 2000.

[140] G. Binnig and H. Rohrer. Scanning tunneling microscope from birth to adolescence. *Reviews of Modern Physics*, 59(3):615–625, 1987.

[141] S. Amelinckx, D. van Dyck, J. van Landuyt, and G. van Tendeloo. Scanning force microscope. In R. Wiesendanger, editor, *Handbook of Microscopy*, volume 2, pages 828–843. Weinheim, New York; Basel; Cambridge; Tokyo, 1997.

[142] U.D. Schwarz, H. Haefke, T. Jung, E. Meyer, H.J. Guntherodt, R. Steiger, and J. Bohonek. Plate like microcrystals of silver bromide investigated by scanning force microscope. *Ultramicroscopy*, 41:435, 1992.

[143] E. Henderson, P.G. Haydon, and D.S. Sakaguchi. Actin filament dynamics in living glial cells imaged by atomic force microscopy. *Science*, 257:1944, 1992.

[144] D. Anselmetti, R. Luthi, E. Meyer, T. Richmond, M. Dreier, J.E. Frommer, and H.-J. Guntherodt. Attractive-mode imaging of biological materials with dynamic force microscopy. *Nanotechnology*, 5:87–94, 1994.

[145] G. Friedbacher, P.K. Hansma, E. Ramli, and G.D. Stucky. Imaging powders with the atomic force microscope: From biominerals to commercial materials. *Science*, 253:1261, 1991.

[146] W.A. Rees, R.W. Keller, J.P. Vesenka, G. Yang, and C. Bustamante. Evidence of DNA bending in transcription complexes imaged by scanning force microscopy. *Science*, 260:1646–1649, 1993.

[147] H.L. Weisenhorn, P. Maivald, H.-J. Butt, and P.K. Hansma. Measuring adhesion, attraction, and repulsion between surfaces in liquids with an atomic-force microscope. *Physical Review B*, 45:11226, 1992.

[148] J. Hu, X.-D. Xiao, D.F. Ogletree, and M. Salmeron. Imaging the condensation and evaporation of molecularly thin films of water with nanometer resolution. *Science*, 268:267–269, 1995.

[149] F.J. Giessibl. Atomic force microscopy in ultrahigh vacuum. *Japanese Journal of Applied Physics*, 33:3726, 1994.

[150] K. Sangwal, P. Gorostiza, J. Servat, and F. Sanz. Atomic force microscopy study of nanoindentation deformation and indentation size effect in MgO crystals. *Materials Research Society*, 14(10):3973–3982, 1999.

Appendix A

Physical Properties of Ammonium Perchlorate

The principal physical properties of AP are presented in Table A.1 and A.2.

Physical Properties	**Symbols**	**Value**	**Units**	**Reference**
Weight % oxygen		54.5		[19]
Molecular weight		117.497		[19]
Lattice type		Orthorhombic, Cubic		[19]
Lattice parameters	a	9.202	Å	[42]
	b	5.816	Å	[42]
	c	7.449	Å	[42]

Table A.1: Principal properties of AP.

Physical Properties	**Symbols**	**Value**	**Units**	**Reference**
Transition Temp.		240	°C	[19]
Decomposition Temp.		270	°C	[19]
Density	ρ	1.95	g/cm^3	[19]
Heat capacity	C	30.61	cal/mole-°C	[19]
Heat of formation(25°C)		-70.73	Kcal/mole	[19]
Lattice energy		602	KJ/mole	[19]
Electrostatic energy		625.5	KJ/mole	[19]

Table A.2: Principal properties of AP.

Appendix B

Equivalent Crystallographic Planes of AP

Inspection of the unit cell shows four identical and symmetric {210} planes. Similarly there are two identical {001} planes in the crystallographic cell. Although these planes are different relative to each other mathematically, they are physically and chemically equivalent. Figure B.1 shows the family of the {210} planes namely: (210), $(\bar{2}\bar{1}0)$, $(\bar{2}10)$ and $(2\bar{1}0)$. Figure B.2 shows the family of the {001} planes namely: (001), $(00\bar{1})$.

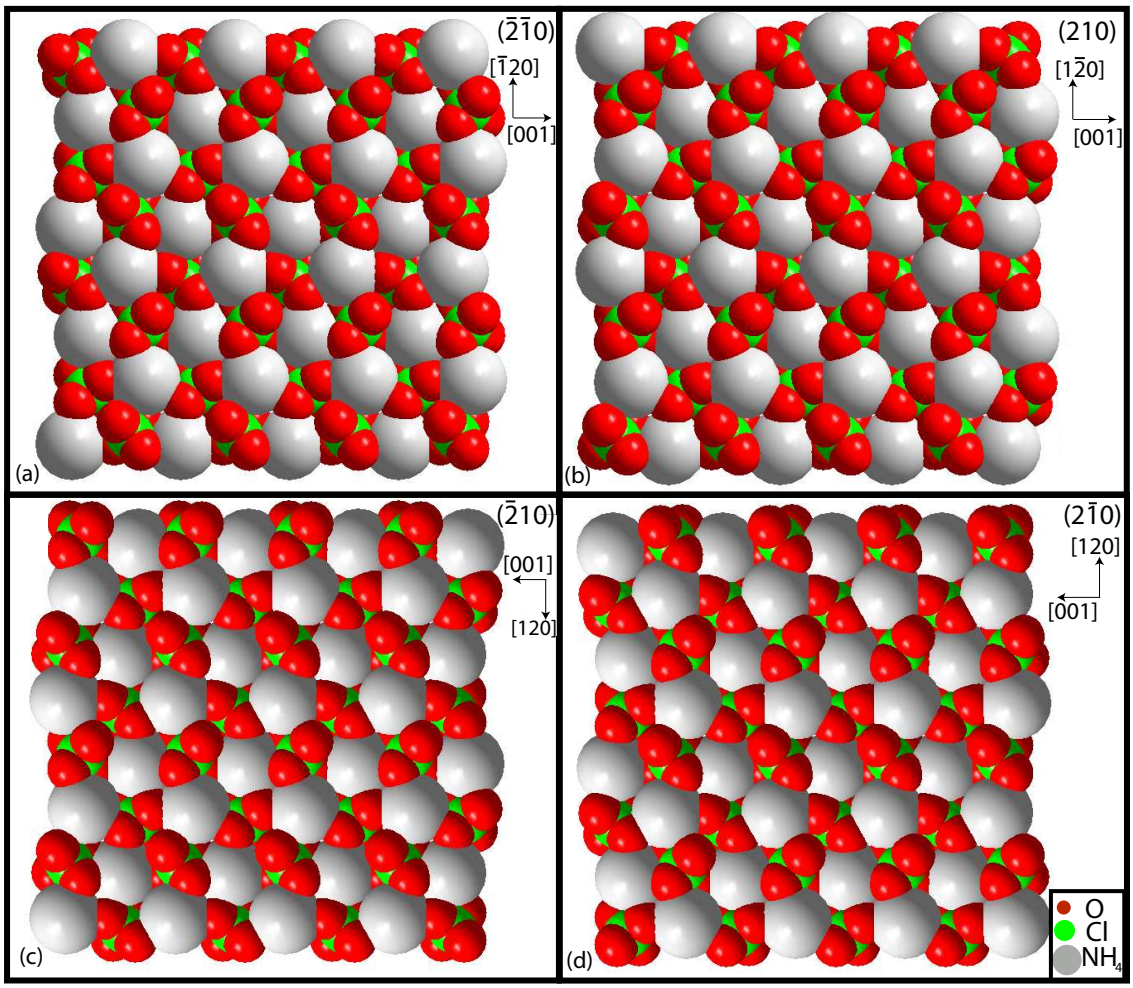

Figure B.1: Projection of the equivalent {210} planes: (a) (210), (b) $(\bar{2}\bar{1}0)$, (c) $(\bar{2}10)$, and (d) $(2\bar{1}0)$.

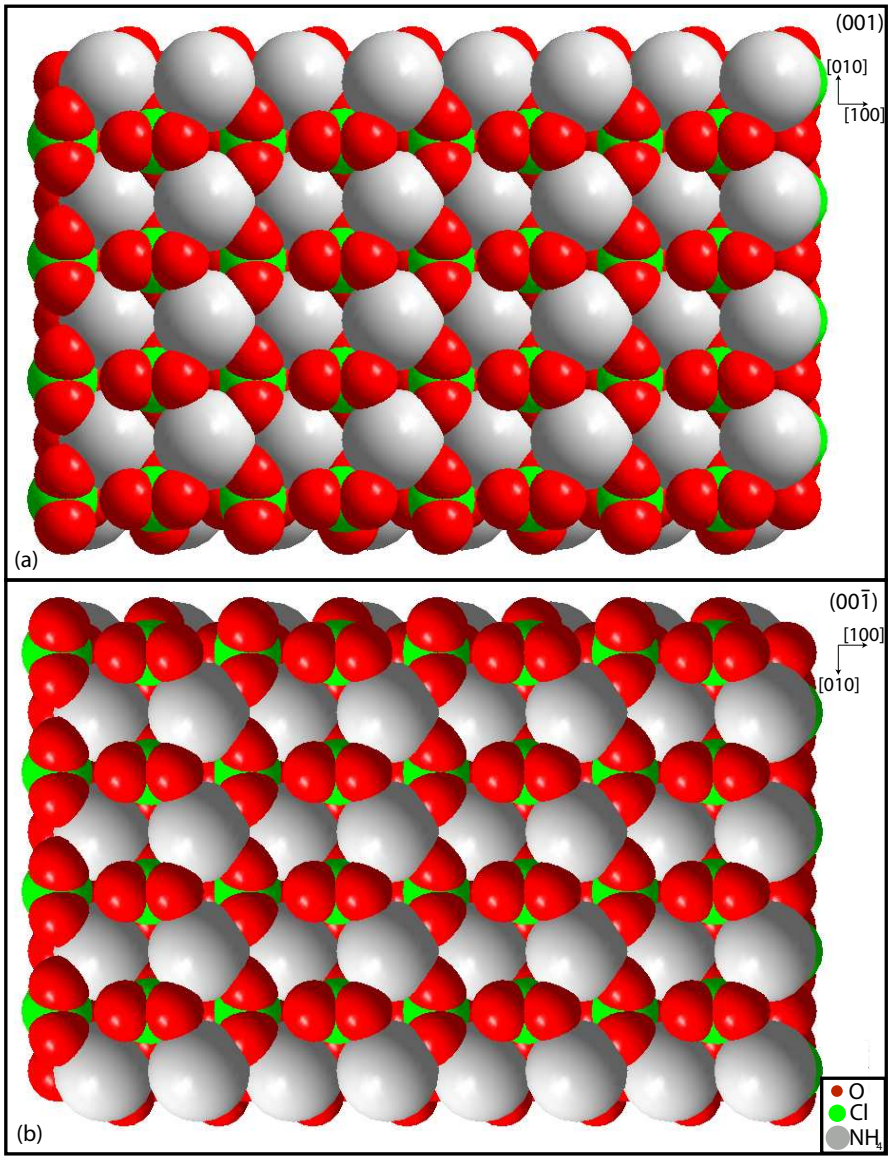

Figure B.2: Projection of the equivalent {001} planes: (a) (001), and (b) (00$\bar{1}$).

Appendix C

Machine Compliance and Area Function Calculation

The measured displacement of the indenter consists of three parts: the elastic and/or plastic deformation of the specimen, the elastic deformation of the indenter, and the elastic deformation of the load frame of the apparatus. The elastic deformation of the indenter has been accounted for by introducing the reduced modulus, E_r. To obtain the response of only the specimen, the elastic deformation of the load frame and mounting must also be subtracted from the measured displacements. The machine compliance (C_f) is needed to evaluate the deformation of the machine and the sample mounting. The machine-sample can be modeled as two springs in series. The total compliance is then:

$$C_{tot} = C_f + C_s \tag{C.1}$$

where C_s is the compliance of the specimen and C_f is the compliance of the machine. Using $C_s = 1/S$ and Eq.(2.6), we can rewrite Eq.(C.1):

$$C_{tot} = C_f + \frac{\sqrt{\pi}}{2E_r}\frac{1}{\sqrt{A}} \tag{C.2}$$

from this equation it follows that a plot of C_{tot} vs. $1/\sqrt{A}$ gives a straight line if E_r is assumed to not depend on the indentation depth. The slope of this line is

proportional to $1/E_r$, and the intercept of the line with the ordinate defines the load-frame compliance C_f. It is obvious from Eq.(C.2), that the contribution of the load-frame compliance to the total compliance increases as the value of the second term on the right hand side decreases. This is achieved either by increasing the projected contact area (i.e. by increasing the maximum load) or by investigating very stiff materials.

The calibration applied in this work was described by Oliver and Pharr [66]. The material used for the calibration was fused silica with a well-known elastic modulus of 72 GPa and Poisson's ratio $\nu = 0.170$. Using Eq.(2.7) the reduced modulus is 69.6 GPa, where $E_i = 1141$ GPa and $\nu_i = 0.07$ for the diamond indenter [66]. The fused silica sample was mounted in the same way that the AP crystals in order to consider the compliance of the mounting in the total compliance.

The calibration was divided in two regions, one for high load between 1500 and 10000 μN equivalent to a contact depth between 70 and 180 nm, and one for low load between 50 and 1000 μN (5 to 55 nm). Two area functions were determined but only one machine compliance was calculated from the high load region where the machine compliance is more significant.

The calibration was performed following the steps:

1. Five indentations were performed at 1000 μN intervals, from 1000 μN to 10000 μN. For the low depth area functions the indentations were performed at 200 μN intervals, from 200 μN to 800 μN.

2. For each indentation the nanoindentation software plots the load vs. penetration depth curve using a C_f value, in the calibration procedure the C_f was set to be equal to zero.

3. The total compliance C_{tot} was determined by derivation of the power law ap-

proximation of the unloading curve, Eq.(2.5), obtaining:

$$C_{tot} = \frac{dh}{dP} = \frac{1}{\alpha m h^{m-1}} = \frac{1}{\alpha m (h_{max} - h_f)^{m-1}} \tag{C.3}$$

4. The projected contact area was calculated using the standard area function proposed by Oliver and Pharr [66]:

$$A = 24.5h_c^2 + C_1 h_c + C_2 h_c^{1/2} + C_3 h_c^{1/4} + C_4 h_c^{1/8} + C_5 h_c^{1/16} \tag{C.4}$$

the lead term describes a perfect Berkovich indenter and the others describe deviation from the Berkovich geometry due to blunting of the tip. C_1, C_2, C_3, C_4 and C_5 come from step 9 (for the first calculation of A we used $C_1 = C_2 = C_3 = C_4 = C_5 = 0$).

5. Substituting Eq.(2.5):

$$S = \frac{dP}{dh} = \frac{2}{\sqrt{\pi}} E_r \sqrt{A} \tag{C.5}$$

in Eq.(C.1), we obtain:

$$C_{tot} = \left(\frac{\sqrt{\pi}}{2E_r}\right) \frac{1}{\sqrt{A}} + C_f \tag{C.6}$$

Equation(C.6) can be seen as a liner equation of the kind:

$$y = mx + q \tag{C.7}$$

where y = C_{tot} and x = $1/\sqrt{A}$ are known from steps 3 and 4. Plotting the values of y and x of each indentation and fitting a linear equation to these points the value of E_r and C_f were obtained.

6. Knowing C_{tot}, C_f and using Eq.(C.2) a new value of S was obtained by:

$$S = \frac{1}{C_{tot} - C_f} \tag{C.8}$$

7. A new value for h_c was obtained using:

$$h_c = h_{max} - \epsilon \frac{P_{max}}{S} \tag{C.9}$$

8. New values for the projected contact area were evaluated using Eq.(2.6):

$$A = \frac{\pi}{4}(\frac{S}{E_r})^2 \tag{C.10}$$

9. The value of h_c and A were then plotted, and fitted by a power equation of the kind described in step 4 and the coefficients C_1, C_2, C_3, C_4, C_5 were evaluated as shown in Fig. C.1.

10. We started over from step 4 until C_f converged.

For the calibration using four constants, the cycle was repeated 5 times before the value of C_f converged to 2.79 nm/mN, the slope of the best fit line is m = 12.3 nm

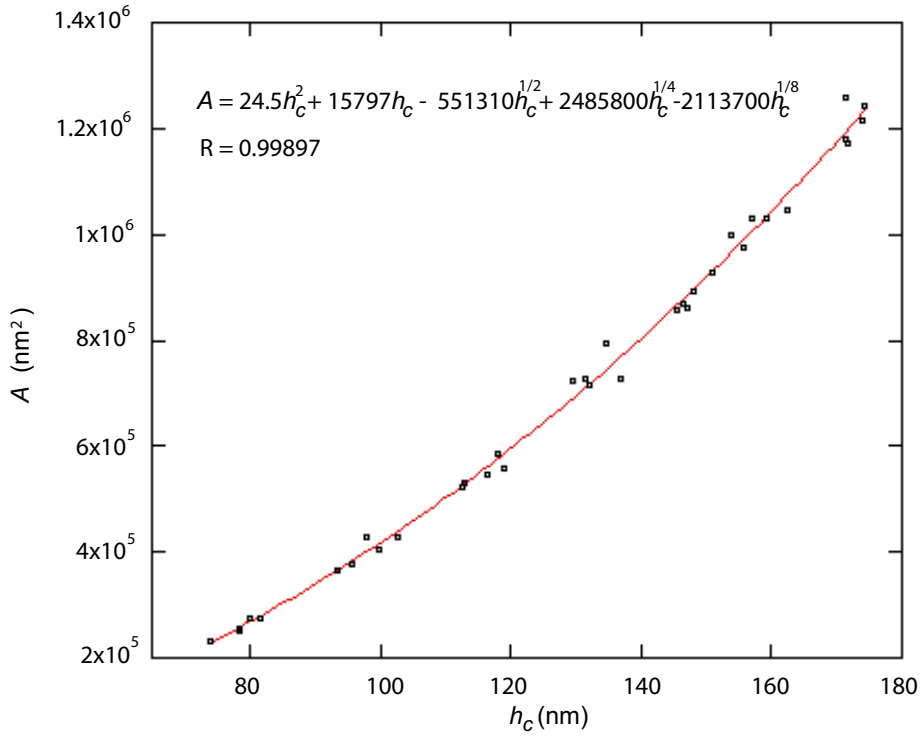

Figure C.1: Determination of the coefficients of the area function for a Berkovich indenter.

which gives a reduced modulus of 69.56 GPa and the four constants for the high load region, h_c between 70 and 180 nm, are:

$$C_1 = 15797$$

$$C_2 = \text{-}551310$$

$$C_3 = 2485800$$

$$C_4 = \text{-}2113700$$

And for the low load region, h_c between 5 and 50 nm, are:

$$C_1 = 3517.3$$

$$C_2 = \text{-}141120$$

$$C_3 = 1271200$$

$$C_4 = \text{-}3003700$$

The machine compliance correction is more important for materials with high elastic modulus. In our case, the machine compliance was negligible and almost all the contribution corresponded to the compliance of the machine.

Appendix D

Atomic Force Microscope

The invention of scanning tunneling microscopy (STM) in 1982 by Binnig and Roher [140] triggered the development of new techniques which use scanning point probes to sense local properties of surfaces. Among these techniques, atomic force microscopy (AFM), has become the most wide-spread and commercially successful tool, and is used in physical, chemical, biological, and medical research laboratories [141].

A force microscope detects forces acting between the sample surface and a sharp tip which is mounted on a softly sprung cantilever beam. A feedback system which controls the vertical z-position of the tip on the sample surface keeps the deflection of the cantilever constant. Moving the tip relative to the sample in the (x,y) plane of the surface by means of a piezoelectric drives, the actual z-position of the tip can be recorded as a function of the (x,y) position. The obtained three dimensional data represent a map of equal forces. The data can be analyzed and visualized through computer processing. In a typical force microscope, cantilever deflections in the range from 0.1 Å to a few micrometers are measured, corresponding to forces from 10^{-13} to 10^{-5} N [141]. Figure D.1 shows a typical set-up of a force microscope.

A sample is suitable to be studied by AFM as long as it is solid and clean. For instance, insulator materials that are highly sensitive to light or electron beams, can be easily studied [142]. In a liquid environment, even soft samples such as the

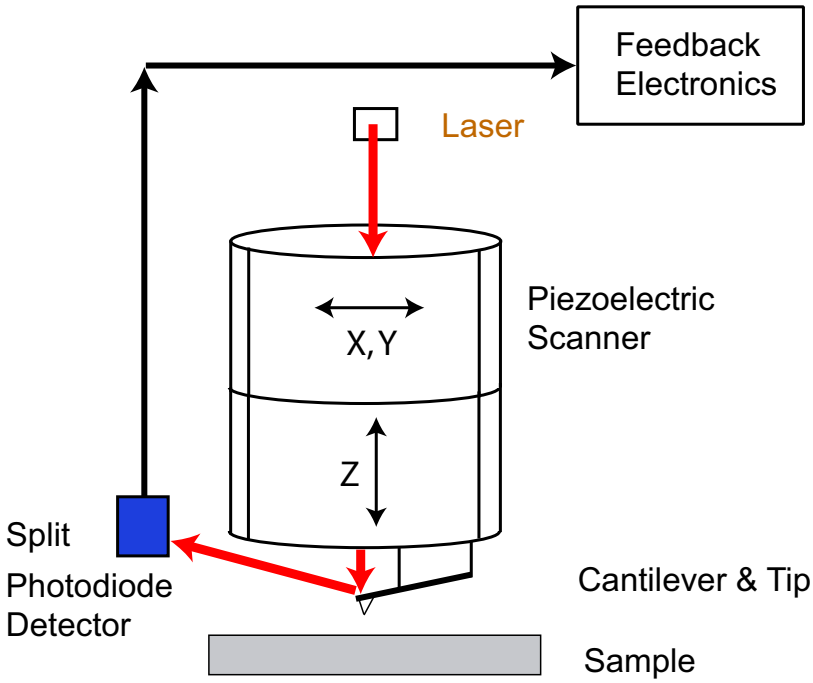

Figure D.1: Schematic of the set-up of a typical atomic force microscope.

biological membranes of a cell or a virus have been successfully imaged [143, 144]. Even powder particles or singular molecules have studied [145, 146]. Samples can be analyzed without any special treatment and in many environmental conditions such as ambient air, liquids [147], gaseous atmospheres [148] and ultrahigh vacuum [149].

There are 3 typical modes of AFM:

1. **Contact mode AFM** This mode operates by scanning the tip while examining the change in the cantilever deflection with a split photodiode detector. A feedback loop maintains a constant deflection between the cantilever and the sample by vertically moving the scanner at each (x,y) point. By maintaining a constant cantilever deflection, the force between the tip and the sample remains constant, the force is calculated from Hooke's law: $F = -kx$. The distance the scanner moves vertically at each data point (x,y) is stored to form the image of the surface.

2. **Tapping mode AFM** This mode operates by scanning a tip at the end of

a cantilever oscillating near its resonance frequency and an amplitude of approximately 20 to 100 nm. The tip slightly taps on the sample surface during scanning, contacting the surface at the bottom of its swing. The feedback loop maintains a constant oscillation amplitude by maintaining a constant RMS of the oscillation signal received by the photodiode detector. The vertical position of the scanner at each (x,y) data point in order to maintain the amplitude is stored by the computer to form the image of the surface.

3. **Non-contact mode AFM** This mode operates by scanning a tip at the end of a cantilever oscillating slightly above its resonance frequency with an amplitude of few nanometers ($\leq$ 10 nm). The tip does not contact the surface of the sample, but oscillates above the absorbed fluid layer on the surface. The cantilever's resonant frequency is decreased by Van der Waals forces, this reduction in frequency causes the amplitude to decrease. The feedback loop maintains a constant oscillation amplitude or frequency by vertically moving the scanner at each (x,y) point. The distance the scanner moves vertically is stored by the computer to form the image of the surface.

SCANNERS

AFM scanners are made from piezoelectric material, which contracts and expands proportionally to an applied voltage. Whether they elongate or contract depends upon the polarity of the voltage. The scanner is constructed by combining independently operated piezo electrodes for x, y and z into a single tube, forming a scanner which can manipulate sample and probes with extreme precision.

PROBES

There are two types of probes: contact mode probes and tapping mode probes. Silicon nitride probes primarily used for contact mode AFM. The cantilever is integrated with a sharp tip at the end. For contact mode it is necessary to have a cantilever which is soft enough to be deflected by very small forces and has a high

enough resonant frequency to not be susceptible to vibrational instabilities. Silicon probes primarily used for tapping mode applications. The tip and cantilever are an integrated assembly of single crystal silicon, produced by etching techniques. These probes are much stiffer than the silicon nitride probes, resulting in larger force constants and resonant frequencies.

Appendix E

Detailed Procedure for Nanoindentation Experiments

In this section we present a description of all the steps followed during the nanoindentation experiments.

The indenter may gradually become contaminated by adherence of foreign matter from tested samples. Therefore, before fixing the indenter on the transducer, the tip of the indenter was wiped with a tissue wetted with a cleaning solution of 70% methanol and 30% ethyl alcohol and then dried by blowing it with ultra-purified nitrogen. The cleanliness of the indenter was checked by carefully inspecting it under an optical microscope. The indenter was attached to the AFM and the controller of the transducer was connected and turned on. The force gain in the transducer controller displays the load applied to the transducer, which corresponds approximately to the weight of the indenter (251.6 mg). This procedure was used to check that all the connections were working properly. Once the value of the force gain had been checked the force gain was reset to zero.

The next step was to place the sample on the chuck and hold it there by a vacuum system. The sample was carefully positioned under the indenter in such a way that the part of the sample under the indenter was away from the edges of the sample and

close to relative flat regions. To minimize surface degradation a desiccant gel was used inside the AFM enclosure similar to the approach described by Yoo et al. [15]. Yoo using desiccant gel inside the AFM enclosure observed no evidence of surface modification and obtained the same results using dry nitrogen into the chamber. In our experiments the humidity was monitored and maintained below 12% during all the experiments with the desiccant inside the indentation chamber before loading the sample. Each crystal was used for less than six hours.

The tip was manually brought to a distance of about 75 μm from the surface with the AFM motor. The samples were allowed one hour to stabilize the cleavage planes and to achieve thermal equilibrium [150]. After one hour, indentations were started. The effect of the thermal drift can be seen on the continuous variation of the force gain in the transducer controller display, which decrease when the thermal drift attenuates. When the value of force gain was constant, typically taking about one hour, the machine was ready to indent and so the value of the force gain was set again to zero.

Before engaging the surface of the sample for the first time an air indentation was made in order to evaluate the effect of electrostatic forces. The air indentation consists of loading and unloading, without any holding, at a peak load of 20 μN and a load rate of 10 μN/sec, without thermal drift correction. The load-displacement of such indentation should result in an increase in displacement with constant load equal to zero. If the load-displacement shows a variation in load during the air indentation, it indicates the effect of electrostatic forces and the electrostatic force constant (EFC) must be changed. The EFC was changed before running the following air indentations, and the load vs. penetration depth curve evaluated until we found the desired response. A typical value of EFC was 0.02976 $\mu N/V^2$.

To engage the surface with the indenter two inputs have to be entered: 1) the velocity of engagement (μm/sec) of the tip and 2) the set point (nA) equivalent to

mg force, entered into the Hysitron software, i.e., the threshold of load measured by the transducer at which the vertical motor had to stop. These two values had to be chosen carefully to avoid false engagement and more important to not damage the surface of our sample. The velocity of engagement and the engagement load used were respectively: 1 μm/sec and 15 μN (1.5 nA). Once these two parameters were set and the scan size checked to be zero, so that the tip once touched the surface did not start scanning the surface with a load of 15 μN, the engagement could be made. No evidence of plastic deformation was observed with these parameters. As soon as the tip came in contact with the surface and then the z motor stopped the current set point was changed to 0.5 - 0.7 nA, corresponding to about 5 - 7 μN, and the scan size was changed to 1 μm.

The values input into the AFM software, which were used to engage the tip to the sample surface were the integral gain (2.00), proportional gain (3.00) and the current setpoint(1.5 nA). When the tip was engaged, the load displayed by the transducer controller was about 10 times the current setpoint value. Immediately after engagement, the AFM motor stopped and the scan size was changed to 1 μm. The indenter tip was used to scan the surface prior to each indentation. Indentations were made in regions selected from 15 μm x 15 μm areas. The regions for indentations were chosen with the criteria that there were relatively smooth large areas of the cleaved surface, free of visible cleavage steps. After the region was selected we performed a 1 μm x 1 μm scanning. While the engaged region was scanned, the appropriate load function was selected in the nanoindentation software and the number of data points was set to 3000. The thermal drift correction was set to a maximum drift rate of 0.1 nm/sec and a maximum time of 20 sec for all indentations. The next step was to set the scan size (so that the scanner stays in a point), the integral and proportional gain (so that the scanner does not add compliance to the indenter)of the scanner equal to zero and perform the nanoindentation. Once this was done, the

transducer maintained the load at zero for a period of 5 seconds and the drift rate of the displacement was evaluated. If this was greater than the maximum drift rate (0.1 nm/sec) the procedure was repeated for another 5 sec otherwise the indentation was performed. If the load was held to zero for 20 seconds and the drift rate was high, the indentation was still performed but such an indentation was not considered in this study. Thus, the drift rate was checked before indenting to confirm that it was less than 0.1 nm/sec averaged over a five second interval. For drift rates less than 0.1 nm/sec, the raw data obtained was corrected for the measured drift rate. After the indentation was performed, the tip was retracted and the integral gain and proportional gain were changed back to original values, so that an in situ image of the indentation was stored and displayed on the AFM monitor.

Five load functions were used for indentation of the AP samples. Each load function consisted of one loading-unloading cycle. The maximum loads applied were: 60 μN, 100 μN, 150 μN, 250 μN, 500 μN. The loading/unloading rate used was 20 μN/sec. Different unloading rates were used to evaluate the effect of this variable in the results. Hold periods were introduced at peak loads to reduce the effect of increase in depth at constant maximum load or creep.

As soon as the indentation was completed the load vs. penetration depth curve was plotted, and the value of the reduced modulus (E_r), hardness (H), contact depth (h_c) and measured stiffness (S), were analyzed based on the Oliver-Pharr method as described in Chapter two.

Name: Oscar Mejia Date of Degree: May, 2004

Institution: Oklahoma State University Location: Stillwater, Oklahoma

Title of Study: INVESTIGATION OF THE NEAR SURFACE MECHANICAL PROPERTIES OF AMMONIUM PERCHLORATE BY NANOINDENTATION

Pages in Study: 84 Candidate for the Degree of Master of Science

Major Field: Mechanical Engineering

Abstract:

The mechanical response of crystalline energetic solids to force loading is known to play a role in thermal decomposition, and also contributes to the overall mechanical behavior of the composite solid propellant. Ammonium perchlorate (AP) is the most widely used crystalline oxidizer because of its good characteristics, including compatibility with other propellant materials, good performance, quality, uniformity, cost and availability.

The near surface mechanical properties and mechanical behavior of the two cleaved surfaces of AP {001} and {210} have been investigated using nanoindentation in combination with atomic force microscopy (AFM). The crystal size was approximately 300 - 400 μm, which is about the size used for rocket fuel.

Multiple discontinuities (referred as pop-in) in load vs. penetration depth curves were observed in all the indentations. Both surfaces exhibited purely elastic behavior until the onset of plasticity at the first pop-in event.

The hardness exhibited the indentation size effect that is, hardness increased as depth decreased. The measured hardness in the near surface was higher than the previously reported for deeper Vickers indentations. For the {001} plane the average hardness obtained at 35 nm was 0.51 GPa and the hardness decreased to 0.27 GPa at a contact depth of 150 nm. For the {210} the average hardness value reduces from 0.72 GPa at 31 nm to 0.39 GPa at 121 nm. The average value of the reduced modulus found for the {001} plane was 22.2 $\pm$ 1.0 GPa and 19.9 $\pm$ 1.1 GPa for the {210} plane.

AFM was used to study the surface topography and identify the probable slip planes responsible for slip step formation around the indentations.

ADVISOR'S APPROVAL: Dr. D. A. Lucca

VITA

Oscar Mejia

Candidate for the Degree of

Master of Science

Thesis: INVESTIGATION OF THE NEAR SURFACE MECHANICAL PROPERTIES OF AMMONIUM PERCHLORATE BY NANOINDENTATION

Major Field: Mechanical Engineering

Biographical:

Personal Data: Born in San Salvador, El Salvador on January 19 1978, the son of Oscar Mejia and Emilia de Mejia.

Education: Bachelor of Engineering degree in Mechanical Engineering from Universidad Centroamericana "Jose Simeon Cañas" in November 2001. Completed the requirements for the Master of Science in Mechanical Engineering at Oklahoma State University in May 2004.

Professional Memberships: Student member of ASM International and student member of Phi Kappa Phi.